

UCSF

UC San Francisco Electronic Theses and Dissertations

Title

Regulation of Chromatin Structure and Segregation

Permalink

<https://escholarship.org/uc/item/49c3b1qh>

Author

Ng, Henry Yue Hon

Publication Date

2023

Peer reviewed|Thesis/dissertation

Regulation of Chromatin Structure and Segregation


by
Henry Ng

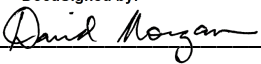
DISSERTATION
Submitted in partial satisfaction of the requirements for degree of
DOCTOR OF PHILOSOPHY

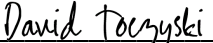
in
Biochemistry and Molecular Biology


in the
GRADUATE DIVISION
of the
UNIVERSITY OF CALIFORNIA, SAN FRANCISCO

Approved:

DocuSigned by:

E2BBE6A63C2745B... Alexander Johnson
Chair

DocuSigned by:

David O. Morgan, PhD

DocuSigned by:

David Toczyski

DocuSigned by:

C876331A93DC4B1... John Gross

Committee Members

Copyright 2023

by

Henry Yue Hon Ng

Acknowledgements

I would like to acknowledge not only the work from my collaborators, but also the support and training I received from everyone I met on this journey at UCSF. First, I ought to thank my mother, Teresa Wai Yee Leung 梁慧儀. In my eulogy for you, the most important attribute I tried to remind our friends and family of was your willingness to learn. Despite your age, the foreign land and culture we found ourselves in, you were unafraid to keep trying and learning. You started from scratch as a cashier, a bank teller after being an over-qualified accountant for decades. You took night classes to learn medical terminology which is completely different from all your past training and experiences. You raised me. You were the person who inspired me to try. I owe you apologies and gratitude for the unconditional love you provided and sacrifices you made for us.

Second, I need to thank the lab sister and brother I had in the two labs I did my thesis in, Dana Kennedy and Chris Carlson. Dana and Chris, you are not only my classmates but also my labmates. My betterment as a scientist stemmed from you, who I worked side by side with every day in the past 6 years. Dana, you have the patience and empathy that I require; Chris, you have the drive and the composure I lack. This PhD would not have been possible without your support and scientific contributions.

Third, I would like to thank my advisors, David Morgan and Bassem Al-Sady. I started my PhD in the Al-Sady Lab which shaped the scientist I am. From Bassem, I have learned how to communicate, and when to seize opportunities. I finished my PhD in the Morgan Lab, which allowed me to fully evolve as a scientist of my own. Dave rekindled my desire to think about science and let me lead and brew my own project. I am grateful for Dave taking me in as fourth-year PhD student to start a whole new project.

I would like to thank my undergraduate advisor Neta Dean. Neta, there are no words I can use to describe how you have changed my life. You let me volunteer in your lab without any experience. You gave me an independent project and helped me published it. You stood alongside with me when my mother was dying. You encouraged me to pursue my PhD. You reminded me that my mother would be proud of me when I graduated college. And you checked in on me in the past six years as you know I am having a difficult time in grad school. You generated the ripples in my life; this PhD journey would not be existent without you.

Also, I need to acknowledge all past and present collaborators and labmates. Nick Sanchez, R. Greenstein, Lucy Brennan, Eric Simental, Lena Kallweit, Cal Clemmer, Amanda Woo from the Al-Sady Lab had provided a haven for me as a young scientist. I would like to thank R. especially on the collaboration, and Nick for being a welcoming presence when I first interviewed at UCSF. Luke Strauskulage, Madeline Keenen, Robbie Diaz, Harrison Khoo from the Redding Lab had provided ample scientific contributions and comradery in our shared group meetings. From the Morgan Lab, Jonathan Asfaha, Nairi Hartooni, Chloe Ghent had provided me a welcoming warmth when I first joined the lab; and mentoring Briana Marinoni, Armin Adly, and Emmy Delaney had been a fruitful experience.

Thank you to all the unofficial mentors I had at UCSF, Barbara Panning, Sandy Johnson, Dave Toczyski, John Gross. Thank Barbara for helping me during my housing crisis when I was a rotation student. Thank Sandy, Dave T. and especially Kaveh Ashrafi for helping me transition from the Al-Sady Lab to the Morgan Lab. Thank all the contributors in my published or soon to be published projects, including Ramon R Barrales, Catherine Tan, Sigurd Braun, Magdalena Murawska, Tamas Schauer, Karl Olsen, Andreas Ladurner, Raymond Suhandynata and Huilin Zhou. I acknowledge the helpful discussions from Douglas Myers-Turnbull and Sandra Catania. Thank Toni Hurley, Danny Dam and Billy Luh for running the Tetrad program.

I would like to thank my classmates, friends, families, and my chosen family. Without the support from you all, I would not have finished this degree. Special thanks to Ben Herken, Gabriella Estevam, Natalie Whitis, Elise Munoz and Manuela Richter for your presence in my life. Thank all the Procraftinators members, especially Francesca Del-Frate, Katie Augspurger and Haley Gause. Thank all the gamers that help distracts me, especially Liz Bond. Thank you for my chosen family who let me live as myself and gave me the freedom and support in San Francisco. Thank Josh Farr and Christie Shea, for doing our own PhDs side by side in different institutes yet still maintaining a friendship and checking in with each other constantly. Thank you, Janie Ou Yang. Thank you to my family, my father Clarence Cheung Wai Ng 吳翔偉, and my brother Tim Yue Chung Ng 吳宇翀. Thank my extended family, Aunt Sabina 吳育珍, Uncle Eric 吳翔均, Aunt Kit 梁結儀, Aunt Angela 鄭少芬, and Uncle Thomas 梁民熙. Special thanks to Uncle Marcus 吳翔輝, Aunt Judy 薛美嫦 and my cousin Kevin Yue Kiu Ng 吳宇翹. You have provided my family and I a safe space to land when we first moved to New York. Thank your family for being so welcoming and helpful to a family of new immigrants.

Thank you, Taylor Emmerson for being my first friend in San Francisco and living with me for the last 4 years. You let me keep you homeless for two months. You have witnessed all the ups and downs. You have quarantined with me throughout COVID. You were the best roommate anyone can ask for.

Contributions

This thesis is a reproduction of materials published in PLOS Genetics, Cell Report and in preparation for publication. Citations are presented below.

Greenstein RA*, **Ng H***, Barrales RR, Tan C, Braun S, Al-Sady B. Local chromatin context regulates the genetic requirements of the heterochromatin spreading reaction. PLoS Genet. 2022 May;18(5):e1010201. *Contributed equally to this work

Murawska M, Greenstein RA, Schauer T, Olsen KCF, **Ng H**, Ladurner AG, Al-Sady B, Braun S. The histone chaperone FACT facilitates heterochromatin spreading by regulating histone turnover and H3K9 methylation states. Cell Rep. 2021 Nov 2;37(5):109944.

Ng H, ..., Morgan DO. Phosphate-binding pocket on cyclin regulates mitotic timing. 2023. In Progress.

Abstract

Regulation of Chromatin Structure and Segregation

Henry Yue Hon Ng 吳宇瀚

The genetic material is packaged differentially at different phases of the cell cycle. In interphase, cells package their genome into heterochromatin and euchromatin domains, where genes are repressed or expressed based on cell identity. Heterochromatin, the gene-repressive structure, is regulated by different factors that control methylation and acetylation on histones.

During cell division, these histone modifications are copied onto the newly synthesized DNA. The heterochromatin structure is seeded from nucleation DNA sequence that recruits other factors to spread the domain. In our studies, we found that the factors required for spreading heterochromatin in different genomic regions are highly variable. Notably, we proposed a mechanism by which Fkh2, a transcription factor, recruits Clr6 histone deacetylase complex I" to a nucleated heterochromatin domain that initiates the spread of heterochromatin domains.

During mitosis, the chromatin is packaged into condensed chromosomes for faithful segregation of the duplicated genome. Progression through mitosis is regulated by the levels of a family of protein kinase complexes named Cyclin-Dependent Kinases (CDKs). The phosphorylation of numerous CDK substrates drives various mitosis events. We identified a novel phosphate-binding pocket on cyclins that aids in the timing of sequential multisite phosphorylation in CDK substrates and mitotic events. Loss of this pocket causes a mitotic delay *in vivo* as well as loss of multisite phosphorylation in various CDK substrates *in vitro*.

Table of Contents

Chapter 1

Local chromatin context dictates the genetic determinants of the heterochromatin spreading reaction.	1
Introduction	3
Results	7
Discussion.....	22
Methods	28

Chapter 2

<i>Phosphate-binding pocket on cyclin regulates mitotic timing.....</i>	<i>85</i>
Introduction	87
Results	90
Discussion.....	95
Methods	98
References.....	121

List of Figures

Chapter 1

Fig 1.1. A genetic screen based on a suite of fluorescent reporters identifies regulators of heterochromatin nucleation-distal gene silencing in different chromatin contexts	41
Fig 1.2. Gain of nucleation-distal gene silencing in MAT Δ REIII and ECT chromatin contexts.	43
Fig 1.3. Heterochromatin nucleation-distal gene silencing is regulated by sets of unique and common protein complexes across different chromatin contexts.	45
Fig 1.4. Chromatin remodeler, SAGA and Clr6 complexes regulate nucleation-distal silencing	47
Fig 1.5. Fkh2- containing Clr6 Complexes regulate H3K9me2 spreading at constitutive and facultative heterochromatin loci	49
Fig 1.6. Fkh2 is a resident member of multiple Clr6 complexes and directs Clr6 to nucleation-distal heterochromatin regions	50
Fig S1.1. Screen of chromatin contexts with “green” and “orange” reporters.....	53
Fig S1.2. Regulators of heterochromatin nucleation-distal silencing in all four chromatin contexts.....	54
Fig S1.3. <i>apm3</i> and <i>apl5</i> , coding for nuclear-cytosolic and cytosolic proteins, respectively, act together in modulation of heterochromatin spreading.....	56
Fig S1.4. Gain of nucleation-distal gene silencing mutants in <i>WT MAT</i> , <i>MAT ΔREIII</i> and <i>ECT</i> chromatin contexts.	57
Fig S1.5. RT-qPCR validations of selected chromatin-context unique loss and gain of nucleation-distal silencing hits	58

Fig S1.6. <i>gcn5</i> is specifically required for H3K9me2 spreading at the <i>ECT</i> heterochromatin spreading sensor, but not pericentromeric heterochromatin.....	59
Fig S1.7. Class III HDAC family Sir2 is required for heterochromatin silencing.....	59
Fig S1.8. 2D density hexbin plots for all Clr6 complex subunit screen mutants in <i>MAT ΔREIII</i>	60
Fig S1.9. Fkh2- containing Clr6 complexes direct H3K9me2 spreading at multiple genomic regions.	62
Fig S1.10. Fkh2 and Prw1 act together in spreading H3K9me2.....	63
Fig S1.11. Effect of <i>clr6-1</i> and <i>Δprw1</i> on H3K9me2 at a WT <i>MAT</i> locus without reporters.....	64
Fig S1.12. Fkh2- containing Clr6 complexes contribute primarily to H3K9me2 spreading, while Clr3 is required for H3K9me2 accumulation at all heterochromatin regions except islands	65
Fig S1.13. Clr6 affects spreading of H3K9me3.....	66
Fig S1.14. Fkh2 is a constituent member of Clr6 complexes.....	67
<i>Fig S1.15. Fkh2 does not affect transcription of core heterochromatin regulators.</i>	<i>68</i>
 <i>Chapter 2</i>	
Fig 2.1. The phosphate-binding pocket is conserved in B-type cyclins.	106
Fig 2.2. Mutation of the phosphate-binding pocket in <i>Clb2</i> causes a growth defect in the absence of <i>CLB1</i> and <i>CLB3</i>	107
Fig 2.3. The <i>clb2-pp</i> mutation causes a mitotic delay.....	109
Fig 2.4. Identification of proteins with reduced phosphorylation in <i>clb2-pp</i> cells.	110
Fig 2.5 Phosphorylation is reduced with <i>clb2-pp</i> in <i>vitro</i>	111
Fig S2.1 Protein sequences of selected proteins identified from SILAC-MS.....	112

Fig S2.2. GO Analysis of proteins which phosphorylation is reduced in *clb2-pp*. 113

List of Tables

Chapter 1

Table S1.1. Nuclear function gene deletion library	69
Table S1.2. Strain table.	81
Table S1.3. Primers used for CHIP qPCR and RT qPCR.	85

Chapter 2

Table 2.1 Yeast Strain Table	114
Table 2.2 Plasmid Table	115
Table S2.1 MS Analyzed peptide containing CDK site with $\text{Log}_2 \text{L/H} > 1$	116

Chapter 1

Local chromatin context dictates the genetic determinants of the heterochromatin spreading reaction.

Local chromatin context dictates the genetic determinants of the heterochromatin spreading reaction.

R.A. Greenstein^{1,2,†}, Henry Ng^{1,2,†}, Ramon R. Barrales^{3,#}, Catherine Tan^{5,6}, Sigurd Braun^{3,4}, and Bassem Al-Sady^{1,*}

¹Department of Microbiology & Immunology, George Williams Hooper Foundation, University of California San Francisco, San Francisco, CA 94143, USA,

²TETRAD graduate program, University of California San Francisco, San Francisco, CA 94143, USA,

³Biomedical Center, Department of Physiological Chemistry, Ludwig-Maximilians-Universität of Munich, 82152 Planegg-Martinsried, Germany,

⁴Institute for Genetics, Justus-Liebig University Giessen, 35392 Giessen, Germany, #current address: Centro Andaluz de Biología del Desarrollo, Universidad Pablo de Olavide de Sevilla-Consejo Superior de Investigaciones Científicas-Junta de Andalucía, Sevilla, Spain.

⁵Department of Cell and Tissue Biology, University of California San Francisco, San Francisco, CA 94143, USA,

⁶Biomedical Sciences graduate program, University of California San Francisco, San Francisco, CA 94143, USA

[†]These authors contributed equally to this work, listed in alphabetical order

*Correspondence: bassem.al-sady@ucsf.edu

Introduction

Cellular differentiation requires stabilizing gene expression such that genes coding for lineage inappropriate information are repressed while genes required for specific cell states are active. Spatial and temporal stabilization of repressive gene states is dependent on the formation and propagation of heterochromatin structures. Heterochromatin is most commonly seeded by DNA sequence-directed nucleation^{1,2} and then propagated distally in a sequence-independent process termed spreading to silence genes in neighboring regions. Heterochromatin structures are associated with chromatin marks, such as histone 3 lysine 9 methylation (H3K9me), which are recognized by “readers” that include Heterochromatin Protein 1 (HP1)^{3,4}. In some cases, the heterochromatic state then restricts transcription directly through exclusion of RNA polymerase via histone deacetylases (HDACs)⁵. Alternatively, or in parallel, RNA processing pathways promote silencing downstream of heterochromatin assembly^{6,7}.

The spreading of heterochromatin, and thus gene silencing distal to the nucleation site (nucleation-distal silencing) occurs in at least two very different chromatin contexts: 1. Constitutive heterochromatin, which is generally gene-poor and therefore depleted of activities associated with active genes known to antagonize heterochromatin^{8,9}; or 2. heterochromatin involved in regulating cellular differentiation, which is either seeded at new nucleation sites or invades gene-rich euchromatin *de novo* from existing nucleation sites¹⁰⁻¹⁴. In either scenario, specific factors may intrinsically promote or antagonize the distal spreading of gene silencing. For constitutive heterochromatin, the inheritance of nucleosomes bearing heterochromatic marks maintains gene silencing across cell divisions¹⁵. This inheritance promotes modification of nearby nucleosomes through “read-write” positive feedback mechanisms that are intrinsic to heterochromatin histone modifiers¹⁶⁻¹⁸. In contrast, when heterochromatin invades active chromatin *de novo*, as occurs in differentiation, it will encounter chromatin modifications that can specifically antagonize heterochromatin⁸. Gene silencing at these sites does not benefit from the

inheritance of pre-existing marked nucleosomes. Beyond the differences between active and inactive chromatin, it remains unclear whether distinct nucleation element classes require different regulators to enact efficient spreading outward from those sites.

Fission yeast is an excellent model for addressing the regulation of heterochromatin spreading:

1. It contains a small number of well-defined heterochromatin nucleators, 2. harbors heterochromatin domains that are constitutive as well as others involved in cellular differentiation, and 3. is competent to assemble ectopic heterochromatin domains at nucleation sequences inserted into euchromatin. Over the past four decades, forward and reverse genetic screens in fission yeast have established an exhaustive list of factors required for the nucleation of heterochromatin domains. These nucleation mechanisms include repeat sequences that instruct RNAi-machinery to process noncoding (nc) RNAs involved in targeting the histone methyltransferase Clr4¹⁹; signals within nascent transcripts that trigger heterochromatin island formation²⁰; pathways involving telomere-protection by the shelterin complex^{21,22}; and transcription factor-bound sequences that recruit heterochromatin regulators directly²³.

However, less is understood about factors specifically required for propagating gene silencing through heterochromatin spreading.

We previously developed a fluorescent reporter-based heterochromatin spreading sensor that can assess one key output of heterochromatin (gene silencing) separately from the spatial control of heterochromatin spreading^{8,24}. This allows us to address the following questions: 1.

Are there known or novel regulators that primarily regulate spreading versus nucleation? 2.

Does spreading over chromatin with distinct characteristics, such as gene density or

nucleosome arrangements, require different sets of regulators? 3. Do unique heterochromatin

nucleation pathways interface with unique heterochromatin spreading regulators? 4. Are there

distinct sets of regulators for spreading of the heterochromatin structure and gene silencing?

Addressing these questions would elucidate mechanisms that safeguard the genome as well as stabilize specific cell states.

Here, we conduct series of reverse genetic screens in *S. pombe* using a custom collection of gene deletions that target nuclear functions. We investigated gene silencing in different heterochromatin contexts that include several derivatives of the fission yeast mating type (MAT) locus. This gene-poor constitutive heterochromatin region is contained by *IR-L* and *IR-R* boundaries²⁵⁻²⁷ and nucleated by at least two elements: (1) cenH, which is homologous to pericentromeric dh and dg elements and relies on ncRNA pathways, including RNAi^{26,28,29}; (2) the REIII element, a sequence which recruits heterochromatin factors via the stress-response transcription factors Atf1 and Pcr1^{23,30}. We also analyzed an ectopic heterochromatin domain that is embedded in gene-rich euchromatin. This domain is nucleated by an ectopically inserted dh element fragment proximal to the *ura4* locus^{24,31,32}. Using the combination of MAT derivatives and the ectopic site allowed us to query requirements for nucleation-distal heterochromatin assembly emanating from different classes of nucleators and in different chromatin environments.

Our genetic screen revealed that requirements for heterochromatin spreading differ significantly between distinct chromatin contexts, and to some degree, between different nucleation mechanisms. In particular a specific histone deacetylase (HDAC) complex, Clr6, guided by the Fkh2 transcription factor, is linked to heterochromatin spreading distal to nucleation sites. In contrast, the Clr3 HDAC is generally involved in regulating H3K9me and gene silencing within the entire heterochromatin domain. Our genetic analysis further indicates that there is broad antagonism of heterochromatin-dependent gene silencing at nucleation-distal sites by a diverse set of nucleosome remodelers, in particular Ino80 and Swr1C. Together our genetic analyses

allow dissection of both site-specific and broader pathways linked to the spreading of gene-silencing heterochromatin.

Results

We previously developed a heterochromatin spreading sensor that relies on three transcriptionally-encoded fluorescent protein-coding genes that collectively allow single-cell measurement of heterochromatin formation via flow cytometry, while normalizing for transcriptional and translational noise^{24,33}. This method provides separate, quantitative recordings of nucleation proximal (“*green*”) and distal (“*orange*”) gene expression at a heterochromatin site over large populations of isogenic cells (typically $N > 20,000$, unless strains grow poorly) (**Fig 1.1A**). The scale of the analysis permits quantitative tracking of unique population distributions, such as multimodal states that would be obscured by ensemble data. When we analyze heterochromatin spreading specifically with our sensor (see Methods), we do so by examining “*orange*” in cells that are “*green*”OFF, which we take as a proxy for normal nucleation^{8,24}. This analysis, therefore, considers the transcriptional consequences of heterochromatin assembly by generating a sensitive readout of the “*green*” and “*orange*” reporters that persists for several cell cycles. However, we note that we cannot account for the possibility of highly transient loss-of-nucleation events that do not result in measurably altered transcription at “*green*”.

Design of heterochromatin spreading sensors that assess four chromatin contexts

To explore whether different genetic contexts utilize general or specific sets of regulators for nucleation-distal gene silencing, we queried three different derivatives of the constitutively heterochromatic mating type (*MAT*) locus and one euchromatic context, each containing an embedded heterochromatin spreading sensor (**Figs 1.1A and S1.1**)²⁴. The mating-type locus contexts included wild type *MAT*, with the *cenH* and *REIII* nucleating DNA elements intact, and two *MAT* variants that contained mutations in either the *cenH* or *REIII* elements (**Figs 1.1A, S1.1A and S1.1B**). Mutations in these DNA elements limit initiation of heterochromatin spreading from one nucleator or the other²⁴. To probe heterochromatin formation in the

euchromatic context, we focused on the *ura4* locus, where heterochromatin spreading is ectopically driven by the upstream insertion of a pericentromeric dh DNA element (**Fig S1.1C**,^{24,31}). We refer to this chromatin context as *ECT* (ectopic).

We first focus on the analysis of strains in which nucleation is driven only by one element, *i.e.* *MAT ΔcenH* (OFF isolate, see Methods), *MAT ΔREIII*, and *ECT*. When analyzed by flow cytometry, *MAT ΔcenH* populations appear fully nucleated with near-complete local spreading, as evidenced by population density in the bottom left in the 2D density hexbin plot (**Fig 1.1E Top**²⁴). *MAT ΔREIII* and *ECT* cell populations, while mostly nucleated, display a stochastic distribution of spreading states, as evidenced by a vertical distribution on the left of the 2D density histogram (**Fig 1.1G and 1.1I Top**²⁴). While the distance between nucleation and sensor sites varies slightly for the different chromatin contexts analyzed (from 2.4 to 3.6 kb; see **Fig S1.1**), we showed previously that altering the distance between “green” and “orange” does not qualitatively affect the output²⁴. Thus, we presume that these differences in behavior reflect different intrinsic properties of the chromatin environment rather than the difference in spatial distribution relative to the nucleation site. In addition to the wild-type background, we assessed *Δclr3* as a reference point for strong loss of gene silencing (**Fig 1.1E, 1.1G and 1.1I, Middle**).

Identification of chromatin context-specific positive spreading regulators

In order to identify nuclear factors linked to context-specific spreading, we crossed a deletion library of ~400 nuclear function genes (see Methods and **Table S1.1 and Fig 1.1B**) to the four reporter strains above and measured nucleation and spreading by flow cytometry. To segregate proximal from distal silencing, we first isolated cell populations that reside within a “green”-off gate, which represents cells with heterochromatin fully assembled at the nucleation site and no expression of the reporter (see Methods, **Fig 1.1C** and ²⁴). Within this gate, we divide the “orange” signal into 4 grids, from fully repressed (*i.e.*, complete spreading over “orange”; Grid 1)

to fully de-repressed (*i.e.*, no silencing at “orange”; Grid 4), with the remaining space symmetrically divided to yield Grids 2&3 (see Methods). To quantify increased or decreased nucleation-distal silencing in a given mutant, we calculated a $\text{Grid}_n^{\text{mut/par}}$ metric (described in Methods), which tracks the changes of cell distributions in “orange” expression within the “green”-off gate (**Fig 1.1C**). Since *MAT ΔcenH* and also *WT MAT* display very tight silencing of both “green” and “orange” with very few events in grid 4 (**Figs 1.1E and S1.2A**), we used a $\text{Grid}_n^{\text{mut/par}}$ metric that considers both grids 3+4 for the robust identification of spreading defects in these strain backgrounds. *MAT ΔREIII* and *ECT* have a more stochastic spreading behavior with “green”-off cells populating a range of “orange” states from OFF to ON²⁴, including, to some extent, both grid 3 and 4 (**Fig 1.1G and 1.1I**). Hence, for these two contexts we used a $\text{Grid}_n^{\text{mut/par}}$ metric that only considers grid 4 to focus on complete loss of spreading (*i.e.* “orange” signal in the range of *Δclr4* control). We used two metrics to define gain or loss of spreading mutants for further analysis. The first was a significance threshold used if multiple parental isolates were available (all except *ECT*). To meet this criteria $\text{Grid}_n^{\text{mut/par}}$ values had to be at least 2 standard deviations (2SD) above the mean of the parent isolates (red line, **Figs 1.1F and 1.1H and S1.2C, S1.2D, S1.2F and S1.2H**). As an additional cut-off, we only considered the top 15% of all $\text{Grid}_n^{\text{mut/par}}$ -ranked mutants, even though more genes passed the 2SD significance threshold, primarily to focus on the genes with the highest impact on nucleation-distal silencing (blue dotted line). Having identified these gene hits, we proceeded to analyze their relationships within and across chromatin contexts.

As general note on how we describe the function of our screen hits, in cases where we can correlate silencing defects at the spreading reporter to altered H3K9 methylation, we refer to these changes as heterochromatin spreading defects. In other cases where we lack information on H3K9 methylation, we refer to these changes as nucleation-distal gene silencing defects, as

it is in principle possible that certain mutants can affect gene silencing without affecting structural features of heterochromatin.

We first examined the degree to which modulators of nucleation-distal silencing are shared between chromatin contexts where heterochromatin spreading is driven by one major element, via upset plots (**Figs 1.1D and S1.2I** for all four contexts). Conceptually similar to a Venn diagram, this analysis allows rapid visualization of the degree of overlap between data sets, with the number of shared hits plotted as a bar graph and the sets each bar represents annotated below the plot. For loss of nucleation-distal silencing (*i.e.* mutants in genes that promote spreading, **Fig 1.1D**), these upset plots showed that exceedingly few genes were shared across all chromatin contexts (*i.e.* 3 out of 145 unique hits for singly-nucleated contexts, **Fig 1.1D**; 2 of 164 unique for all contexts hits, **Fig S1.2I**). Notably, two of these three genes (*apm3*, *rrp17*) have not previously been implicated in heterochromatin assembly. *Apm3* has been proposed to be part of an AP-3 adaptor complex that mediates vesicle trafficking, whereas *Rrp17* is a predicted rRNA exonuclease.

We expanded this analysis to also include the *WT-MAT* context. Six genes were shared across all the *MAT* locus chromatin contexts (*apl5*, *cph1*, *hrp1*, *spt2*, *snt2*, *pcf1*). In contrast, the majority of hits (*i.e.* 101 genes for all contexts, 118 when examining singly nucleated contexts) were linked to regulation in only one chromatin context. The degree to which genes contributed positively towards spreading ($\text{Grid}_n^{\text{mut/par}}$) and the degree of overlap across chromatin contexts (by color code) is shown in **Figs 1.1F, 1.1H, 1.1J** and **S1.2B, S1.2D, S1.2F** and **S1.2H** along with the top loss-of-spreading hit for each context (**Figs 1.1E, 1.1G, 1.1I Bottom** and **S1.2A Bottom**). A similar picture emerged on a more coarse-grained level, comparing the two major chromatin environments, *MAT* and *ECT*. To do so we grouped both singly nucleated *MAT* contexts (*MAT* Δ *REIII* and *MAT* Δ *cenH*) and compare them to *ECT*. Even in this small

comparison of two groups, only 17 genes are shared out of a total of 145 (**Fig 1.1K**). The low overlap of genes shared across specific chromatin contexts and environments in the genome emphasizes that specific contexts have a strong impact on nucleation-distal silencing.

Examining the top hits, we make the following observations: Pathways that restrain the heterochromatin antagonist Epe1 play a prominent role in promoting nucleation-distal silencing. Both the COP9 signalosome and an E3 ubiquitin ligase complex comprising the adaptor proteins Ddb1 and Cdt2³⁴ are involved in Epe1 turnover^{34,35}. *cdt2* is one of the three hits conserved across all singly nucleated contexts. We found that *csn1* (COP9), *cdt2*, and *ddb1* are the three strongest hits in *ECT* and that *cdt2* is also among the top hits in *MAT ΔcenH*. The histone chaperone, Asf/HIRA (*hip1*) and histone variant H2A.Z (*pht1*) were top hits linked specifically to *ECT* regulation (**Fig 1.1J**). H2A.Z was just recently shown to play a role in maintaining RNA-driven heterochromatin in *S. pombe*³⁶ and is known to antagonize heterochromatin spreading in budding yeast³⁷, indicating that a role for this histone in heterochromatin domain expansion control is conserved even though it functions in opposite directions in the two systems. The transcription factor gene *fkh2* was a top hit in regulation of *WT MAT* and *MAT ΔREIII*, along with *rrp6*, a key member of the nuclear exosome (see below; **Figs 1.1G and S1.2A**). We also saw strong hits that were unique to *MAT ΔcenH*. The top hit here was *gad8*, which encodes a protein kinase that targets several factors, including Tor1 and Fkh2 (**Fig 1.1E**). In short, specific gene sets seem to regulate spreading distal to the nucleation site in different chromatin contexts. Though specific, some of these genes play a conserved role in regulating chromatin spreading in other organisms.

As mentioned above, loss of the AP-3 adaptor complex subunits Apm3 and Apl5 induced nucleation-distal gene silencing, and as we will show below, impairs H3K9me2 accumulation. Interestingly, loss of Apm3 affected spreading in all chromatin contexts, whereas Apl5 affected

only the *MAT* contexts (also observed in ³⁸). We further assessed the activities of Apm3 and Apl5 by generating $\Delta apm3$ and $\Delta apl5$ single and double mutants in the *MAT* $\Delta REIII$ background, where $\Delta apm3$ and $\Delta apl5$ had a moderate and mild effect in the screen, respectively. We reproduced the mild to moderate spreading defect for both single mutants; we further observed a slightly stronger defect in the $\Delta apm3 \Delta apl5$ double mutant (Grid4 mut/par 1.56) compared to the $\Delta apm3$ and $\Delta apl5$ single mutants (Grid4 mut/par 1.4 and 1.16, respectively; **Fig S1.3A– S1.3D**). Whereas Apl5 is largely cytoplasmic, thus likely acting indirectly, Apm3 shows both nuclear and cytoplasmic localization, (**Fig S1.3E and S1.3F**) and also affects H3K9me2 accumulation at heterochromatin islands (**Fig S1.3G**). Together, these findings suggest a direct rather than indirect role for Apm3 in heterochromatin assembly. However, further work is needed to elucidate the specific function of Apm3 in heterochromatin spreading and whether this is linked to the AP-3 complex itself.

Identification of negative spreading regulators

In addition to loss of nucleation-distal silencing (positive regulators), we also identified mutants that showed gain of silencing (negative regulators). We examined a $Grid_n^{mut/par}$ metric that considers grid 1, as increased distribution into grid 1 indicates silencing of “orange” beyond the wild-type. We could not examine *MAT* $\Delta cenH$ for this phenotype because this chromatin context is highly repressed in the OFF state as reported previously and the vast majority of cells are already resident in Grid 1 (**Fig 1.1E**)^{24,39}. As before, we examined first singly nucleated contexts in which gain of spreading can easily be detected, *i.e.* *MAT* $\Delta REIII$ and *ECT* (**Fig 1.2**) and separately also all three contexts including *WT* *MAT* (**Fig S1.4A–S1.4F**). Even though *ECT* displays a very similar spreading behavior to *MAT* $\Delta REIII$ ²⁴, we found little overlap between the two, with only 10 genes shared between them (for *MAT* $\Delta REIII$ and *ECT*: 10 shared out of 92, **Fig 1.2B**; examples for top hits are shown in **Fig 1.2D and 1.2F**. For all contexts including *WT* *MAT*: 5 shared out of 98, these are *vps71*, *arp6*, *leo1*, *git1*, and *pmk1*, **Fig S1.4G**). Of the more

limited number of genes shared across all three contexts, we note that *Leo1* was previously shown to be implicated in spreading control across boundaries⁴⁰, whereas *Vps71* and *Arp6* are members of the H2A.Z-specific *Swr1* remodeling complex⁴¹. The larger number of antagonists unique to *ECT* (**Figs 1.2B** and **S1.4G**) suggests that heterochromatin spreading is under additional layers of control in the euchromatic context.

We sought to independently validate the above observations. We selected 5 mutants that have chromatin context-specific effects, covering both loss and gain of spreading: *saf5*, which shows gain of spreading in *WT MAT* and mildly in *MAT ΔREIII*; *eaf6*, which shows gain of spreading in *MAT ΔREIII* only; *pht1* and *hip1*, which show loss of spreading only in *ECT*; and *gad8*, which shows loss of spreading primarily in *MAT ΔcenH*. We recreated these mutations *de novo* in the chromatin contexts described above and conducted RT-qPCR analysis for SF-GFP (“*green*”, nucleation) and mKO2 (“*orange*”, spreading) transcripts. This validation approach broadly recapitulated our initial screen (**Fig S1.5**), confirming that these gene products play context-specific functions in nucleation-distal silencing.

Chromatin remodelers broadly antagonize nucleation-distal silencing

Taking our analysis beyond individual genes, we sought to query which protein complexes are involved in regulating nucleation-distal gene silencing, as this may highlight the major pathways involved in this process. Using the Gene Ontology (GO) protein complex annotations from Pombase⁴², we annotated each gene hit that met the criteria for further analysis as outlined above for all four chromatin contexts. We then tabulated the frequency (“counts”) of each GO complex by chromatin context for both loss of distal silencing (loss) and gain of distal silencing (gain) phenotypes, performed unsupervised clustering on the data, and displayed the results as a heatmap (**Fig 1.3**). Overall, we identified three major common trends: 1. A broad role for chromatin remodelers in antagonizing nucleation-distal silencing; 2. a role for the SAGA

complex in promoting nucleation-distal silencing at *ECT*; 3. a role for Clr6 histone deacetylase complexes (HDACs) in promoting nucleation-distal silencing at *MAT*, with the notable exception of the Set3C module (part of expanded Rpd3L complex), which antagonizes distal silencing.

Mutants defective in chromatin remodeling complexes strongly contribute to the “gain” phenotypic category, which includes the Swr1C, Ino80, SWI/SNF, and RSC-type complexes (**Fig 1.3**). To explore this further, we assessed which protein components contributed to these GO complex counts. For all genes annotated to a given chromatin remodeling complex and present in our screens, we displayed whether they were identified as a hit (blue) or not (grey) in a hit table (**Fig 1.4A**). Indeed, we found that the large majority of the gene hits annotated fall within the “gain” but not “loss” phenotype across backgrounds, confirming that these nucleosome remodeling complexes potentially antagonize spreading (see examples 2D hexbin plots, **Fig 1.4B**).

SAGA primarily promotes heterochromatin spreading in the euchromatic context

A surprising observation was the enrichment of a large number of subunits of the SAGA complex among the loss-of-nucleation-distal silencing hits (**Fig 1.3**). Indeed, six SAGA subunit genes were associated with altered expression of the *ECT* reporter, the most enriched single complex for any reporter strain (**Figs 1.3**, and **1.4C**). This suggests that SAGA, a histone acetylase involved in gene transcription, positively regulates nucleation-distal silencing in euchromatin (see example 2D hexbin plots, **Fig 1.4D**). To assess if SAGA directly influences heterochromatin spreading, rather than indirectly affecting gene silencing, we assessed H3K9me2 accumulation at “green” and “orange” in the *ECT* background, as well as the pericentromeric *dg* element. Consistent with the results of the genetic screen, we find that the histone acetylase catalytic subunit Gcn5 is required for efficient spreading of H3K9me2 to “orange”, but not its establishment at “green” or at *dg* (**Fig S1.6**).

Clr6 HDAC complexes promote nucleation distal silencing, primarily in constitutive heterochromatin

Three classes of HDACs exist, which have both redundant and non-overlapping functions in the formation of heterochromatin domains and gene silencing. Clr6 belongs to class I and is part of several sub-complexes, contributing to both heterochromatic and euchromatic gene regulation^{43,44}. Clr3 belongs to class II and is a member of the SHREC complex⁴⁵, whereas Sir2 is a class III HDAC of the sirtuin family⁴⁶. Based on our screen, class II and III HDACs affect nucleation and distal gene silencing equally, indicating that they do not act in a spreading-specific manner. (Clr3, **Fig 1.1**; Sir2, **Fig S1.7**). In contrast, sub-complexes of the Clr6 family, including Rpd3S, Rpd3L, and Clr6 I', contribute exclusively to nucleation-distal but not proximal silencing (hit table, **Fig 1.4E**; 2D hexbin plots, **Figs 1.4F** and **S1.8**). As noted above, the forkhead transcription factor Fkh2 was identified amongst the strongest nucleation-distal silencing hit in *WT MAT* and *MAT ΔREIII* reporter strains. Despite not being formally annotated to the Clr6 I' complex by GO terms, Fkh2 has previously been linked to this sub-complex⁴⁷. Based on this previous analysis, and our genetic data, we considered Fkh2 to be a member of Clr6 I'. While Rpd3L/ Clr6 I', Clr6 I'', and Clr6S (Complex II) positively contributed to spreading ("loss" phenotype), several members of the Rpd3L-Expanded complex antagonized spreading and were found as hits inducing a "gain" phenotype (**Figs 1.4E, 1.4F** and **S1.8**). This includes a subset belonging to the Set3 Complex (Set3, Hif2, Hos2, Snt1). We validated our analysis by examining the phenotype of the *de novo* generated gene deletion strains of *fkh2* and *prw1*, which encodes a core structural subunit of the Clr6 HDAC complexes, in the *MAT ΔREIII* heterochromatin spreading sensor (**Fig 1.4F, Bottom**). The *Δfkh2 Δprw1* double mutant displayed a similar phenotype to the *Δprw1* single mutant, corroborating the hypothesis that Fkh2 is part of the same complex as Prw1 (**Fig 1.4F, Bottom**).

Overall, these data suggest that Clr6 I', Clr6 I" and Clr6S HDAC complexes specifically promote nucleation-distal heterochromatic gene silencing.

Clr6 complexes promote distal H3K9 methylation spreading at telomeres, pericentromeres and islands.

The analysis above suggests that Clr6 complex subunits contribute to the spreading of gene silencing. We therefore examined the mechanisms underlying this phenotype and examined the role of Clr6 relative to another prominent heterochromatic HDAC, Clr3, which is well-established as a key regulator heterochromatin in gene silencing^{45,48}. First, we examined whether the phenotype observed for $\Delta prw1$ and $\Delta fkh2$ holds true for *clr6* itself, which encodes the catalytic subunit in the complex. We tested the phenotype of the *clr6-1* allele, which has a hypomorphic phenotype at permissive temperatures (note that *clr6* is an essential gene)⁴³. Under these conditions, *clr6-1* shows moderate spreading defects in *MAT $\Delta REIII$* without affecting nucleation, which is consistent with its role in nucleation-distal silencing (**Fig 1.5B** vs. **1.5A**). In contrast, a catalytically dead mutant of Clr3 (*clr3-D232N*) showed complete loss of silencing (**Fig 1.5C** vs **1.5A** and **Fig 1.1**). This complete loss of silencing is identical to the null $\Delta clr3$ (**Fig 1.1**), supporting further analysis using the hypomorphic allele.

Next, we examined directly whether heterochromatin assembly is impacted. To this end, we focused on the H3K9me2 mark, which signals heterochromatin formation and can accumulate without major changes in gene expression⁴⁹. This allows us to examine whether the loss of nucleation-distal silencing we observe is due to a loss of heterochromatin spreading or a loss of gene-silencing per se. We performed H3K9me2 ChIP-seq analysis in wild-type and the mutants $\Delta fkh2$, $\Delta prw1$, *clr6-1*, and *clr3-D232N* and analyzed the data in two independent ways: First, we produced input-normalized signal tracks, plotting mean and 95% confidence interval per genotype calculated from multiple replicates (**Fig 1.5D–1.5I**, top panels; see Methods). Second,

we conducted a differential enrichment analysis that examines 300bp windows along the genome containing above-background signal for significantly different accumulation of H3K9me2 between each mutant and the wild-type (**Fig 1.5D–1.5I**, Bottom panels; see Methods). We define heterochromatin spreading defects as the differential, distance dependent loss of H3K9me2 over genomic features annotated in light grey (non-nucleator features) relative to genomic features containing the nucleation elements (annotated in dark grey) (**Figs 1.5D–1.5F** and **S1.9**).

Principal Component Analysis (PCA) on the overall phenotype revealed that mutant isolates segregated from the wild-type along PC1. *Clr6* mutants also diverge from wild-type along PC2 (**Fig S1.9A**). Focusing on the signal tracks as well as the differential enrichment analysis, we found that the three *Clr6*-related mutants, *Δfkh2*, *Δprw1*, and *clr6-1*, show very strong defects in heterochromatin spreading at most, but not all, heterochromatic locations in the genome (**Figs 1.5D–1.5J** and **S1.9B–S1.9F**). We independently validated these effects by ChIP-qPCR, additionally examining the *Δfkh2Δprw1* double mutant (**Fig S1.10**). The effects are most prominent at pericentromeres and sub-telomeric regions, as evidenced both by separation of the 95% confidence intervals of the mutant versus wild-type signal tracks and the differential enrichment analysis in the non nucleator regions (light gray, **Figs 1.5D–1.5F** and **S1.9B–S1.9E**). *Clr6* mutants also have strong effects at heterochromatin islands, with severe loss of H3K9me2 (**Fig 1.5G–1.5I**). Critically, *Clr6* mutants show minimal defects in H3K9me2 accumulation at nucleation sites (dark gray), especially those driven by RNAi, *i.e.* *cenH* at *MAT*, the *dg* and *dh* repeats at the pericentromere, and homologous repeats at the subtelomeric *tlh1/2* gene (**Figs 1.5D–1.5F**, **1.5J**, **S1.9B–S1.9E**, and **S1.11**), further reinforcing the notion that *Clr6* complexes largely do not contribute to heterochromatin assembly during nucleation, but instead are essential for spreading.

Interestingly at the MAT locus, the effect tends to be restricted to regions that are centromere-distal to *cenH* (**Figs 1.5J** and **S1.9B**), near the location of “orange” (**Fig S1.1**). This effect on spreading does not appear to impact the region near *REII*, which is centromere-proximal relative to *cenH*. This may indicate that Clr6 works redundantly with other regulators at the *MAT* locus to promote heterochromatin spreading. We also tested if the relatively localized effect of on H3K9me2 to the right side of *cenH* is an artefact of the “orange” reporter insertion. We generated *clr6-1* and $\Delta prw1$ without any reporter genes and found, similar to *MAT* $\Delta REIII$, a reduction in H3K9me2 accumulation to the right of *cenH* (**Fig S1.11**). This indicates that the loss H3K9me2 observed in the ChIP-seq is not due to the insertion of reporters.

In contrast, *clr3-D232N* shows strong H3K9me2 accumulation defects at all major nucleation centers as well as the distal regions (**Fig 1.3E–1.3H**), even though some residual H3K9me2 is evident at nucleation centers. This is consistent with the view that spreading is dependent on successful heterochromatin assembly at nucleation sites. The sole exception are heterochromatin islands, where surprisingly, *clr3-D232N* shows increased H3K9me2 accumulation, possibly due to redistribution from RNAi nucleation centers elsewhere (**Fig 1.5G–1.5I**).

We further analyzed the different impact of Clr6 and Clr3 on H3K9me2 at nucleation sites and distal regions using volcano plots. We compared differential H3K9me2 enrichment in $\Delta fkh2$, $\Delta prw1$, *clr6-1*, and *clr3-D232N* relative to wild-type (**Fig S1.12A–S1.12H**). While all mutants have significantly reduced enrichment relative to wild-type at distal sites subject to spreading, these plots reveal key features that separate the phenotype of the Clr6C mutants from *clr3-D232N*: We find, (1) that nucleation center sequences are significantly reduced in the *clr3-D232N* versus wild-type comparison, but not in Clr6 complex mutant compared to wild-type. This further indicates that *clr3-D232N*, but not Clr6 mutants, show significant H3K9me2

accumulation defects at nucleation centers. In addition, this analysis reveals (2) that, in comparison to wild-type, *clr3-D232N* shows significantly increased H3K9me2 enrichment at euchromatic sites, namely islands, which is absent for the Clr6-related mutants (**Fig S1.12D and S1.12H**).

Finally, we assessed if these effects on H3K9me2 in Clr6 mutants are also evident for the major repressive mark, H3K9me3. We conducted H3K9me3 ChIP-qPCR and examined *MAT*, telomere, islands and a pericentromere II-distal locus (**Fig S1.13**). Our results show that H3K9me3 is depressed at distal sites in *clr6-1* and $\Delta fkh2$ relative to wild-type. This is consistent with our prior work on H3K9me spreading within *MAT*²⁴, showing H3K9me3 declines in concert with H3K9me2 at nucleation-distal sites. This is not surprising, since H3K9me3 is required for H3K9me2 spread via the Clr4 chromodomain^{18,49}. Overall, these analyses reinforce the view that Clr6 primarily acts by promoting nucleation-distal spreading of H3K9me. This effect is highly localized within *MAT*, indicating either that Clr6 largely impacts gene silencing functions that are downstream from heterochromatin assembly, or multiple redundant factors work in concert with Clr6 to spread H3K9me at *MAT*.

Fkh2 is part of several Clr6 complexes *in vivo*

Fkh2 was previously shown to physically associate with Clr6⁴⁷, and we confirmed that Fkh2 associates with Clr6, and also Sds3 by co-immunoprecipitation (**Fig S1.14A**). The co-immunoprecipitation with Sds3 suggests that Fkh2 can associate with Clr6 I complexes, which are typified by Sds3 (**Fig S1.14A**)⁴⁴. To assess whether Fkh2 stably integrates into Clr6 complexes, we performed sucrose gradient fractionations of cellular lysates, similar to prior analyses⁴⁴, using a Fkh2-TAP fusion and epitope-tagged Clr6 (Clr6-13MYC; Fkh2-TAP) or epitope tagged Sds3 (TAP-Sds3; Fkh2-13MYC). Our results can be summarized as follows: Fkh2 likely associates with Clr6 complexes Clr6 I⁴⁴, the related Clr6 I' complexes⁴⁷, as well as

Clr6 II. We based this assessment on the fact that Fkh2-TAP co-migrates with at least two Clr6 complexes, a smaller and a larger complex. The large complex migrates in fraction 10 in the Fkh2-TAP: Clr6-13MYC experiment (**Figs 1.6A and S1.14C**), and peaks in fractions 9–10 in the TAP-Sds3: Fkh2-13MYC experiment (**Fig S1.14B**). Given that this fraction contains the peak of Sds3, it likely represents a mixture of the large complexes I' and I"⁴⁴. Separately, Fkh2 associates with a smaller Clr6 complex in fractions 5–7 in the Fkh2-TAP:Clr6-13MYC experiment (most abundant in fraction 7), which based on prior analysis⁴⁴ likely represents Clr6 II. Fkh2-TAP also migrated in an apparent free form (fraction 2, **Fig 1.6A**), consistent with its role as a transcription factor^{50,51}. Next, we sought to address if this co-migration indicates stable Clr6 complex association. We predicted that the migration pattern of Fkh2 would change in mutants of core Clr6 complex members. When we performed sucrose gradient analysis with Fkh2-13MYC (as opposed to Fkh2-TAP above) in the *Δprw1* mutant, we found that the peaks associated with bound, but not free, Fkh2-MYC are shifted towards lower molecular weight by one fraction; this was seen for both, large and small Clr6 complexes (**Fig 1.6B**). We note that in this experiment, more Fkh2-MYC was detected in lower molecular weight migrating complexes. Therefore, we conclude that Fkh2 is a bone fide member of Clr6 complexes.

Fkh2 helps direct Clr6 to nucleation-distal heterochromatin sites

We next sought to understand how Fkh2 helps Clr6 spread H3K9me2 or gene silencing. One trivial possibility is that Fkh2 promotes the transcription of major heterochromatin components, independent of its association with Clr6 complexes. To test this notion, we performed RT-qPCR for 9 heterochromatin regulators, which were chosen to represent the major complexes ClrC, RITS, Clr6, and SHREC. We also separately queried the key heterochromatin assembly factor gene *swi6*. We do not observe any significant reduction of these transcripts in *Δfkh2* compared to wild-type (**Fig S1.15**), suggesting that Fkh2 acts via another mechanism. We next tested whether Fkh2 affects the chromatin localization of Clr6. Using ChIP, we tracked the chromatin

association of Clr6-13MYC at various heterochromatic loci in *WT* or $\Delta fkh2$ in the *MAT* $\Delta REIII$ heterochromatin spreading sensor background. At the *MAT* locus, Clr6-13MYC was efficiently detected above background signal (untagged control) at *cenH* “green” or at *mtd1*, a euchromatic gene outside the *IR-R MAT* boundary. At these loci, Clr6 recruitment was unaffected by the absence of Fkh2 (**Fig 1.6C**). However, at “green”-distal sites, namely the “orange” reporter and a more boundary proximal site (“*MAT* distal”), *fkh2* deletion reduced Clr6 localization. Similarly, $\Delta fkh2$ affected Clr6 localization at the heterochromatin islands *mei4*, *mcp7*, and *ssm4* (**Fig 1.6D**). At telomeres, where $\Delta fkh2$ also had a significant impact on H3K9me2 spreading, we also found a significant reduction in Clr6 chromatin association at distal sites (**Fig 1.6E**, 30kb) but not at the euchromatic control locus, *act1* (**Fig 1.6F**). Therefore, it appears that one role of Fkh2 in promoting heterochromatin spreading is to strengthen the recruitment of Clr6 to nucleation-distal heterochromatic sites.

Discussion

The formation of a heterochromatin domain requires three interconnected steps: DNA sequence driven nucleation, assembly of heterochromatin structures, and the lateral spreading to neighboring regions. It remains poorly understood whether the distal propagation of gene silencing or the heterochromatin structure itself has locus-specific requirements, and whether the genetic circuitry directing proximal and distal events overlap or are separable. Our reporter allows us to separate requirements for nucleation-proximal and distal silencing and thereby pinpoint which factors are necessary to drive or restrain it at different genomic loci. A key finding is that variants of the Clr6 HDAC complex are specifically involved in distal heterochromatin spreading and/or silencing. In contrast, a broad class of chromatin remodelers antagonize nucleation-distal heterochromatin silencing. Additionally, we find that different chromatin contexts have specific requirements for distal silencing. For example, the SAGA complex promotes heterochromatin spreading in a euchromatic context.

Several HDACs are involved in heterochromatin regulation in fission yeast, Clr6, Clr3 and Sir2. Of those, we find that Clr6 has a disproportionate effect on nucleation-distal sites. In contrast, the striking loss of silencing and H3K9me2 accumulation at nucleation sites in *clr3* mutants indicate that Clr3 either primarily impacts nucleation, which precedes spreading, or that it affects both processes (**Figs 1.1E, 1.1G, 1.1I, 1.5 and S1.9**). We note that while Clr3 is thought to be required for silencing at nucleation centers, for example at *REIII* and *cenH*^{1,26,45}, the literature on the impact of *clr3* gene deletions on the distribution of H3K9me2 is mixed, showing either no¹ or significant loss³¹. We believe that the strong loss of H3K9me2 we observe in *clr3-D232N* closely reflects the native function of the gene, given that prior analysis of this mutation indicates a very similar degree of loss of function⁴⁵. The variable results for Δ *clr3* may reflect compensation that occurs in strains carrying null versus other loss-of-function alleles⁵². Our finding that Clr6 only affects distal silencing is consistent with the finding that the *clr6-1* allele has only small impacts

on transcription of the *cenH* nucleator-encoded ncRNAs⁵³. Our screen showed that several, but not all members, of the recently described Clr6 complex Iⁿ⁴⁷ and, to a lesser extent, other Clr6 complexes, promote spreading. Not all annotated Clr6 subunits share gain or loss of spreading phenotypes, suggesting that these subunits do not contribute to distal silencing but instead mediate other functions of the complex.

Fkh2 prominently promotes spreading of H3K9me2 at pericentromeres and sub-telomeres and at the right side of the *MAT* locus. We find that Fkh2 is a resident member of several Clr6 complexes, the I', I'', and II types (**Fig 1.6A** and **1.6B**). These results indicate two possible, nonexclusive interpretations: 1. the composition of different Clr6 subcomplexes *in vivo* is more dynamic than previously thought; 2. a number of different, preassembled Clr6 complexes can associate with Fkh2, which imparts a role in spreading regulation. Interestingly, the Set3-submodule that typifies the Rpd3L-Expanded complex⁵⁴ has a distinct spreading-antagonizing behavior (**Fig 1.4C**). This is in contrast with prior findings on the Set3 complex, where it was shown to exhibit a mild positive role at pericentromeres⁵⁵. Taken together, our data suggest a division of labor between Clr3 and Clr6, with Clr3 majorly impacting heterochromatin assembly at nucleation sites and Fkh2-containing Clr6 complexes function to spread heterochromatin structures and/or silencing outward (**Fig 1.6G**). However, a formal possibility remains that these deacetylases function in similar ways, with the activity of Clr6 at nucleation sites masked by the activity of other HDACs. The observation that heterochromatin spreading at the *MAT* locus is weakly affected while gene silencing is strongly affected indicates that other pathways, such as FACT^{38,56}, may act redundantly with Clr6 in heterochromatin spreading. It is also possible that Clr6 is primarily involved in distal propagation of gene silencing via its deacetylation function, which when lost indirectly weakens heterochromatin at certain loci.

What mediates the spreading-specific role of Clr6 complexes? One possible explanation is that they act in conjunction with the histone chaperone Asf/HIRA, which cooperates with Clr6 in gene silencing at ncRNA nucleators⁵³. However, we do not favor the idea that this pathway mediates distal silencing, since Asf/HIRA subunits Hip1, Hip3 and SIm9 have mild or no phenotypes for distal silencing in *MAT* contexts. Asf/HIRA mutant phenotypes were more pronounced in *ECT*, a context that is less reliant on Clr6 for spreading (**Fig 1.1**, see below). We believe that Fkh2 plays a key role in imparting this spreading-specific role for Clr6. Fkh2 is a transcription factor that regulates meiotic genes in *S. pombe*^{50,51,57}. However, the observation that loss of Fkh2 impacts H3K9me2 spreading at non-nucleator sites (over grey feature annotations, **Figs 1.5** and **S1.9B–S1.9E**) raises two possibilities: 1. Fkh2 acts via its canonical sequence binding capacity. In this case, Fkh2 may exhibit DNA binding that is more degenerate than the consensus motif, or it may bind its canonical consensus sequence and regulate chromatin architecture. In support of the first, while Fkh2 is described as a DNA binding transcription factor that recognizes specific motifs^{57,58}, Fkh2 appears to be found on many regions of the chromosome, including at the left side of the pericentromere (*cen II*), the *MAT* locus and several other locations (genome browser, Pombase tracks from⁵⁸). Alternatively, rather than binding locally along chromatin, Fkh2 may also act as a chromatin organizing protein, as has been previously shown⁵⁹. It is conceivable that Fkh2 creates chromatin environments that are conducive to nucleation-distal Clr6 recruitment, either by tethering to a nuclear compartment such as the nuclear periphery³⁸ or via chromatin conformational or biophysical changes^{60,61}. 2. It is possible that Fkh2 acts in a transcription factor-independent fashion, recognizing features of nucleation-distal regions through regions other than its sequence-specific binding domain. Instances of transcription factors executing key functions independent of DNA binding, but via protein-protein interactions, have been demonstrated for example in plants⁶². We find that Fkh2 promotes the recruitment of Clr6 complexes to the spreading zone (**Fig 1.6C–1.6E**). The spreading-specific role of Clr6 complexes may be

additionally supported by other known recruitment mechanisms, for instance a pathway involving HP1/Swi6^{2,5,63}. While the precise mechanism of Fkh2-mediated Clr6 recruitment will be the subject of further studies, our results unambiguously demonstrate that Fkh2 typifies a specific functional mode of the conserved HDAC Clr6/RPD3 among its numerous essential activities in gene regulation⁶⁴. Given that Fkh2 resides within Clr6 complexes (**Fig 1.6A and 1.6B**), we favor the view that it directly participates in regulating spreading of gene silencing or H3K9 methylation.

Beside the positive regulation of heterochromatin spreading detailed above, our results show that several classes of chromatin remodelers, including Ino80, Swr1C, SWI/SNF and RSC, antagonize nucleation-distal silencing. This broad antagonism contrasts with more specific functions uncovered previously for Ino80/Swr1C³⁷. As seen for Clr6, not all subunits in remodeling complexes show a spreading phenotype. Remodelers have been implicated in negatively regulating heterochromatin function by creating specific nucleosome free regions (NFRs,⁶⁵) that antagonize heterochromatin. Since NFRs may be roadblocks to spreading^{66,67}, it is possible that remodelers employ this mechanism to restrain heterochromatin spreading globally. In addition, remodelers such as SWI/SNF and RSC generally destabilize nucleosomes^{68,69}, leading to increased turnover⁷⁰, which would antagonize heterochromatin spreading. This increased turnover may be tolerated at ncRNA nucleation sites, where turnover is at near euchromatic levels²⁴, likely due to ncRNA transcription^{29,71}. This would suggest that regulation of nucleosome stability has a particular significance at distal, but not nucleation sites.

Beyond the finding of Clr6 and remodelers in promoting and antagonizing heterochromatin spreading, respectively, this study uncovered several locus- and nucleator-type-specific pathways. Here we would like to highlight two main observations:

1. Distinct factors are required for similar nucleators in different chromatin environments. *ECT* and *MAT ΔREIII* are both driven by related ncRNA nucleators (*dh* and *cenH*, respectively) and have remarkably similar behaviors with respect to nucleation and spreading across the cell population²⁴. Efficient spreading, specifically at *ECT*, requires Hip1, and moderately SIm9, which code for a key subunits of the HIRA H3/H4 chaperone. HIRA has been implicated in stabilizing heterochromatic nucleosomes⁵³. Hence, given that transcribed chromatin is known to destabilize nucleosomes, it seems likely that this specific requirement reflects the challenge faced by heterochromatic domains when expanding within gene-rich chromatin. *ECT* is also particularly reliant on the SAGA complex for spreading (**Figs 1.4A** and **S1.4**). This may seem counterintuitive initially, as SAGA has been shown to be recruited by Epe1 to antagonize heterochromatin assembly at constitutive sites⁷². In fact, in our screen SAGA plays a less prominent role in the *MAT* context. This requirement for SAGA at *ECT* may be connected to the observation that SAGA can modulate the chromatin recruitment of remodelers, such as SWI/SNF, via direct acetylation⁷³. Therefore, one possible explanation that remains to be tested for the SAGA phenotype we observe is acetylation of SWI/ SNF and possibly other remodelers that antagonize spreading, releasing them from chromatin.

2. Spreading from qualitatively different nucleators within the same environment, namely *REIII* and *cenH*, also differs in sensitivity to different mutants. The significant overlap in factors between *WT MAT* and *MAT ΔREIII* indicates that heterochromatin formation at *MAT* is dominated by the ncRNA nucleator *cenH*, in agreement with our previous findings²⁴. The *REIII* element, which nucleates heterochromatin independent of ncRNA²³, has different requirements. For example, ncRNA-independent spreading at *REIII* (*MAT ΔcenH*) is uniquely promoted by the TORC2 pathway Gad8 kinase, consistent with a previous report implicating Gad8 for *MAT* silencing⁷⁴. While Gad8 is reported to target Fkh2 for phosphorylation, *Δfkh2* has very weak effects on *MAT ΔcenH*. Other potential phosphorylation targets of Gad8 in promoting spreading from *REIII*, if it acts through its kinase function, remain to be established. We note that *REIII* can

confer a high propensity for local intergenerational inheritance of silencing^{24,39}. Therefore, a formal possibility for spreading defects in the *MAT ΔcenH* context, or others with high intergenerational stability, is that the genes identified are required for the maintenance of silencing outside the nucleator, rather than the initiation of silencing across the distal locus.

In this work, we defined the regulation of nucleation-distal gene silencing, which has specific chromatin context-dependent requirements that are separate from the regulation of silencing at nucleation centers. While similar nucleation elements likely rely on common mechanisms, the success of heterochromatin mediated distal silencing appears to depend on the chromatin context and particularly differs in gene-rich versus gene-poor chromatin. Our findings have implications for directing gene silencing during cellular differentiation. In this situation, regions that have previously been in a transcriptionally active state are invaded by heterochromatin and will therefore compete for core spreading factors in a dosage limited system^{75,76}. We note that several of the factors we identify as critical to regulating spreading in euchromatic environments are conserved in metazoans, indicating that they may contribute to differentiation through heterochromatin control in these organisms.

Methods

Mutant generation for genetic screen

We generated a 408 gene deletion mini-library that represents a subset of the *S. pombe* Bioneer deletion library, focused on nuclear function genes. The library (**Table S1.1**) was assembled via three criteria: 1. ~200 genes coding for proteins have a “nuclear dot” appearance in a high throughput YFP- tagged “ORFeome” screen (⁷⁷, also used in ³⁴). 2. ~50 deletions of central *S. pombe* DNA binding transcription factors. 3. ~150 gene deletions selected based on their annotation as chromatin regulation-related functions (majority of this set), or prior preliminary data indicating a role in heterochromatin function. Deletions that grow poorly in rich media were eliminated. Several Bioneer collection mutants were independently validated and produced *de novo*. For the ectopic locus HSS reporter strain, the screen was performed essentially as described⁸. Briefly, the parent HSS reporter strain was crossed to the library. Crosses were performed as described^{8,24,40,78} using a RoToR HDA colony pinning robot (Singer). For the *MAT* HSS reporter strains, the screen was performed essentially as described⁸ with the exception that crosses were generated using a 96 well manual pinner. Note that the *MAT* we used an OFF isolate for $\Delta cenH$ ²⁴. This is because $\Delta cenH$ behaves in a bimodal fashion, producing stable ON (no heterochromatin) and OFF (heterochromatin) alleles at *MAT*. *MAT* $\Delta cenH$ isolates were picked absent any selection based on their “green” and “orange” profiles in flow cytometry²⁴. In addition, three $\Delta clr4$ mutant isolates and six individual parent isolates from each genomic context were included as controls. Crosses for the ectopic HSS strains were performed using SPAS media for 4d at room temperature, while for the *MAT* HSS strain crosses were performed on ME media for 3d at 27°C. For all strains, crosses were incubated for 5d at 42°C to retain spores, while removing unmated haploid and diploid cells. The ectopic HSS spores were germinated on YES medium supplemented with G418, hygromycin B, and nourseothricin. For *MAT* HSS strains, spores were germinated on YES medium

supplemented with G418 and hygromycin B. The resulting colonies were pinned into YES liquid medium for overnight growth and then prepared for flow cytometry as described below.

Flow cytometry data collection and normalization for genetic screen

In preparation for flow cytometry, overnight cultures were diluted to OD = 0.1 (approximately a 1:40 dilution) in rich media (YES) and incubated at 32°C with shaking of rpm for 4–6 hours. For the ectopic locus HSS strains, flow cytometry was performed essentially as described^{8,24}. For the *MAT* locus HSS strains, flow cytometry was performed using a Fortessa X20 Dual instrument (Becton Dickinson) attached with high throughput sampler (HTS) module. With a threshold of 30,000 events, samples sizes ranged from ~1000 to 30,000 cells depending on strain growth. Fluorescence detection, compensation, and data analysis were as previously described^{8,24}. Flow data derived from the genetic screen for individual strains are represented as 2d density hexbin plots in **Figs 1.1, 1.2, 1.4, 1.5, S1.2, S1.4, S1.7, and S1.8**. Dashed red and blue guidelines respectively indicate median minus 2SD of “green”/ “orange”-On cells ($\Delta clr4$ control cells with normalized fluorescence above 0.5) and median plus 2SD of “green”/ “orange”-Off cells (“red”-Only control).

Spreading analysis

Nucleated cells were extracted using a “green”-off gate, using median of a “red”-only control plus 2 times the SD. Enrichment of cell populations in particular “orange” fluorescence ranges (Grid_n) are calculated as Grid_n^{mut/par}: fraction of mutant population is divided by the fraction of parent population in one grid. The intervals of “orange” fluorescence used in grids are determined by: median plus 2SD of “orange”-Off cells (“red”-Only control), median minus 2 SD of “orange”-On cells ($\Delta clr4$ control cells with normalized fluorescence above 0.5) and the median of the two. For *ECT*, instead of using a “red”-Only control strain, we adjusted the fluorescence value of a fluorescence-negative (unstained) strain by the “red” fluorescence from

the $\Delta clr4$ control. To evaluate gain of spreading phenotype, enrichment in Grid 1 in *WT MAT*, *MAT $\Delta REIII$* and *ECT* were calculated. To evaluate loss of spreading phenotype, enrichment in Grid 3 and 4 in *MAT $\Delta cenH$* and *WT MAT* as well as Grid 4 in *MAT $\Delta REIII$* and *ECT* were calculated. The distribution of the $Grid_n^{mut/par}$ were plotted as swarmplots with annotation of the 85th percentile and median plus 2SD of parent isolates $Grid_n^{mut/par}$. Gene hit lists comprised mutations above median and 2SD within the 85th percentile. Upset plots were generated using the R package UpSetR⁷⁹. Beeswarm plots were plotted using the R packages ggbeeswarm⁸⁰.

GO complex and sub-complex analysis

Generating the heatmap count data

GO Complexes—Based on the GO Complex annotations

[https://www.pombase.org/data/annotations/Gene_ontology/GO_complexes/] retrieved from Pombase^{42,81}, GO complex membership was determined for genes identified as hits for each strain background and hit category (gain/loss). Briefly, using functions from the R package dplyr (Wickham H., François R., Henry L. and Müller K. (2020). dplyr: A Grammar of Data Manipulation. R package version 0.8.4. <https://CRAN.R-project.org/package=dplyr>), gene names were converted to systematic ID numbers and these systematic IDs were queried against the GO complex annotation table. The number of times a GO complex appeared per background and hit category was tabulated. Genes can be associated with any number of GO complexes depending on their annotations. However, each gene was only counted once per GO complex despite potentially being annotated to that GO complex by more than one evidence code. The unique list of GO complexes for all hits was determined and a matrix was computed representing the number of times each GO complex (row) was identified per strain/hit category (column). This counts matrix was used to generate the GO complex heatmap in **Fig 1.3**, described below. Hit tables—Genes annotated to the seven complexes in **Fig 1.4A, 1.4C** and **1.4E** were obtained from Pombase⁴². fkh2 was added to the Clr6 I” complex given the protein

contacts described previously⁴⁷. For the unique set of genes per panel it was determined if each gene was identified as a hit in each strain background/hit category combination. The data was summarized in a counts matrix where rows represent the unique list of genes per panel and columns represent the strain background / hit category. The counts matrix for each set of genes was used to generate the heatmaps in **Fig 1.4A, 1.4C** and **1.4E** as described below.

Generating the heatmap clustering

Using the R package ComplexHeatmap⁸², both row and column dendrogram and clustering were generated using hierarchical clustering. Based on an optimal Silhouette score, the strain background / hit category (columns) were clustered into 2 clusters. The dendrogram representing complexes (**Fig 1.3**) or genes (**Fig 1.4A, 1.4C** and **1.4E**) in rows were not separated because validations of the clustering by connectivity, Dunn index or Silhouette score were inconclusive. Clustering validations were conducted using the R package cValid (Brock, G., Pihur, V., Datta, S. and Datta, S. (2008) cValid: An R Package for Cluster Validation Journal of Statistical Software 25(4) URL: <http://www.jstatsoft.org/v25/i04>).

Validation of strains and plasmid construction

Plasmid constructs for gene knockout validation in HSS background strains were generated by *in vivo* recombination as described^{8,24}. *S. pombe* transformants were selected as described²⁴. For microscopy, *hygMX super-folder GFP (SFGFP)* constructs for C-terminal tagging we described previously³³ were amplified with 175bp ultramer primers with homology to *apm3* or *apl5* and transformed into a *Swi6:E2C kanMX* strain. *Apm3:SFGFP;Swi6:E2C* and *Apl5:SFGFP;Swi6:E2C* strains were selected on hygromycin B and G418. For validations in PAS100 (wild-type, no HSS): *clr6-1*(PAS933) was generated by CRIPSR/Cas9 editing as described⁸³. *Aprw1*(PAS932) was generated by first outcrossing the HSS from PAS799 and then crossing the progeny to PAS100. Integrations and gene knockout were confirmed by PCR

and sequencing (*clr6-1*). Strains generated for this study beyond the screen can be found in **Table S1.2**.

Flow cytometry data collection and normalization for validation

For validation of flow cytometry experiments, cells were grown as described^{8,24} with the exception that cells were diluted into YES medium and grown 5–8 hours before measurement. Flow cytometry was performed as above. Depending on strain growth and the volume collected per experiment, fluorescence values were measured for ~20,000–100,000 cells per replicate. Fluorescence detection, compensation, and data analysis were as described^{8,24,33} with the exception that the guide-lines for boundary values of “off” and “on” states were determined using median of a Red-Only control plus 3 times the median absolute deviation (MAD) and median of $\Delta clr4$ minus 2 times the MAD value respectively. Validation flow cytometry plots were generated using the ggplot2 R package⁸⁴.

Chromatin immunoprecipitation and quantification

Chromatin Immunoprecipitation (ChIP) was performed essentially as described^{8,24}. Bulk populations of cells were grown overnight to saturation in YES medium. For anti-H3K9me2 ChIP, the following morning, cultures were diluted to OD 0.1 in 25mL YES and grown for 8h at 32°C and 225rpm. Based on OD measurements, 60×10^6 cells were fixed and processed for ChIP as previously described²⁴ without the addition of W303 carrier. For anti-MYC ChIP and anti-H3K9me3 ChIP, 40mL cultures were grown to OD 0.4–0.7 and then incubated. Cells for anti-MYC ChIP were lysed as described²⁴, except that cells were bead mill homogenized for 9 cycles. Cleared chromatin for anti-H3K9me2, anti H3K9me3, or anti-MYC ChIP samples was incubated with either 1µL of anti-H3K9me2 antibody (Abcam, ab1220), 1µL of antiH3K9me3 antibody (Millipore 07–442, lot 3782120), or 2µL anti-MYC antibody (Invitrogen, MA1-980, lot VL317116) overnight after a small fraction was retained as Input/WCE. DNAs were quantified by

qPCR. For H3K9me2 and H3K9me3, percent immunoprecipitation (%IP, ChIP DNA/Input DNA) was calculated as described²⁴, except for **Fig S1.6**, where a ratio of % IP queried locus/%IP act1 is plotted. For anti-MYC ChIP, enrichment is presented as the ratio of %IP in PAS867 or 868 (*Clr6:13XMYC* in PAS 332 *WT* or *Δfkh2*) over %IP in PAS332 (untagged). Data was plotted in Prism (GraphPad). For comparison of different preparations of ChIP samples, %IP of mutant divided by %IP of wildtype was calculated.

ChIP-seq data collection, library preparation and sequencing

ChIP was performed essentially as above, with the following exceptions: From 60 mL cultures, 300x10⁶ cells in logarithmic phase were fixed and processed. Sheared chromatin samples were not pre-cleared with Protein A Dynabeads, and the chromatin was directly treated with 2μL of anti-H3K9me2 antibody (Abcam 1220, Lot GR3308902-4). Barcode-indexed sequencing libraries were generated from reverse-crosslinked ChIP-DNA samples using a Kapa Hyper DNA Library Preparation Kit (Kapa Biosystems-Roche, Basel, Switzerland) and NextFlex UDI adapters (PerkinElmer, Waltham, MA). The libraries were amplified with 16 PCR cycles and cleaned with SPRI bead protocol according to the instructions of the manufactures. The fragment lengths of the sequencing libraries were verified via micro-capillary gel electrophoresis on a LabChip GX Touch system (PerkinElmer). The libraries were quantified by fluorometry on a Qubit instrument (LifeTechnologies, Carlsbad, CA), and combined in a pool at equimolar ratios. The library pool was size-selected for library molecules in the lengths of 200 to 450bp using a Pippin-HT instrument (Sage Science, Beverly, Massachusetts). The success of the sizeselection was verified on a Bioanalyzer 2100 instrument (Agilent, Santa Clara, CA). The pool was quantified with a Kapa Library Quant kit (Kapa Biosystems-Roche) on a QuantStudio 5 real-time PCR system (Applied Biosystems, Foster City, CA) and sequenced on a Illumina NextSeq 500 (Illumina, San Diego, CA) run with paired-end 40bp reads.

ChIP-seq data analysis

Data processing for ChIP-seq analysis was performed as follows. Trimming of sequencing adaptors and sliding window quality filtering were performed using Trimmomatic v0.39⁸⁵. Filtered and trimmed paired-end (PE) reads were aligned to the *S. pombe* genome (Wood et al. 2002) with Bowtie2 v2.4.2⁸⁶ using standard end-to-end sensitive alignment. An additional 6bp was trimmed from the 5' end of each read prior to alignment. Sorted, indexed bam files were generated using SAMtools v1.12⁸⁷. Duplicate reads were marked with Picard tools v2.25.2 "MarkDuplicates" command. Filtered bam files were generated with SAMtools "view" with the following flags [-bh -F 3844 -f 3 -@ 4 I II III mating_type_region] to retain only properly paired reads on the listed chromosomes/contigs, and remove duplicate reads. The resulting filtered bam files were sorted and indexed with SAMtools and used for downstream genome-wide analysis. Input-normalized BigWig files for signal tracks for 25bp bins were generated from the filtered bam files with the bamCompare function from deeptools v3.5.1⁸⁸. To do so, the following flags were used: [-outFileFormat bigwig--scaleFactorsMethod readCount--operation ratio--pseudocount 1--extendReads--samFlagInclude 64--skipZeroOverZero--binSize 25--numberOfProcessors 4--effectiveGenomeSize 12591546 --exactScaling]. Fragments were counted once by including only the first mate of each pair and extending to the fragment size. For each genotype, 2 or 3 biological replicates were processed for downstream analysis. Initial whole genome clustering analyses on ChIP and Input samples and inspection for low signal to noise ratio in IGV prompted us to remove two outlier samples, one *clr6-1* and wild-type respectively. BigWig files were imported into R v4.0.3 with rtracklayer v1.50.0⁸⁹. BigWig files were used to generate signal tracks comprised of the mean and confidence interval for each genotype in custom genome browser plots generated with the DataTrack() command from the Gviz Bioconductor package v1.34.1⁹⁰. As described previously⁸, gene annotations were imported from PomBase⁴² and converted to genomic coordinates in R v3.5.1 with the makeTxDbFromGFF function from GenomicFeatures v1.32.3⁹¹ and saved out to an sqlite file. This

sqlite file was imported into R v4.0.3 and used to generate feature annotations for signal tracks in Gviz with the AnnotationTrack() command. Reads from the filtered bam files for CHIP samples were counted into either 300bp windows or 5kb bins using windowCounts() function from the Bioconductor package csaw v1.24.3⁹². Regions +/-1.5kb surrounding the following features (*ade6*, *ura4*, *fkh2*, *prw1*, *mat1-Mc*, *mat1-Mi*) were blacklisted as they represent experimental artifacts—*ade6* and *ura4* because their promoter and terminator regions are present in the reporter cassettes, *fkh2* and *prw1* because these gene's ORFs were entirely removed in certain genetic backgrounds and *mat1* genes because these regions are expressed but homologous to those found in the heterochromatic *MAT* locus. Global background was determined from 5kb bin count matrices and interpreted onto the 300bp windows with the csaw filterWindowsGlobal() function. Only 300bp windows where the abundance exceeded a filtering threshold of 1.7 times the global median were retained resulting in 1500 windows for further analysis.

Differential Enrichment analysis was performed on these 1500 300bp windows using the DESeq2 Bioconductor package v1.30.1⁹³. Size Factors were calculated on the count matrices in the global 5kb bins with the estimateSizeFactors() function and applied on the global enrichment filtered 300bp windows. The model matrix for the experimental design was constructed based on genotype. Normalized counts per bin were obtained with the vst() function from DESeq2 with the parameter blind = FALSE. VST transformed counts were used as an input to principal component analysis via the prcomp() R function on the top 500 most variable bins (as adapted from RNA-Seq differential enrichment workflows), or all 1500 bins. PCA plots were generated with ggplot2 v3.3.3⁸⁴. Differential Enrichment analysis, including estimating dispersions and fitting of a negative binomial generalized linear model, was performed with the DESeq() function. Results for pairwise contrasts between genotypes were extracted as GRanges objects with the results() function. Each of the 1500 windows was annotated as belonging to global or

heterochromatin location specific nucleation/spreading/euchromatic/ other categories. Volcano plots were generated with ggplot2 for each comparison by plotting $-\log_{10}(\text{padj})$ against $\log_2\text{FoldChange}$ values. Each dot represents a 300bp region tested for differential enrichment. Dots are colored by their location annotation. Coordinates for nucleator regions are derived from feature coordinates from PomBase adjusted to a multiple of 300 so that a 300bp bin can only be annotated to one category of feature. Coordinates for spreading are defined to be between or outside of nucleator regions. Euchromatic regions are defined as coordinate ranges identified as an “island”²⁰, “HOOD”⁹⁴, or “region”⁹⁵ as delineated in Supplemental Table S6 from⁹⁶. A threshold for significance of padj (Benjamini-Hochberg adjusted p-value) < 0.005 and $\text{abs}(\log_2\text{FoldChange}) > \log_2(2)$ was applied to the results for each comparison and these cutoff values are additionally annotated on the volcano plots. For each comparison, the number of significant regions of each category was tabulated. Regions called as significant for the comparison of each mutant to WT are annotated on the custom genome browser plots generated with the Gviz AnnotationTrack() command. A Venn diagram of regions where WT signal significantly exceeds signal from mutants was generated outside of the conda environment in R v4.0.5 with the venn R package v1.10. An additional custom analysis for the MAT locus was performed starting at the genome alignment stage. A fasta file that includes the inserted “green” and “orange” color cassettes and intact atf1/pcr1 binding sites was used to build a genome index for bowtie2. Alignment to this custom reference was performed with bowtie2 as above. Alignments were filtered with SAMtools to retain only properly paired reads. Multimapping and low-quality alignments were removed with a mapq filter of $-q 10$. In the context of this custom reference sequence, multimapping reads represent regions that align to *ura4p*, *ade6p*, and *ura4t* which are present at XFP reporter cassettes, *IR-R* and *IR-L* repetitive regions, and parts of the mating type cassettes. Duplicate reads were marked and removed with Picard tools. Sorted, and indexed bam files were generated with SAMtools. BigWig files for coverage signal tracks at 10bp resolution were generated from ChIP files using the deeptools

bamCoverage function with the following flags [`—outFileFormat bigwig—scaleFactor ##—extendReads—samFlagInclude 64—binSize 10—numberOfProcessors 4—blackListFileName cenH_blacklist.bed—effectiveGenomeSize 19996—exactScaling`]. Bam files were scaled by a custom scaling factor (replacing `##` above) that adjusts for the read count in the bam file from each sample's the full genome alignment to the read count of the bam file with the smallest number of reads in the full genome alignment. The regions included in the *cenH* element were blacklisted in this step as they are homologous to many sequences found at the centromeres and telomeres and in this analysis represent aggregate signal from all these regions. The resulting coverage BigWig files were used to generate signal tracks in R/Gviz as described above.

Microscopy

Swi6:E2C; Apl5:SFGFP and *Swi6:E2C; Apm3:SFGFP* cells were grown in YES media as described. Slides (ibidi, Cat. No. 80606) were pre-coated with 100 mg/mL lectin (SigmaAldrich, Cat. No. L1395) diluted in water by adding lectin solution to slide for 1 min. and removing supernatant. Cells growing in log-phase were applied to the slide and excess cells were rinsed off with YES. Cells were immediately imaged with a 60x objective (CFI Plan Apochromat VC 60XC WI) on a Nikon TI-E equipped with a spinning-disk confocal head (CSU10, Yokogawa) and an EM-CCD camera (Hamamatsu). Cells were imaged in brightfield and also excited with 488nm (SFGFP) and 561nm (E2C) lasers. Emission was collected using a 510/50 band-pass filter for GFP emission and a 600/50 band-pass filter for E2C emission. For the SFGFP and E2C channels, z-stacks were obtained at 0.3 μ m/slice for 11 slices total. An overlay of the maximum z-projections for SFGFP and E2C channels are shown separately from the brightfield images. Brightness and contrast were adjusted in ImageJ to clearly show both Swi6 and Apl5/Apm5 signals in the overlay. At least two isolates were imaged to confirm localization patterns.

Reverse transcription qPCR validation of context-specific spreading mutants

For validation of context-specific spreading *hits*, *saf5*, *eaf6*, *pht1*, *hip1* and *gad8* mutants were crossed to PAS217 (*WT-MAT*), PAS332 (*MAT-ΔREIII*), PAS482 (*MAT-ΔcenH*), and PAS231 (*ECT*), respectively and mating products selected for *KAN* and *HYG* (PAS217, PAS332, and PAS482) or *KAN*, *HYG*, and *NAT* resistance (PAS231). For analyzing transcriptional regulation of heterochromatin regulators via Fkh2, PAS332 or PAS798 (*Δfkh2* in PAS332) were grown as above. Two independent isolates of each strain were grown in 200μl YES in 96 well plates to log phase (OD~0.4–0.8), washed with water and flash frozen. Total RNA was extracted from cell pellets as described²⁴ using the Masterpure yeast RNA extraction kit (Lucigen). cDNA was produced from 2–3μg total RNA as described²⁴ using a dT primer and Superscript IV (Invitrogen) reverse transcriptase, followed by an RNaseH step to remove RNA:DNA hybrids. qPCR was performed with primers against *act1*, SF-GFP and mKO2, or amplicons for heterochromatin regulator transcripts indicated in **Fig S1.15**. For *act1* qPCR, the cDNA was diluted 1:60. qPCR was performed as described⁸. qPCR amplicon primers can be found in **Table S1.3**.

Sucrose gradient analysis

Sucrose gradient analysis was performed essentially as in⁹⁷, with several modifications. PAS833 (*Fkh2:13XMYC*), PAS836 (*Fkh2:TAP; Clr6:13XMYC*), or PAS837 (*Fkh2:13XMYC; Sds3:TAP*) were grown in 50ml YES to OD~ 1, spun and washed with STOP buffer (150mM NaCl, 50mM NaF, 10mM EDTA and 1mM NaN₃) and flash frozen. Cells were resuspended in 3ml ice cold HB-300 (50mM MOPS pH7.2, 300mM NaCl, 15mM MgCl₂, 15mM EGTA, 60mM glycerophosphate, 0.1mM Na₃VO₄, 2mM DTT, 1% Triton X-100, 1mM PMSF, 200μM phenantroline, pepstatin A, leupeptin, aprotinin and 1X of EDTA-free protease-inhibitor cocktail (Roche) and then lysed in the presence of 600μl 0.5mm zirconia beads (RPI) for 6X 1min, with 5 min rest on ice in between cycles, at the maximum setting in a bead mill homogenizer

(Beadruptor-12, Omni International). The lysate was clarified by spinning at 18,000 x g for 20min. 500µl clarified lysate was applied to a 4–20% sucrose gradient in gradient buffer (50mM Tris-HCl pH 7.5, 50mM KCl, 1mM EDTA, 1mM DTT, 1mM PMSF, 200µM phenantroline, pepstatin A, leupeptin, aprotinin and 1X of EDTA-free protease-inhibitor cocktail (Roche)) and spun for 20hrs at 151,000 x g (rav) at 4°C in a swinging bucket rotor (Beckman SW-41 Ti). 12x 1ml fractions were collected from the gradient and incubated for 10min at RT with 100µl 0.15% deoxycholine. Proteins were then precipitated by addition of 100µl of 50% Trichloroacetic acid and incubation on ice for 30min. Precipitates were collected by centrifugation at 16,000 x g at 4°C for 10min and pellets washed twice in ice cold acetone and then resuspended in 2X SDS-laemmli buffer and proteins separated on 1 10% SDS-PAGE gel.

Co-immunoprecipitation

100x106 PAS 835 (*Fkh2:13MYC; Clr6:TAP*) or PAS 837 (*Fkh2:13MYC; Sds3:TAP*) cells were grown, lysed and the lysate clarified as above (sucrose gradient analysis) but in the following lysis buffer: 20mM HEPES pH7.6, 150mM NaCl, 1mM EDTA, 0.5% IGEPAL NP-40, 10% glycerol, 1mM PMSF, 200µM phenantroline, pepstatin A, leupeptin, aprotinin and 1X of EDTA-free protease-inhibitor cocktail (Roche). 500µL total protein was incubated with 20µL IgG-Sepharose 6 resin (GE healthcare) for 2 hrs at 4°C with rotation. Beads were washed 4 times with lysis buffer with 350mM NaCl instead of 150mM. Proteins were eluted off washed beads in 20µL 2X SDS-laemmli buffer, separated on SDS-PAGE gels and blotted as below.

Western blot analysis

Proteins were transferred to low-fluorescence PVDF membranes (Bio-rad) at 90min at 200mA at 4°C. Membranes were blocked in 1:1 mixture of 1XPBS: Intercept PBS blocking buffer (LiCor) and then incubated with anti-PAP (Sigma, P1291, lot 92557) or anti-MYC (Biolegend, 626802, lot B274036) at 1:1,000 either overnight at 4°C or 90 min at RT. Membranes were washed 4X in

the presence of 0.2% Tween-20 and then incubated with fluorescent anti-mouse (800nm, Rockland, 610-145-003, lot 34206) and anti-rabbit (680nm, Cell Signaling, 5366P, lot 9) at 1:5,000 and 1:15,000 respectively for 1hr at RT. Membranes were washed 4X as above, transferred to 1X PBS and imaged on a LiCor Odyssey CLx imager.

Data Availability

Raw and processed CHIP-seq data is available on GEO (accession GSE184379). Code for flow cytometry, CHIP-seq data analysis, and the primary flow cytometry data are deposited in Zenodo (<https://doi.org/10.5281/zenodo.6499338>). Software version information will be included in conda environment yml files (2021_seqTools.yml for command line data processing and 2021_Renv.yml for analysis via R/Bioconductor).

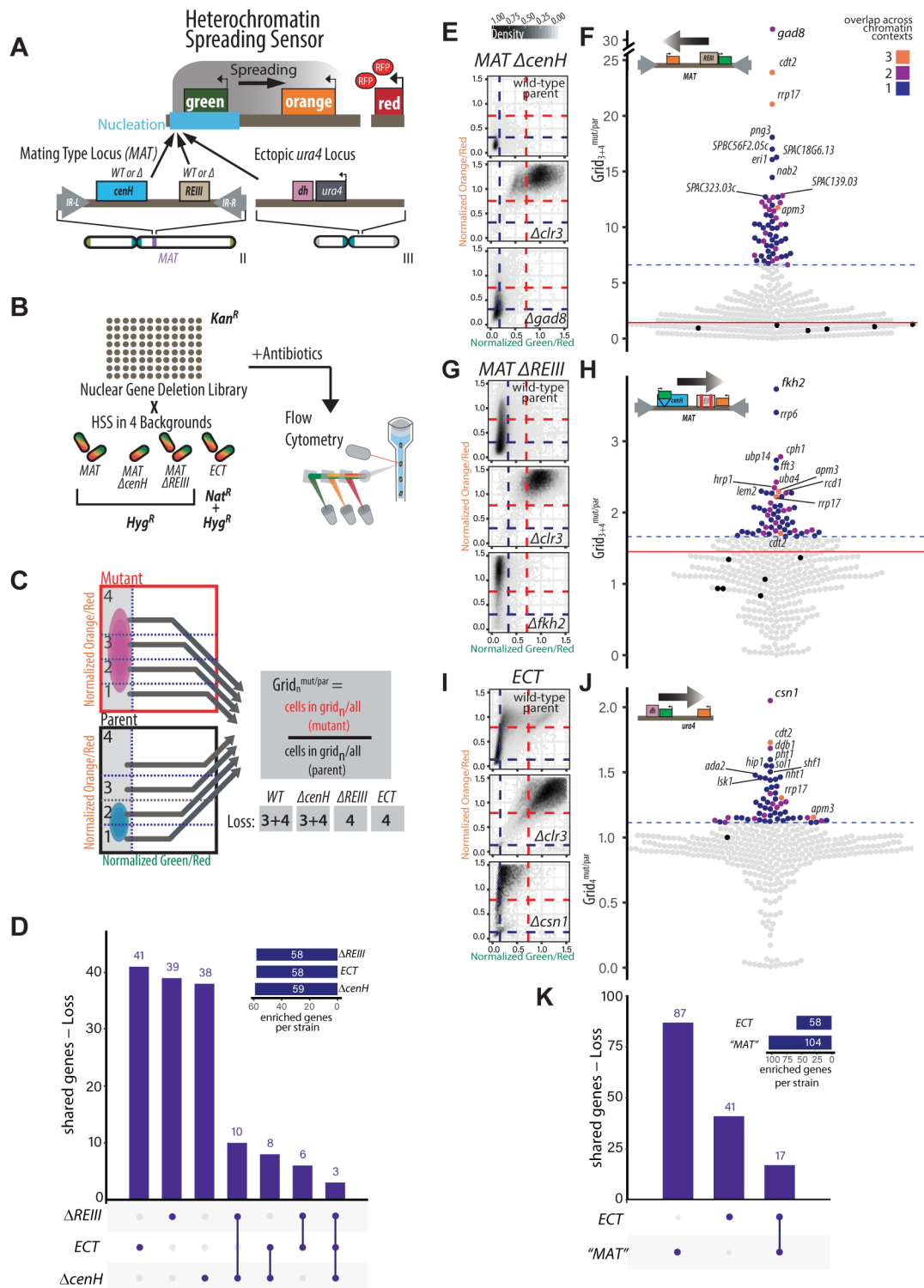


Fig 1.1. A genetic screen based on a suite of fluorescent reporters identifies regulators of heterochromatin nucleation-distal gene silencing in different chromatin contexts.

A. Top: Overview of heterochromatin spreading sensor (HSS,²⁴). Three transcriptionally encoded fluorescent protein genes are integrated into the genome. SFGFP (“green”) proximal or internal to the nucleation site allows identification of heterochromatin nucleation; mKO2 (Figure caption continued on the next page.)

(Figure caption continued from the previous page.)

“orange”) distal to the nucleation site allows identification of heterochromatin spreading.

3x2C (“red”) in a euchromatin region normalizes cell-to-cell noise. Bottom: The endogenous mating type locus (*MAT*) and heterochromatin ectopically targeted to the *ura4* locus²⁴ were examined with the HSS in the screen. In bona fide mutations of the *MAT* nucleators, *cenH* and *REIII*, nucleation is only initiated at one site. See **Fig S1.1** for detailed diagrams.

- B. Workflow of the screen to identify genes that contribute to nucleation-distal gene silencing. A custom nuclear function deletion library (S1 Table) was mated with four different reporter strains (*WT MAT*, *MAT ΔcenH*, *MAT ΔREIII* and *ECT*). The fluorescence of “green”, “orange” and “red” for each mutant cell within each background are recorded by flow cytometry.
- C. Overview of the loss-of-spreading analysis with mock distributions of cells and grids indicated. To identify cells that have successfully nucleated heterochromatin and are silencing-competent, “green”-off populations (successful nucleation events) are isolated first. Within these populations, enrichments of cell populations in particular “orange” fluorescence ranges (Grid_n) are calculated as $\text{Grid}_n^{\text{mut/par}}$. This second step specifically assesses for any loss of nucleation-distal gene silencing. As an example, In *WT MAT* $\text{Grid}_{3+4}^{\text{mut/par}}$ is calculated as percentage of the mutant population divided by percentage of parent population in Grid_{3+4} . The Grids (either 3+4 or 4) used for analysis of loss of spreading in the four chromatin contexts are indicated.
- D. Upset plots indicating the frequency of “loss of spreading” gene hits appearing in one or multiple singly nucleated chromatin contexts. For each bar, the chromatin context(s) with shared phenotypes for the underlying gene hits is indicated below the plot. The inset indicates the total number gene hits for loss of spreading in each chromatin context. “Shared genes”: number of genes that appear as “loss of spreading” hits across the number of indicated chromatin contexts.
- E. *MAT ΔcenH* 2D-density hexbin plots of the wild-type parent, a strong heterochromatin loss hit (*Δclr3*), and the top loss of nucleation-distal silencing hit (*Δgad8*) in this chromatin context. Dashed blue lines indicate the values for repressed fluorescence state and dashed red lines indicate values for fully expressed fluorescence state.
- F. Beeswarm plots of $\text{Grid}_{3+4}^{\text{mut/par}}$ for *MAT ΔcenH* loss of nucleation-distal silencing hits and number of overlapping contexts. The top 10 hits are all annotated, and below those hits, mutants that show overlap with at least 2 other chromatin contexts are additionally annotated. Red line, 2SD above the $\text{Grid}_{3+4}^{\text{mut/par}}$ of the wild-type parent isolates (black dots); dashed brown line, the 85th percentile; Dot color, number of chromatin contexts with loss of spreading phenotype over the cutoff. This mutation allows examination of only the *REIII* nucleation site at the *MAT* locus.
- G. -H. Beeswarm plots of $\text{Grid}_4^{\text{mut/par}}$ for the *MAT ΔREIII* strain were analyzed and displayed as in E. and F. This mutation allows examination of only the *cenH* nucleation site at the *MAT* locus.
- I. -J. Data for the *ECT* strain were analyzed and displayed as in G. and H. This strain examines a euchromatic context and analyzes silencing of at the *ura4* locus by spreading from an ectopic nucleation site.
- K. Upset plots indicating the frequency of “loss of spreading” gene hits appearing in singly nucleated *MAT* contexts (*MAT ΔREIII* and *MAT ΔcenH*) versus the *ECT* context.

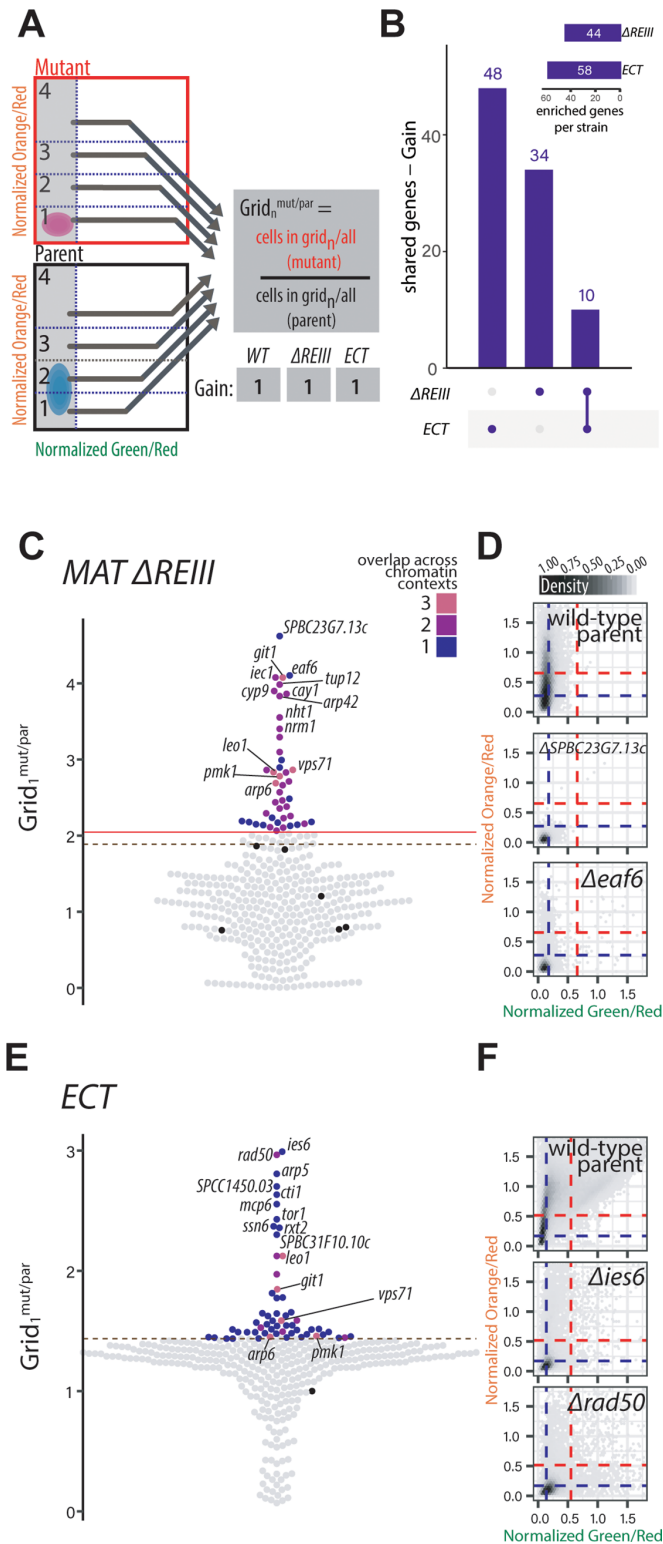


Fig 1.2. Gain of nucleation-distal gene silencing in *MAT ΔREIII* and *ECT* chromatin contexts.

A. Overview of the gain of nucleation-distal silencing analysis with mock distributions of cells and grids indicated, as in Fig 1.1C. To identify gain of spreading mutants in *ECT* and *MAT* (Figure caption continued on the next page.)

(Figure caption continued from the previous page.)

$\Delta REIII$, $Grid_1^{mut/par}$ was calculated as percentage of the mutant population divided by percentage of parent population in $Grid_1$.

- B. Upset plots indicating the frequency of Gain of Spreading gene hits that appear in one or both chromatin contexts as in **Fig 1.1D**. For each bar, the chromatin context(s) with shared phenotypes for the underlying gene hits is indicated below the plot. The inset indicates the total number gene hits in each chromatin context of the same phenotype.
- C. Beeswarm plots of $Grid_1^{mut/par}$ for *MAT* $\Delta REIII$ gain of nucleation-distal silencing hits. The top 10 hits are all annotated, and below those hits, mutants that show overlap with 2 other (*WT* *MAT* and *ECT*) chromatin contexts are additionally annotated. Red line, 2SD above the $Grid_1^{mut/par}$ of wild-type parent isolates (black dots); dashed brown line, the 85th percentile; Dot color, number of chromatin contexts with loss of spreading phenotype over the cutoff.
- D. *MAT* $\Delta REIII$ 2D-density hexbin plots of the wild-type parent, and the two top gain of spreading hit of this chromatin context. Dashed blue lines indicate the values for repressed fluorescence state and dashed red lines indicate values for fully expressed fluorescence state.
- E. -F. As in A. and B., but for *ECT*.

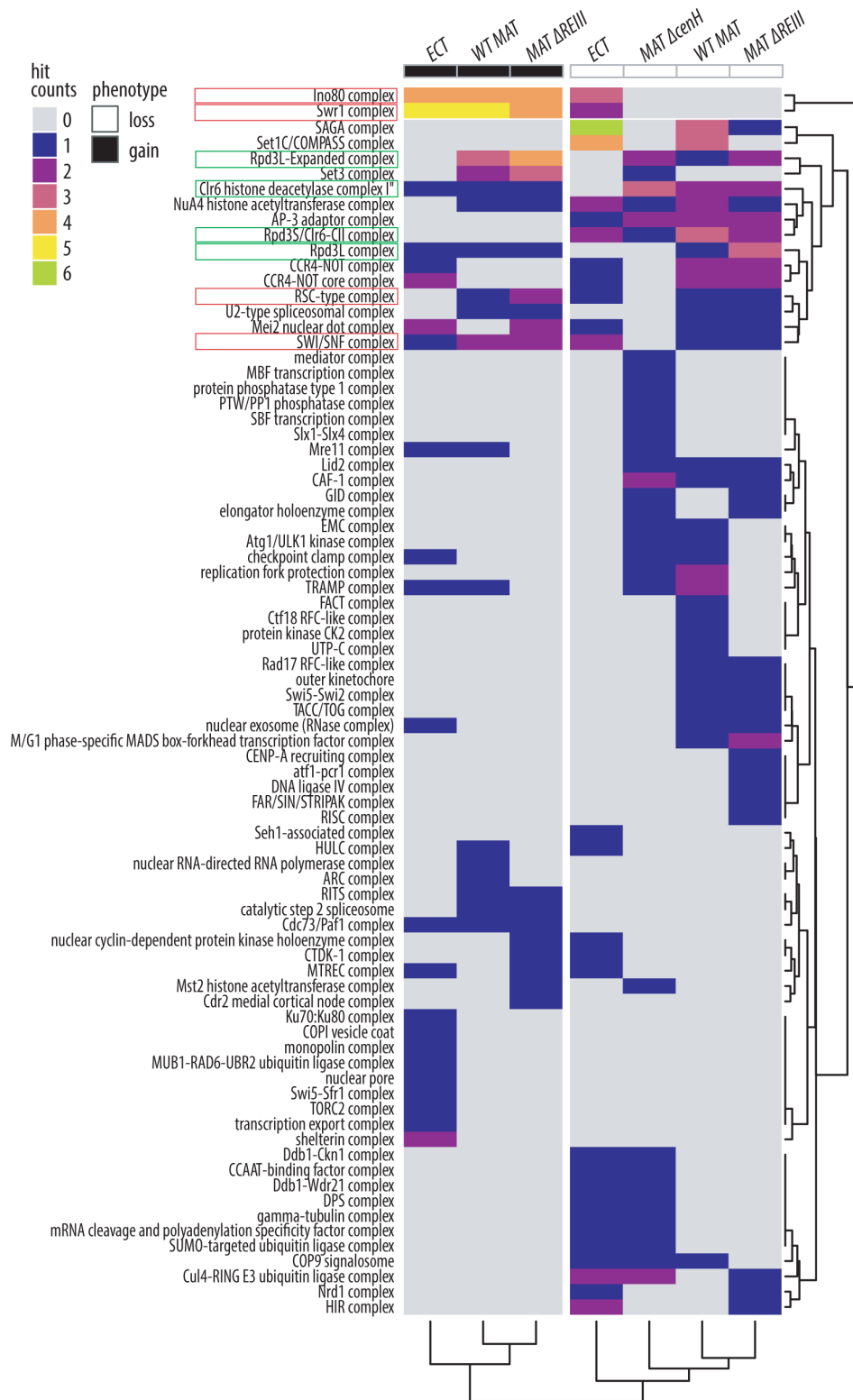


Fig 1.3. Heterochromatin nucleation-distal gene silencing is regulated by sets of unique and common protein complexes across different chromatin contexts.

Heatmap of GO complex annotations for hits in each category and strain. Rows, representing (Figure caption continued on the next page.)

(Figure caption continued from the previous page.)

GO complexes annotated to genes within the screen that were identified as hits, are arranged via hierarchical clustering. Columns are defined by the hit phenotype (loss of nucleation-distal silencing - white; gain of nucleation-distal silencing - black), and each screen chromatin context is indicated at the top. The columns were clustered by hierarchical clustering and the dendrogram was cut to define 2 branches. Red boxes, chromatin remodeling complexes; Green boxes, Clr6 complexes (Note that Rpd3L Expanded includes Set3C).

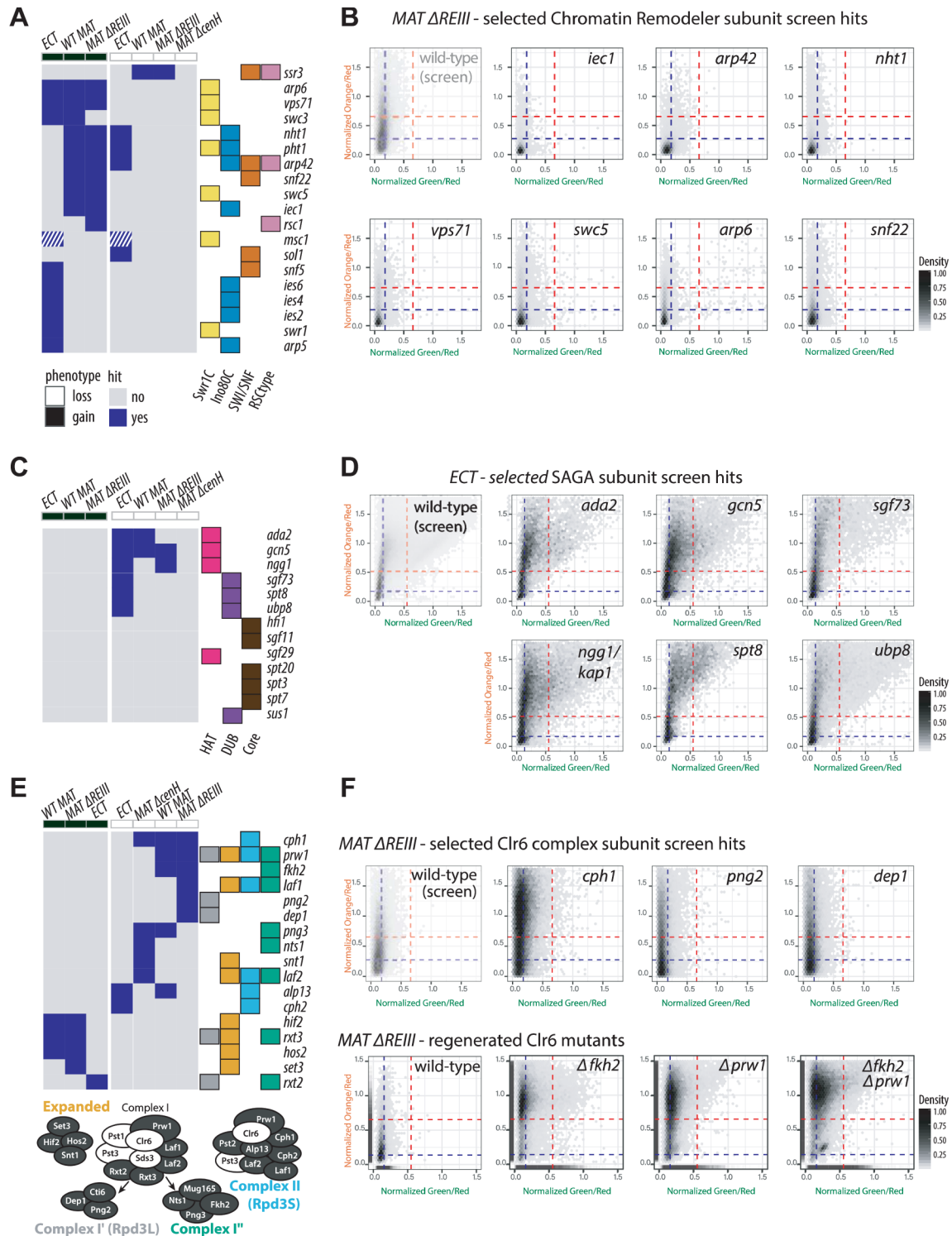


Fig 1.4. Chromatin remodeler, SAGA and Clr6 complexes regulate nucleation-distal silencing.

A. Table of complex members which were hits for chromatin remodeler complexes Swr1C, Ino80, SWI/SNF, and RSC. Components that showed a “gain” or “loss” of nucleation-distal silencing phenotype for each background were identified a hits and are marked blue, subunits that are a hit for both phenotypes (*msc1*) are white-blue crosshatched. The (Figure caption continued on the next page.)

(Figure caption continued from the previous page.)

proteins present in each complex or subcomplex are annotated at the right: color indicates membership of a particular remodeling complex, as labeled below.

- B. 2D density hexbin plots for selected chromatin remodeler gain of nucleation-distal silencing screen hits in *MAT ΔREIII*.
- C. As described in panel A. but for the SAGA complex. All SAGA subunits in the screen except TAFII are shown.
- D. 2D density hexbin plots for SAGA loss of nucleation-distal silencing screen hits in *ECT*.
- E. As described in panel A. Clr6 mutants that were not hits are *mug165*, *pst2* and *cti6*. Bottom: schematic of Clr6 complexes with essential subunits indicated in white.
- F. Top: 2D density hexbin plots for selected Clr6 complex loss of spreading screen hits in *MAT ΔREIII*. Bottom: *Δfkh2*, *Δprw1* and *Δfkh2 Δprw1* mutants were re-created *de novo* in *MAT ΔREIII*. A rug plot is included on the X and Y axes indicating the 1D density for each color. Rug lines are colored with partial transparency to assist with visualization of density changes. *MAT ΔREIII* and *ECT* parents shown in **Fig 1.1** are shown here again (with transparency) for comparison.

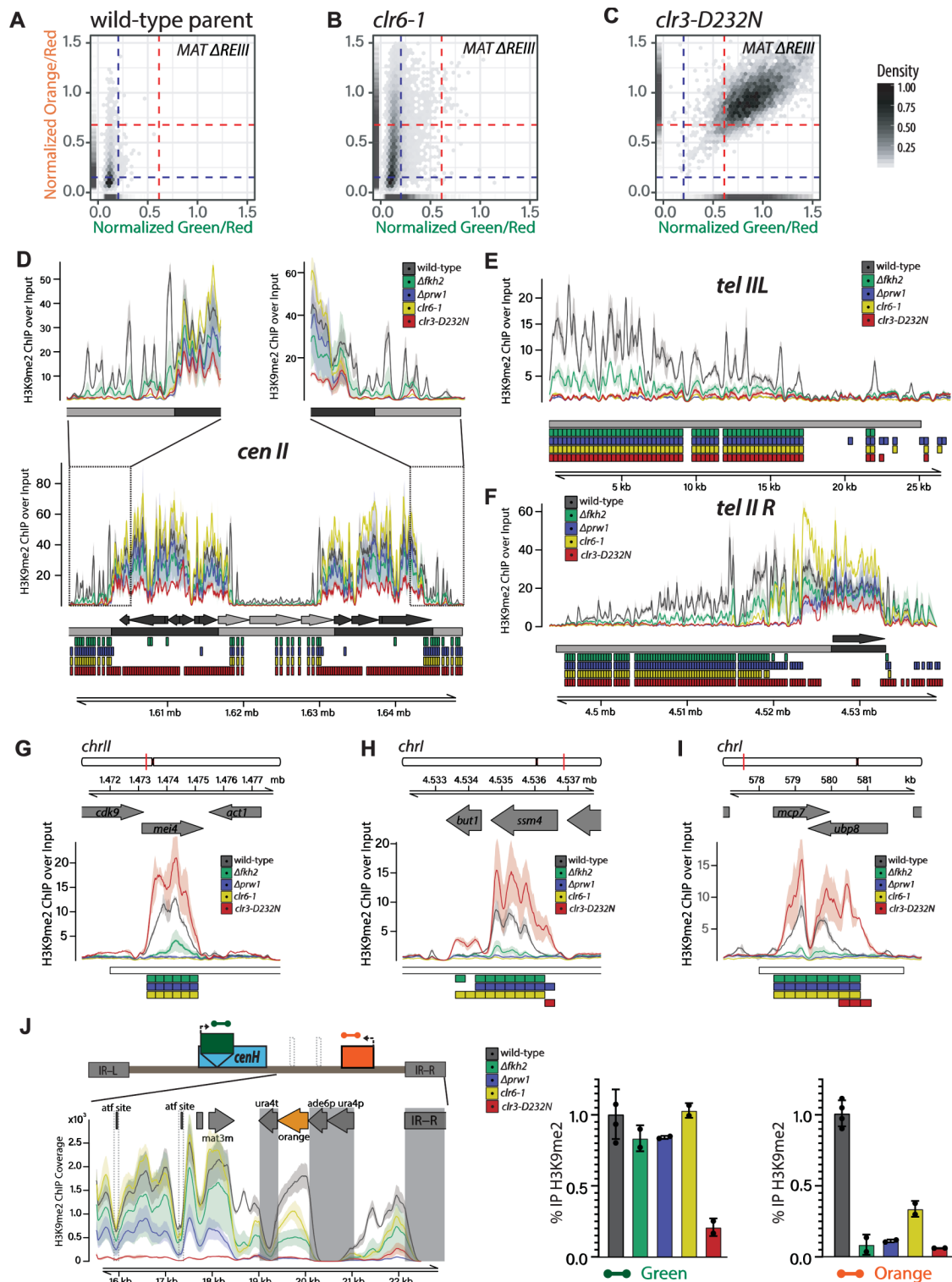


Fig 15. Fkh2- containing Clr6 Complexes regulate H3K9me2 spreading at constitutive and facultative heterochromatin loci.

A. -C. The hypomorphic *clr6-1* allele exhibits a loss of nucleation-distal silencing, while the catalytic dead *clr3-D232N* allele loses all silencing. 2D density hexbin and rug plots in the *MAT Δ REIII* background of the parent strain (A.) run together with B. & C.; *clr6-1* (B.); and (Figure caption continued on the next page.)

(Figure caption continued from the previous page.)

clr3-D232N (C.). A rug plot is included on the X and Y axes indicating the 1D density for each color. Rug lines are colored with partial transparency to assist with visualization of density changes. Dashed blue lines indicate the values for repressed fluorescence state and dashed red lines indicate values for fully expressed fluorescence state.

- D. -J. Visualization of H3K9me2 ChIP-seq signals in the *MAT ΔREIII* background at centromere II (D.), telomere and subtelomere *III* and *R* (E.&F.), three heterochromatin islands (G.-I.), and the right side of the *MAT* locus (J. Left). ChIP/Input normalized signal is plotted as mean (line) and 95% confidence interval (shade) for each genotype. For J. Left, alignment was performed to a custom mating type region contig in *MAT ΔREIII* with green and orange color cassettes. ChIP signal represents the coverage of each interval adjusted for the sequencing depth of the full genome bam file relative to that of the full genome bam file with the lowest depth. Features of interest are annotated above the signal tracks. During data processing for alignment to this custom contig, reads mapping to multiple locations within the reference sequence were removed. For this reason, there is little to no signal over regions that are homologous within this reference including *ura4p/ade6p* at the color cassette promoters, *ura4t* at the color cassette terminators, and *IR-L* and *IR-R* elements (these regions are shaded). Signals at feature “atf site” (indicated by dashed box) are reduced as both 7bp sites in *MAT ΔREIII* are deleted. D.-I. Below the signal tracks the following annotations are present in order from top to bottom: (1) D-F, features of interest (*i.e.* nucleators, dark grey; non-nucleator, light grey) based on coordinates and strand derived from Pombase (since no nucleator sequences are present on subtelomere *III*, first annotation row below the signal tracks is empty); G-I., previously identified euchromatin embedded H3K9me2 heterochromatin region (“island”, “HOOD”, or “region”) annotated as a white box. (2) for D-F only, nucleation and spreading annotation zones (based on (1)) are represented by dark grey and light grey boxes respectively. Spreading zones are defined to be between or outside of nucleation zones. (3–6, D-F) or (2–5, G-I): 300bp regions determined to be significantly differentially enriched for the comparisons between *Δfkh2* and wild-type (green), *Δprw1* and wild-type (blue), *clr6-1* and wild-type (yellow), *clr3-D232N* and wild-type (red) are annotated as colored boxes respectively. In J. Right, bars above signal tracks indicate wild-type normalized H3K9me2 ChIP-RTqPCR signals for indicated genotypes conducted independently of the ChIP-seq experiment at “green” and “orange” reporters. Error bars represent 1SD of three replicates.

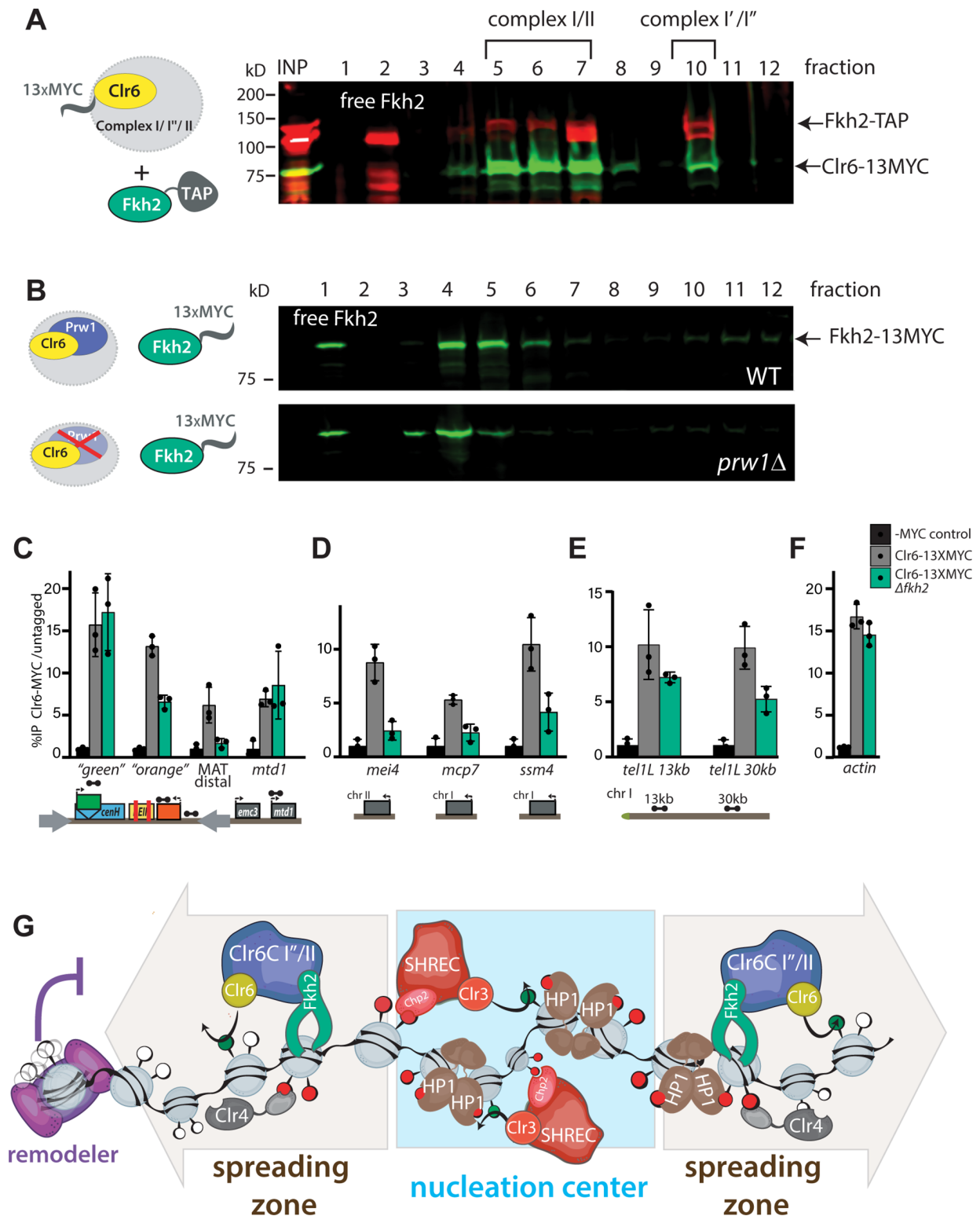


Fig 1.6. Fkh2 is a resident member of multiple Clr6 complexes and directs Clr6 to nucleation-distal heterochromatin regions.

A. Fkh2 comigrates with medium sized and large Clr6 complexes. Western blot against TAP (red) and MYC (green) on fractions of a sucrose density gradient of whole cells extract (Figure caption continued on the next page.)

(Figure caption continued from the previous page.)

containing Fkh2-TAP and Clr6-MYC. Fkh2 migrates as a free protein on top of the gradient and in both major peaks of Clr6. Complex annotation based on ⁴⁴.

- B. Fkh2 migration in sucrose gradients depends on Prw1. Western blot against MYC (green) on fractions of a sucrose density gradient of wild-type (WT) or $\Delta prw1$ whole cell extract containing Fkh2:MYC. While the free Fkh2 fraction is not affected by the absence of Prw1, the medium and large peak fractions shift towards the top of the gradient.
- C. -F. Clr6 chromatin localization in heterochromatin spreading areas and heterochromatin islands depends partially on Fkh2. Clr6:MYC ChIP qPCR in wild-type (Clr6- 13XMYC) or $\Delta fkh2$ (Clr6-13XMYC $\Delta fkh2$) background relative to an untagged (-MYC) control, in *MAT $\Delta REIII$* at the HSS reporter and downstream (C.), heterochromatin islands (D.), *tel1L* (E.), and *act1* (F.). Error bars indicate 1SD of three replicates.
- G. Model for control of heterochromatin spreading by Clr3, Clr6 and chromatin remodeler complexes. The Clr3- containing SHREC complex is essential for heterochromatin assembly at noncoding RNA-driven nucleation centers, such as *cenH*, *dg/dh* repeats or *tlh1/2*. There, SHREC activity enables normal HP1 and Clr4 H3K9 methylase activity. In the spreading zone, Fkh2-containing Clr6 complexes (complex I" or complex II) are required to propagate H3K9 methylation and gene silencing. Fkh2 recruits Clr6 to nucleation center-distal chromatin. Chromatin remodelers repel spreading via nucleosome destabilization, thus hinder the "guided-state" nucleosome-to-nucleosome spreading mechanism of Clr4.

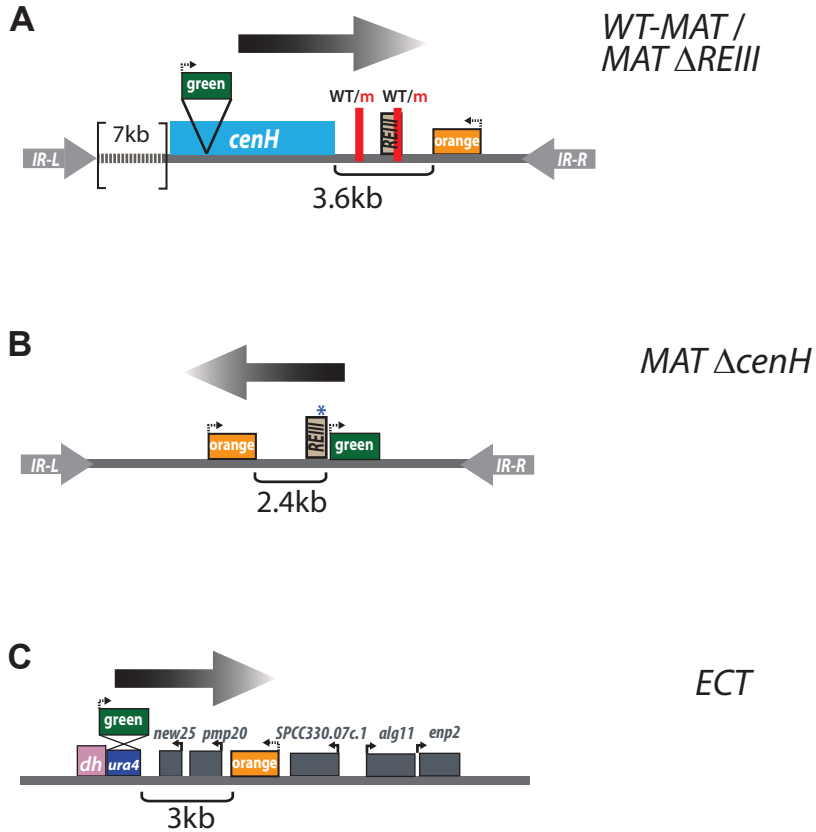


Fig S1.1. Screen of chromatin contexts with “green” and “orange” reporters.

To-scale diagrams of the heterochromatin spreading sensors (without the euchromatically placed “red” reporter) in the 4 chromatin contexts used for the spreading screen (as in Greenstein et al 2018). The direction in which spreading is analyzed (“green” to “orange”) is indicated per chromatin context.

- WT MAT* and *MAT ΔREIII*. These two contexts are similar, except that *MAT ΔREIII* contains two short 7bp deletions of the two Atf1/Pcr1 DNA binding sites near *REIII*, inactivating it. The first binding site is not included in *REIII*, per the definitions of ⁹⁸and ²³.
- MAT ΔcenH*.
- ECT*. In Greenstein et al 2018, the distance between “green” and “orange” was varied for B. and C. contexts, without changes to the qualitative behavior of spreading.

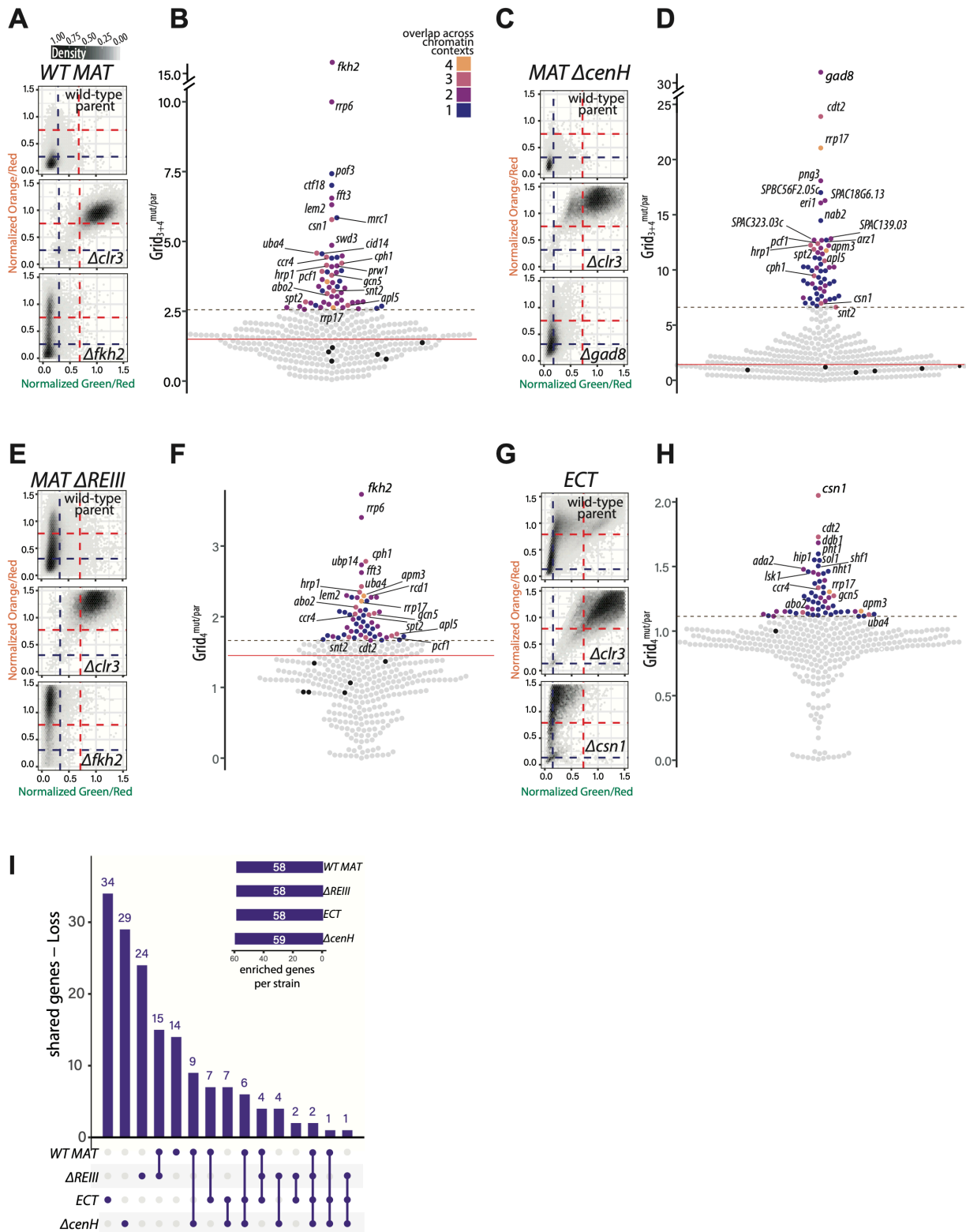


Fig S1.2. Regulators of heterochromatin nucleation-distal silencing in all four chromatin contexts.

A. WT-MAT 2D-density hexbin plots of the wild-type parent, a strong heterochromatin loss hit (Figure caption continued on the next page.)

(Figure caption continued from the previous page.)

($\Delta clr3$), and the top loss of spreading hit ($\Delta fkh2$) in this chromatin context. Dashed blue lines indicate the values for repressed fluorescence state and dashed red lines indicate values for fully expressed fluorescence state.

- B. Beeswarm plots of $Grid_{3+4}^{mut/par}$ for *WT MAT* loss of spreading hits. The top 10 hits are all annotated, and below those hits, mutants that show overlap with at least 3 other chromatin contexts are additionally annotated. Red line, 2SD above the $Grid_{3+4}^{mut/par}$ of the wild-type parent isolates (black dots); dashed brown line, the 85th percentile; Dot color, number of chromatin contexts with loss of spreading phenotype over the cutoff.
- C. -D. Data for the *WT $\Delta cenH$* strain were analyzed and displayed as in E. and F. This mutation allows examination of only the *REIII* nucleation site at the *MAT* locus.
- E. -F. Data for the *WT $\Delta REIII$* strain were analyzed and displayed as in E. and F expect that $Grid_4^{mut/par}$ was used as the metric.
- G. -H. Data for the *ECT* strain were analyzed and displayed as in E. and F.
- I. Upset plots indicating the frequency of “loss of spreading” gene hits appearing in one or multiple chromatin contexts. For each bar, the chromatin context(s) with shared phenotypes for the underlying gene hits is indicated below the plot. The inset indicates the total number gene hits for loss of spreading in each chromatin context. “Shared genes”: number of genes that appear as “loss of spreading” hits across the number of indicated chromatin contexts.

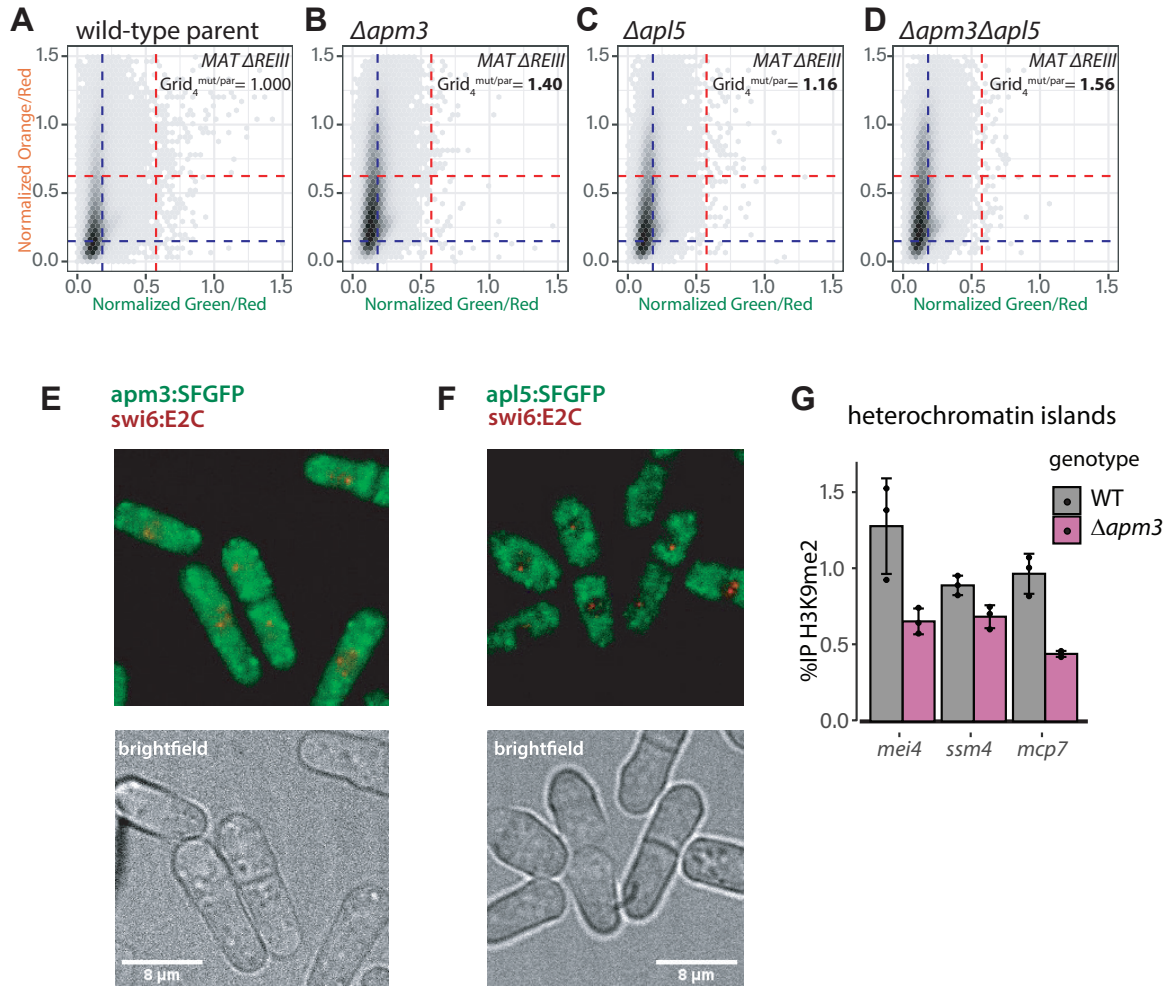


Fig S1.3. *apm3* and *apl5*, coding for nuclear-cytosolic and cytosolic proteins, respectively, act together in modulation of heterochromatin spreading.

- A. -D. 2D density hexbin plots of *de novo* generated Δapm3 (B.), Δapl5 (C.), and $\Delta\text{apm3}\Delta\text{apl5}$ double mutant (D.) compared to the wild-type *MAT ΔREIII* parent (A.). The Fold change of $\text{Grid}_4^{\text{mut/par}}$ is indicated in the plot. At least 3 independent isolates of each genotype are combined in each plot.
- E. *Apm3::SFGFP* is distributed in the cytosol and nucleus. *Apm3::SFGFP* was expressed from its native locus and co-expressed with *Swi6::E2C*. *Swi6::E2C* labels nuclear heterochromatin. Z-projection overlays of the *Apm3::SFGFP* and *Swi6::E2C* on top, and a brightfield image on the bottom.
- F. *Apl5::SFGFP* is largely nuclear excluded. *Apl5::SFGFP* was expressed from its native locus and co-expressed with *Swi6::E2C*. *Swi6::E2C* labels nuclear heterochromatin. Z-projection overlays of the *Apl5::SFGFP* and *Swi6::E2C* on top, and a brightfield image on the bottom.
- G. Δapm3 exhibits a mild defect in H3K9me2 accumulation at heterochromatin islands. H3K9me2 ChIP-qPCR in wild-type parent *MAT ΔREIII* or Δapm3 mutant. Error bars represent 1SD of three replicates.

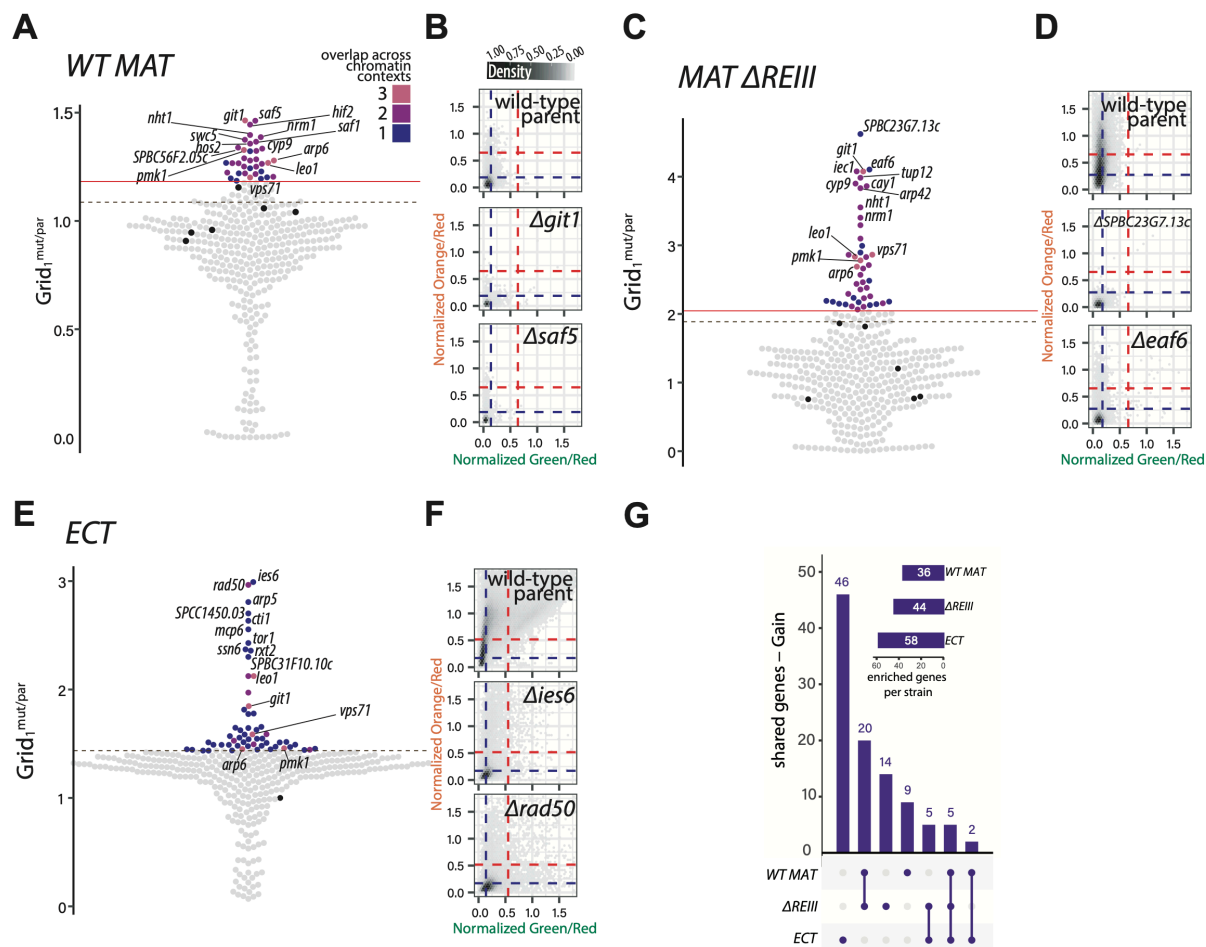


Fig S1.4. Gain of nucleation-distal gene silencing mutants in *WT MAT*, *MAT ΔREIII* and *ECT* chromatin contexts.

- A. Beeswarm plots of $Grid_1^{mut/par}$ for *WT MAT* gain of nucleation-distal silencing hits. The top 10 hits are all annotated, and below those hits, mutants that show overlap with 2 other chromatin contexts are additionally annotated. Red line, 2SD above the $Grid_1^{mut/par}$ of wild-type parent isolates (black dots); dashed brown line, the 85th percentile; Dot color, number of chromatin contexts with loss of spreading phenotype over the cutoff.
- B. *WT MAT* 2D-density hexbin plots of the wild-type parent, and the two top gain of nucleation-distal silencing hits of this chromatin context. Dashed blue lines indicate the values for repressed fluorescence state and dashed red lines indicate values for fully expressed fluorescence state.
- C. -D. As in A., B. but for *MAT ΔREIII*.
- E. -F. As in A., B. but for *ECT*.
- G. Upset plots indicating the frequency of gain of nucleation-distal silencing gene hits that appear in the chromatin the three in contexts as in **Fig 1.2B**. For each bar, the chromatin context(s) with shared phenotypes for the underlying gene hits is indicated below the plot. The inset indicates the total number gene hits in each chromatin context of the same phenotype.

Gain of distal silencing mutants:

Loss of distal silencing mutants:

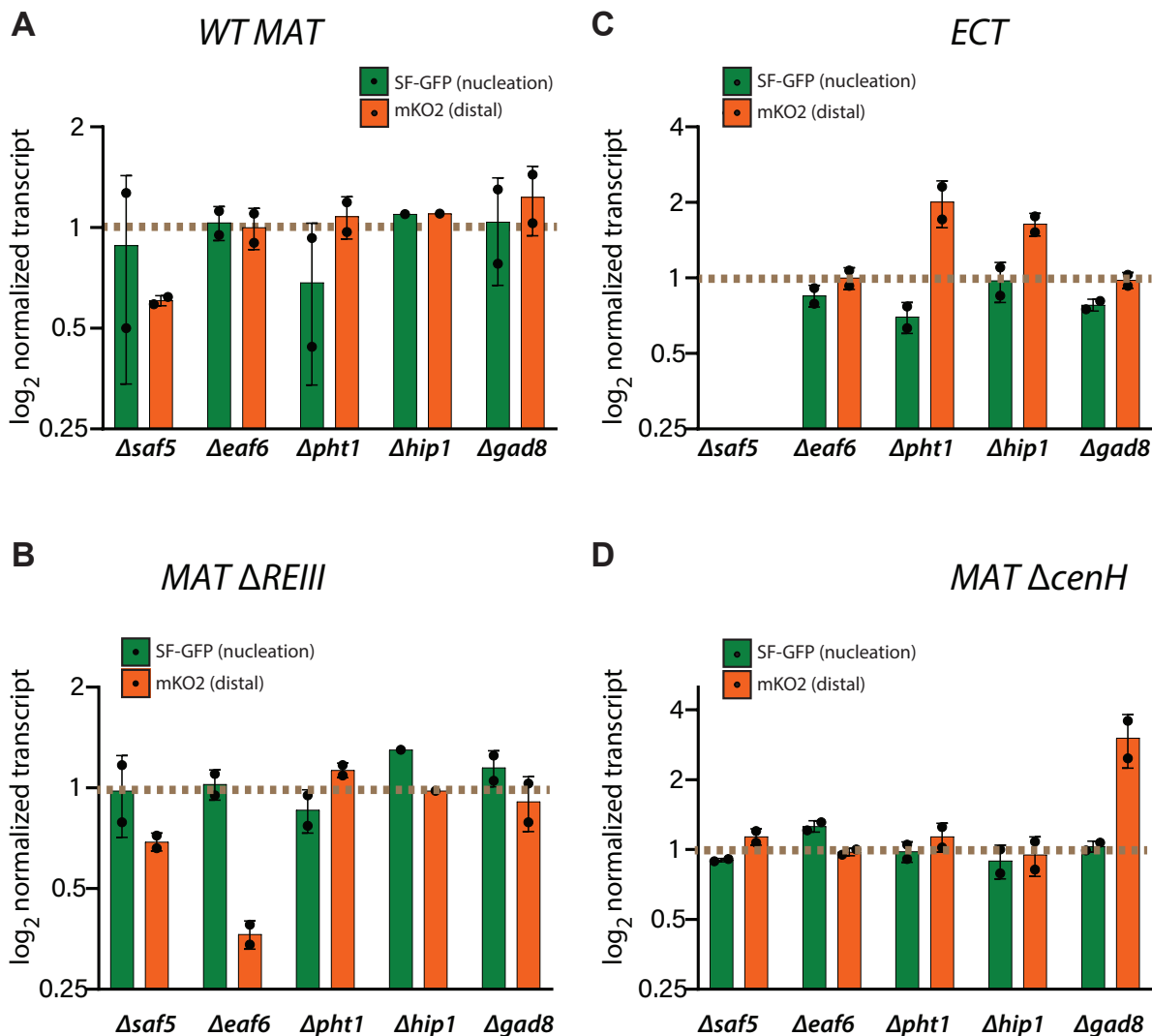


Fig S1.5. RT-qPCR validations of selected chromatin-context unique loss and gain of nucleation-distal silencing hits.

5 moderate- to strong hits in the loss and gain of distal silencing category that are partially or fully chromatin context-specific were selected for validations: *saf5* (gain of silencing in *WT MAT*, and moderately in *MAT $\Delta REIII$*), *eaf6* (gain of silencing only in *MAT $\Delta REIII$*), *pht1* and *hip1* (loss of silencing only in *ECT*), and *gad8* (strong loss of silencing in *MAT $\Delta cenH$* and mildly in *ECT*). RT-qPCRs for SF-GFP (“green”-nucleation) and mKO2 (“orange”, distal) transcripts normalized to the *act1* transcript and scaled to the wild-type (dashed brown line, = 1) are shown for examples of: Gain of distal silencing;

A. *WT-MAT*,

B. *MAT $\Delta REIII$* . Loss of distal silencing;

C. *ECT*,

D. *MAT $\Delta cenH$* . Error bars indicate 1SD of 2 biological replicates generated independently from the screen. Dotted lines represent wild-type control. Note we could not recover $\Delta saf5$ mutants in *ECT*.

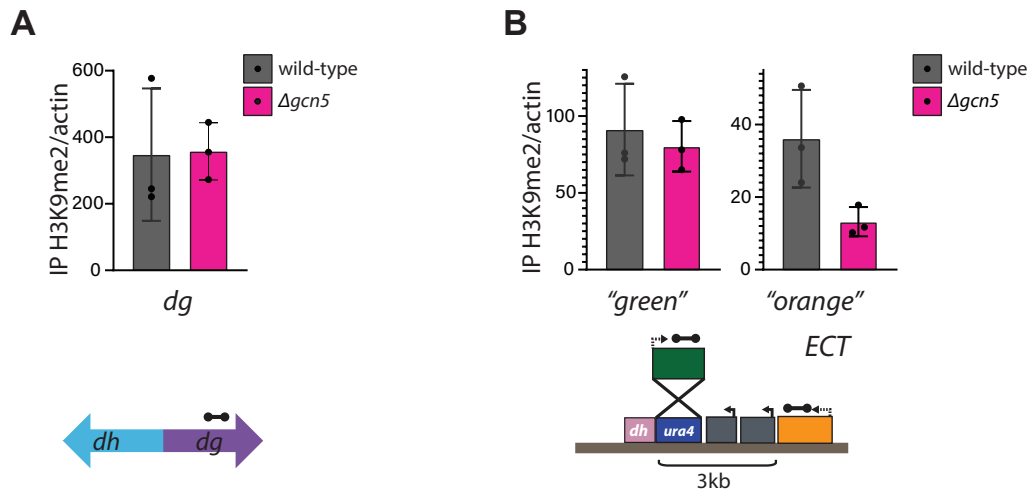


Fig S1.6. *gcn5* is specifically required for H3K9me2 spreading at the *ECT* heterochromatin spreading sensor, but not pericentromeric heterochromatin.

act1-normalized ChIP-qPCR for H3K9me2 in *ECT* wild-type parent or the *de novo* generated $\Delta gcn5$ mutant at

A. the pericentromeric *dg* element, and

B. the heterochromatin spreading sensor at the *ura4* locus in *ECT*. Dumbbells indicate qPCR amplicons. Error bars indicate 1SD of 3 biological replicates.

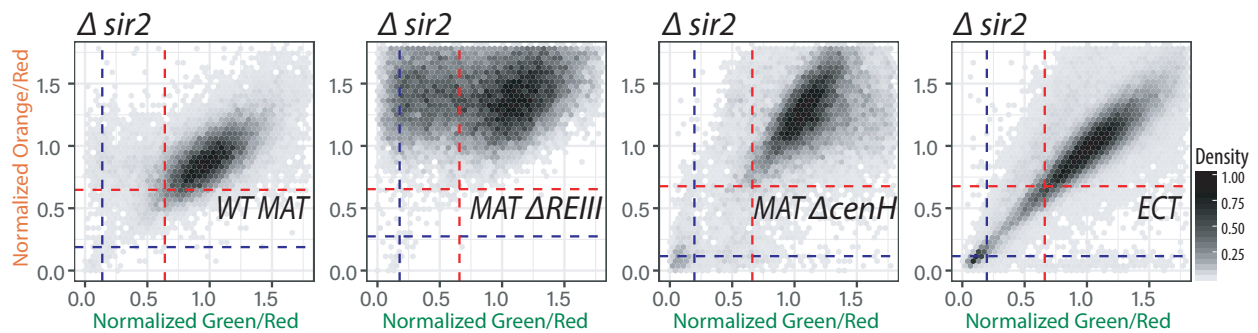


Fig S1.7. Class III HDAC family *Sir2* is required for heterochromatin silencing.

2D density hexbin plots of $\Delta sir2$ mutants in each chromatin context from the screen. Mutation in *sir2* causes a loss of silencing phenotype in all examined chromatin context.

MAT Δ REIII - Clr6 Subcomplex Components

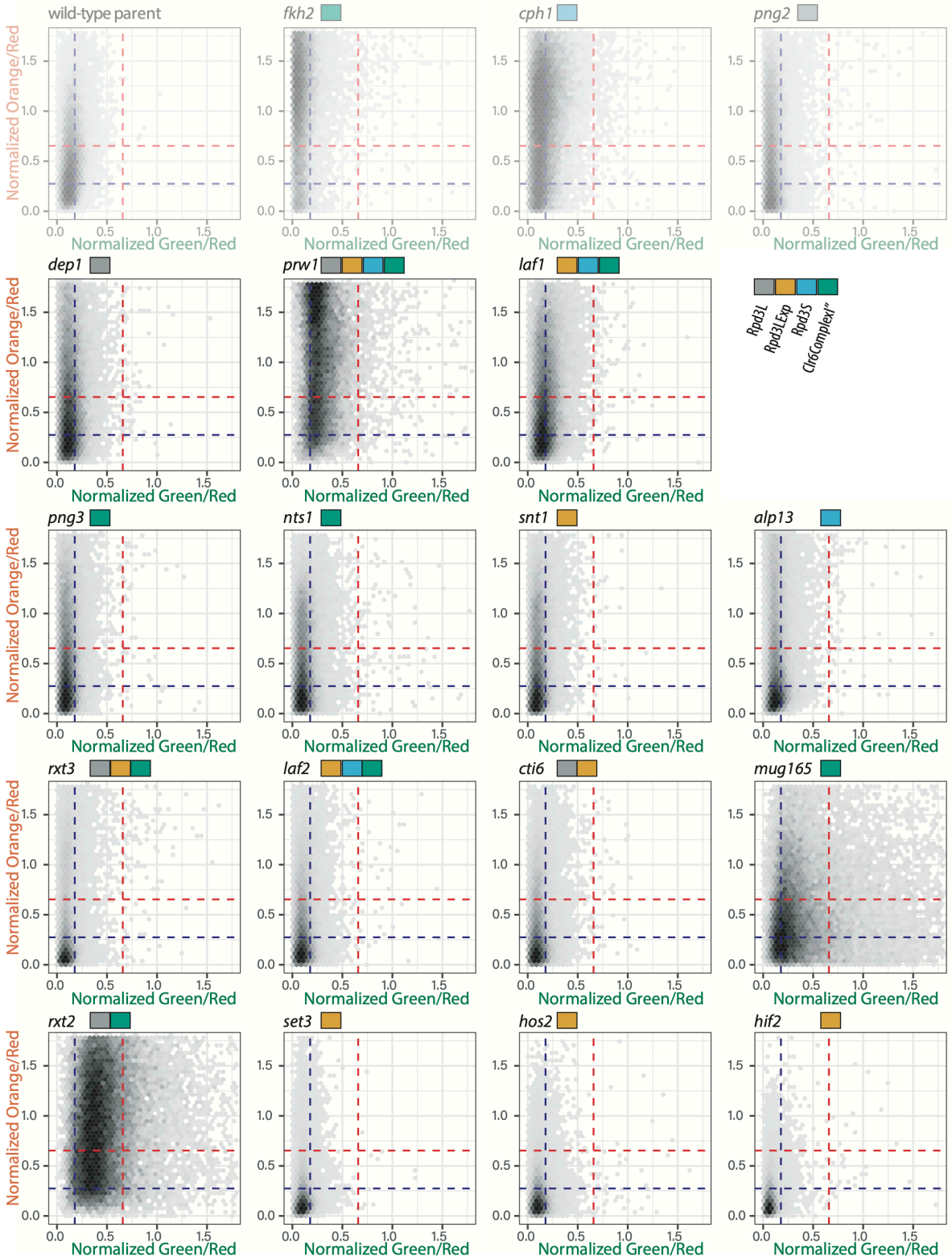


Fig S1.8. 2D density hexbin plots for all Clr6 complex subunit screen mutants in *MAT ΔREIII*.

2D density hexbin plots of all Clr6 complexes gene mutants from the screen, corresponding to **Fig 1.4E** in *MAT ΔREIII* context. The mutants are arranged in descending order of $\text{Grid}_{3+4}^{\text{mut/par}}$; in *MAT ΔREIII* only $\Delta fkh2$, $\Delta cph1$, $\Delta png2$, $\Delta dep1$, $\Delta prw1$ and $\Delta laf1$ were identified as loss of spreading phenotype. Original *MAT ΔREIII* wild type parent and mutants shown in **Figs 1.1** and **1.4E** are shown here again (with transparency) for comparison. GO complex annotations are indicated next to each mutant by colored boxes.

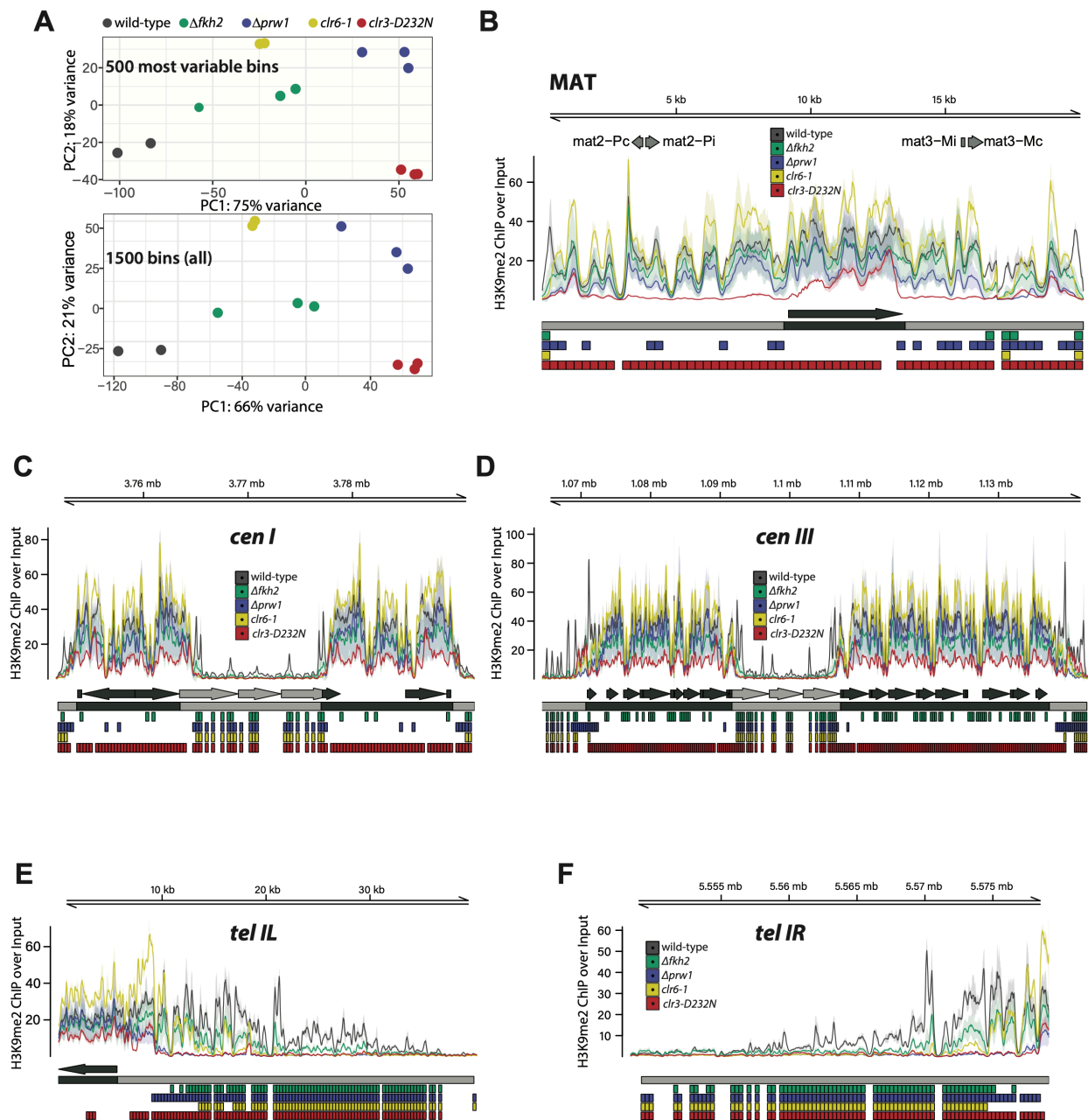


Fig S1.9. Fkh2- containing Clr6 complexes direct H3K9me2 spreading at multiple genomic regions.

- A. Principal Component Analysis was performed on the normalized counts in the top 500 most variable bins (analogous to RNA-Seq analysis, Top) or all 1500bp bins (Bottom) passing a threshold for global enrichment of H3K9me2 signal (see Methods). The first two principal component values are plotted for each sample with genotypes as defined in the legend.
- B. -F. Signal tracks plots for the MAT locus and indicated centromeres and telomeres as in the main text. No nucleator sequences are present on subtelomere IR so the first annotation row below the signal tracks is empty.

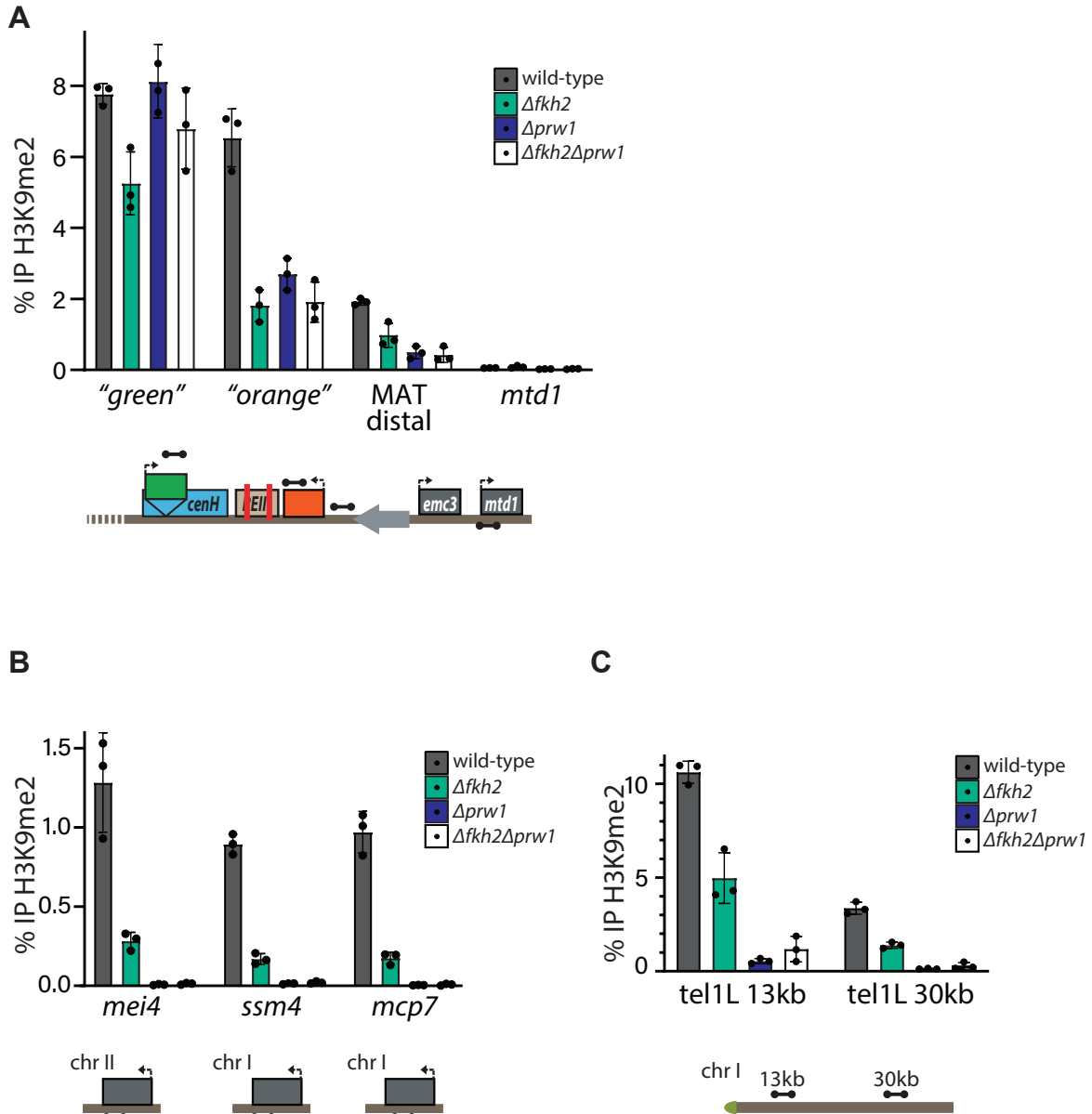


Fig S1.10. Fkh2 and Prw1 act together in spreading H3K9me2.

A. H3K9me2 ChIP-qPCR at the MAT locus in wild-type *MAT* $\Delta REIII$, $\Delta fkh2$, $\Delta prw1$, and the $\Delta fkh2\Delta prw1$ double mutant.

B. As in A., at indicated heterochromatin islands.

C. As in A., at *tel IL*. Error bars represent 1SD of 3 biological replicates.

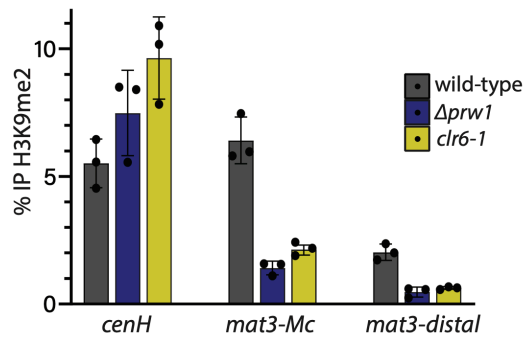
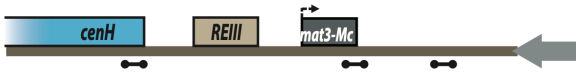


Fig S1.11. Effect of *clr6-1* and $\Delta prw1$ on H3K9me2 at a WT MAT locus without reporters
 H3K9me2 CHIP-qPCR at the MAT locus in a wild-type MAT locus (no heterochromatin spreading reporters, see diagram), $\Delta prw1$, and *clr6-1*, at indicated amplicons (dumbbells). Error bars represent 1SD of 3 biological replicates.

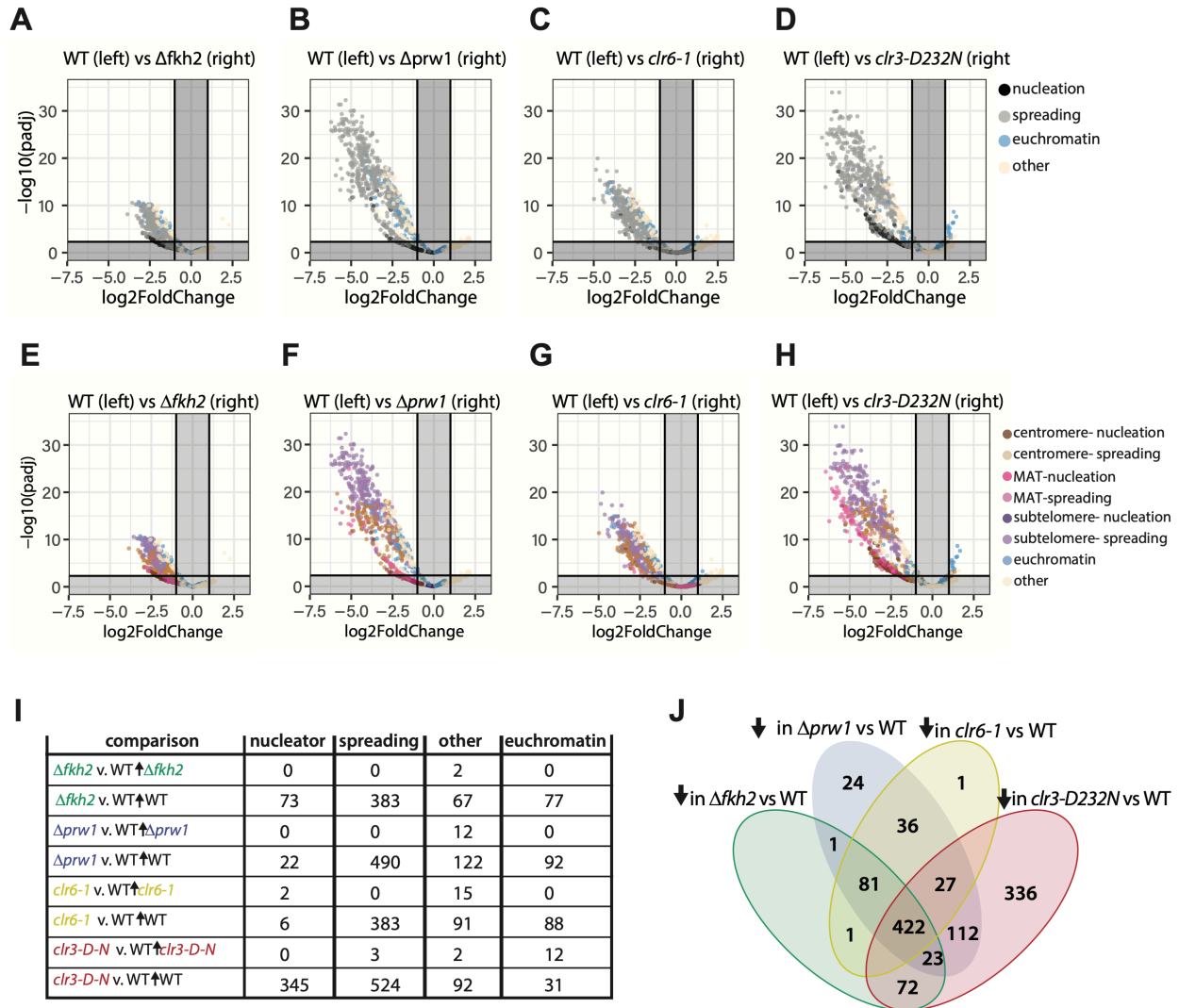


Fig S1.12. Fkh2- containing Clr6 complexes contribute primarily to H3K9me2 spreading, while Clr3 is required for H3K9me2 accumulation at all heterochromatin regions except islands.

- A. -D. Volcano plots representing $-\log_{10}(\text{adjusted p-value})$ vs $\log_2\text{FoldChange}$ values for mutants (I., $\Delta fkh2$; J., $\Delta prw1$; K., $clr6-1$; L., $clr3-D232N$) over WT. P-values were corrected for multiple testing with the Benjamini-Hochberg procedure. Cutoff values for adjusted p-value < 0.005 and absolute value $\log_2\text{FoldChange} > 1$ are annotated on the plot. Dots represent individual 300bp windows tested for differential enrichment. Dots are colored by their annotation to nucleation or spreading zones, presence within a previously identified euchromatin embedded H3K9me2 heterochromatin region (“island”, “HOOD”, or “region”), or regions outside these categories (other).
- B. -H. Volcano plots were generated as in A-D. Dots are colored by their annotation to nucleation or spreading zones broken down by heterochromatin location (pericentromere, subtelomere, MAT) or presence within a previously identified euchromatin embedded H3K9me2 heterochromatin region.
- H. The number of regions called as significant in each direction for each of the pairwise comparisons is tabulated per each category of genomic feature.
- I. The overlap of regions identified as significantly reduced in H3K9me2 signal in each mutant vs WT is compared in a Venn Diagram.

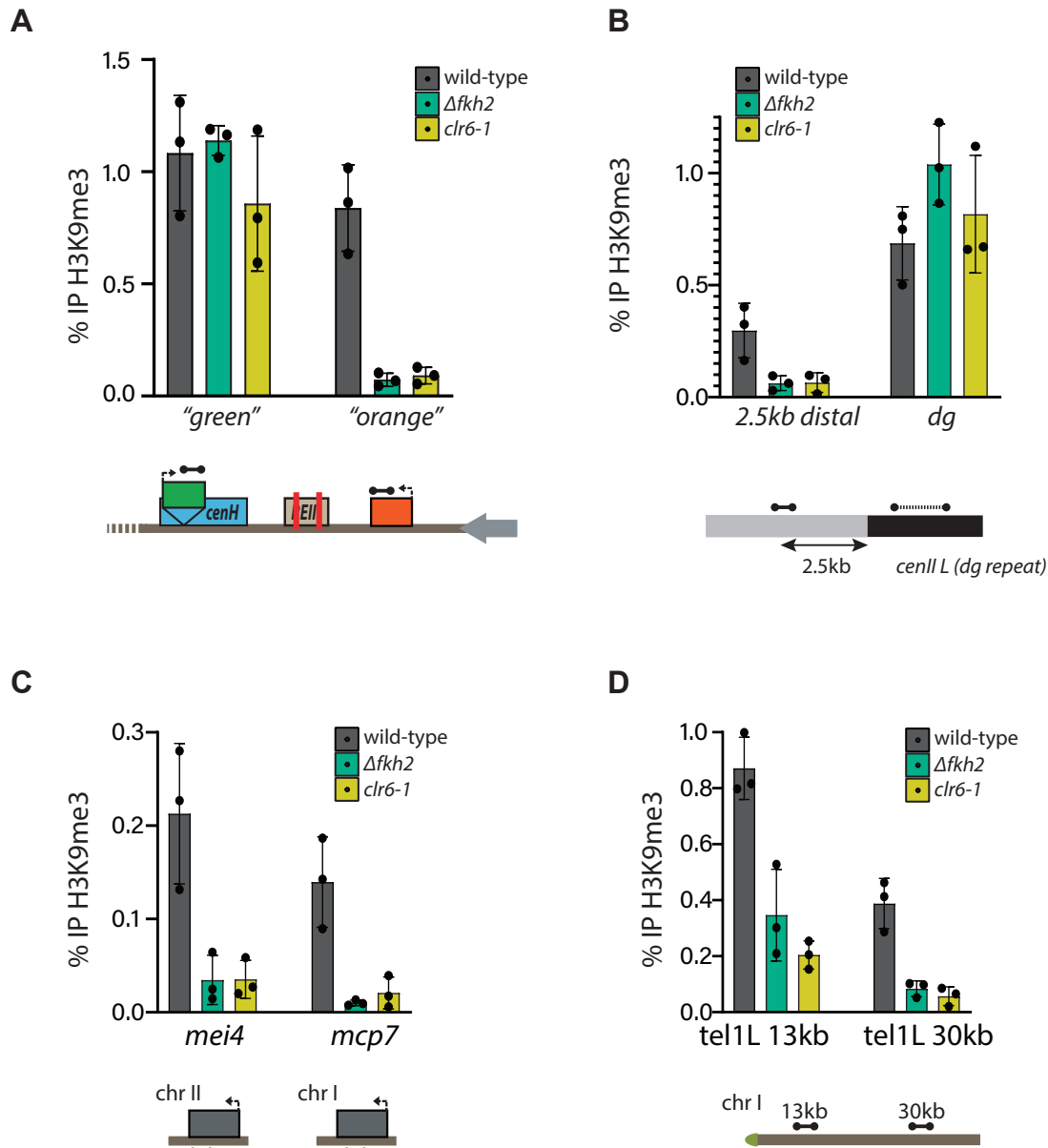


Fig S1.13. Clr6 affects spreading of H3K9me3.

- A. H3K9me3 ChIP-qPCR at the MAT locus in wild-type *MAT* $\Delta REIII$, $\Delta fkh2$, and *clr6-1*.
 B. As in A., at *dg* repeats, which are at the distal end of the left of the pericentromere at *cen II* and an amplicon 2.5kb beyond the last annotated nucleating feature at *cen II* left.
 C. As in A., but at heterochromatin islands *mei4* and *mcp7*.
 D. As in A., but at *tel 1L*. Error bars represent 1SD of 3 biological replicates.

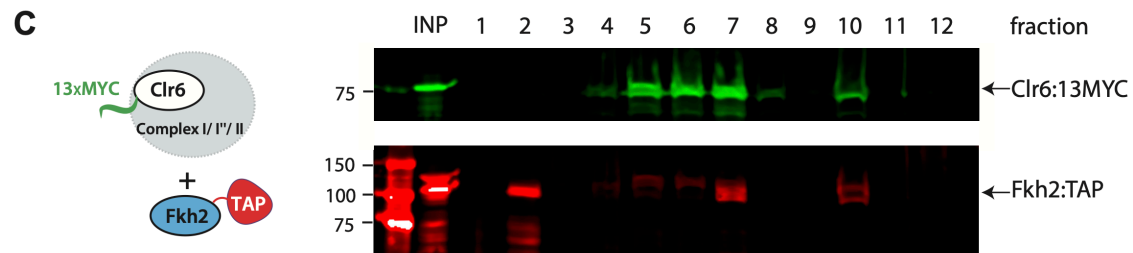
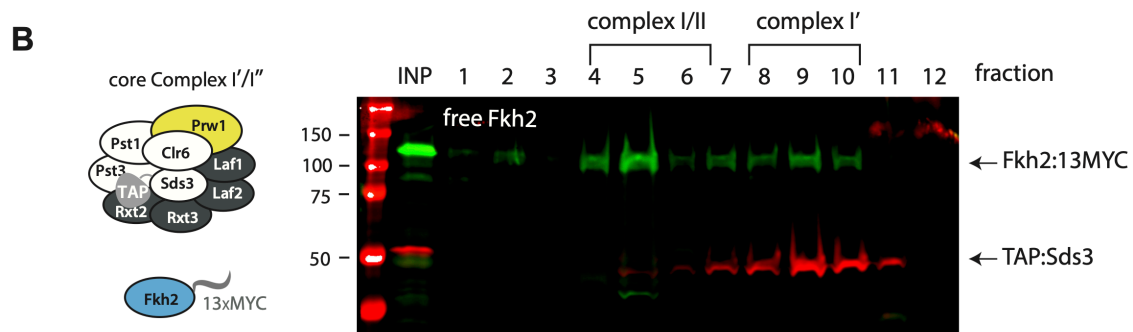
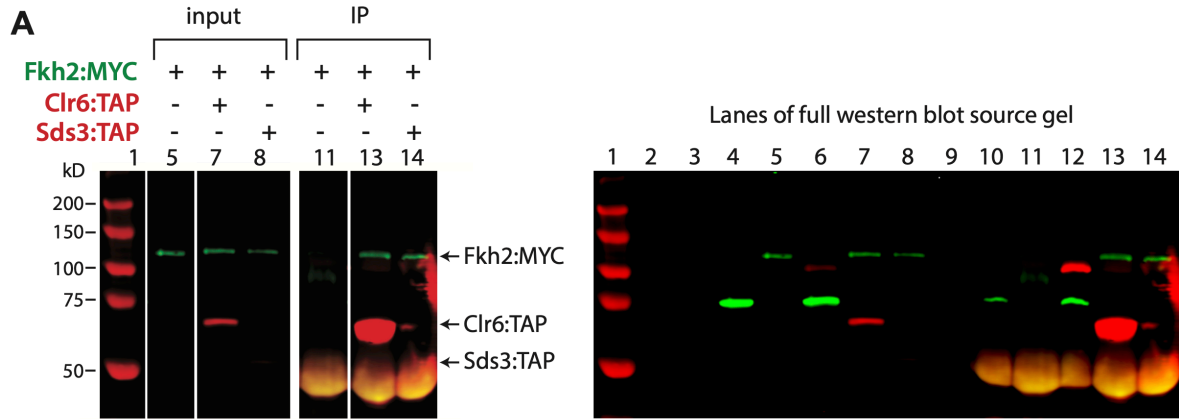


Fig S1.14. Fkh2 is a constituent member of Clr6 complexes.

A. Co-Immunoprecipitation experiment with baits Clr6-TAP or Sds3-TAP and prey Fkh2-MYC. Left: Western blot against indicated proteins for the Co-IP experiment. Right shows the entire western blot, including lanes unrelated to the co-IP experiment (2–4,5,10,12).

B. Sucrose density gradient for whole cell extracts of cells containing Sds3-TAP, a signature of complex I'/I'', and Fkh2:MYC. Gradient and Western as in Fig 1.6.

C. Single channel Western blots of Fig 1.6A.

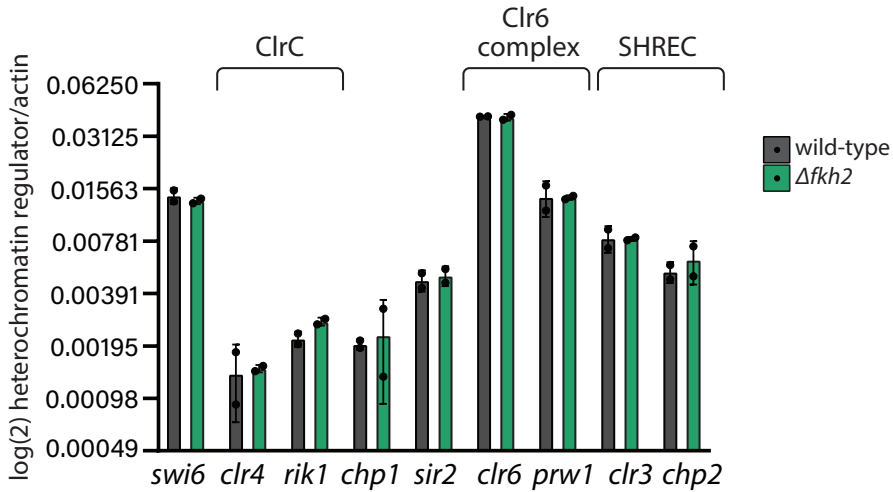


Fig S1.15. Fkh2 does not affect transcription of core heterochromatin regulators. RT-qPCR of indicated core heterochromatin regulators, including representatives of ClrC, Clr6, and SHREC in *MAT ΔREIII* wild-type or $\Delta fkh2$ cells. Heterochromatin regulator transcripts are normalized to the *act1* transcript and shown on a log₂ scale, given the wide distribution of transcript abundance between indicated regulators. Error bars indicate 1SD of 2 biological replicates.

Table S1.1. Nuclear function gene deletion library.

List of gene deletion strains used for genetic screens in this study.

Nuclear function gene deletion library.

	Systematic ID	Symbol	Description
1	SPAC1002.05c	jmj2	histone demethylase Jmj2
2	SPAC1006.03c	red1	RNA elimination defective protein Red1
3	SPAC1039.05c	klf1	transcription factor, zf-fungal binuclear cluster type Klf1
4	SPAC1071.02	mms19	CIA machinery protein Mms19
5	SPAC1071.06	arp9	SWI/SNF and RSC complex subunit Arp9
6	SPAC10F6.08c	nht1	Ino80 complex HMG box subunit Nht1
7	SPAC10F6.11c	atg17	autophagy associated protein kinase activator Atg17
8	SPAC1142.03c	swi2	Swi5 complex subunit Swi2
9	SPAC1142.08	fhl1	forkhead transcription factor Fhl1
10	SPAC11D3.07c	toe4	transcription factor, zf-fungal binuclear cluster type(predicted)
11	SPAC11D3.16c		Schizosaccharomyces specific protein
12	SPAC11E3.01c	swr1	SNF2 family ATP-dependent DNA helicase Swr1
13	SPAC11H11.01	sst6	ESCRT I complex subunit Vps23
14	SPAC11H11.05c	fta6	Mis6-Sim4 complex Fta6
15	SPAC12B10.10	nod1	medial cortical node Gef2-related protein protein Nod1
16	SPAC12G12.13c	cid14	TRAMP complex poly(A) polymerase subunit Cid14
17	SPAC139.03	toe2	transcription factor, zf-fungal binuclear cluster type (predicted)
18	SPAC139.06	hat1	histone acetyltransferase Hat1
19	SPAC1399.05c	toe1	transcription factor, zf-fungal binuclear cluster type
20	SPAC13A11.04c	ubp8	SAGA complex ubiquitin C-terminal hydrolase Ubp8
21	SPAC13D6.02c	byr3	translational activator, zf-CCHC type zinc finger protein (predicted)
22	SPAC13G6.01c	rad8	ubiquitin-protein ligase E3/ ATP-dependent DNA helicase Rad8
23	SPAC144.02	iec1	Ino80 complex subunit Iec1
24	SPAC144.05		DNA-dependent ATPase/ ubiquitin-protein ligase E3 (predicted)
25	SPAC144.06	apl5	AP-3 adaptor complex subunit Apl5 (predicted)
26	SPAC144.14	klp8	kinesin-like protein Klp8
27	SPAC14C4.06c	nab2	poly(A) binding protein Nab2 (predicted)
28	SPAC14C4.12c	laf1	Clr6 L associated factor 1 Laf1
29	SPAC14C4.13	rad17	RFC related checkpoint protein Rad17
30	SPAC1556.01c	rad50	DNA repair protein Rad50
31	SPAC15A10.11	ubr11	UBR ubiquitin-protein ligase E3 Ubr11
32	SPAC15A10.15	sgo2	inner centromere protein, shugoshin Sgo2
33	SPAC1610.01	saf5	splicing factor Saf5

	Systematic ID	Symbol	Description
34	SPAC1610.02c	mrpl1	mitochondrial ribosomal protein subunit L1 (predicted)
35	SPAC1687.05	pli1	SUMO E3 ligase Pli1
36	SPAC1687.09	irs4	autophagy/CVT pathway ENTH/VHS domain protein Irs4 (predicted)
37	SPAC16A10.03c		ubiquitin-protein ligase E3 involved in vesicle docking Pep5/Vps11-like (predicted)
38	SPAC16A10.07c	taz1	shelterin complex subunit Taz1
39	SPAC16C9.04c	mot2	CCR4-Not complex ubiquitin-protein ligase E3 subunit Mot2
40	SPAC16C9.05	cph1	Clr6 histone deacetylase associated PHD protein-1 Cph1
41	SPAC16E8.12c	png3	ING family homolog Png3 (predicted)
42	SPAC1751.01c	gti1	gluconate transmembrane transporter inducer Gti1
43	SPAC1782.05	ypa2	protein phosphatase type 2A regulator, PTPA family Ypa2
44	SPAC1782.08c	rex3	exonuclease Rex3 (predicted)
45	SPAC1782.09c	clp1	Cdc14-related protein phosphatase Clp1/Flp1
46	SPAC1783.05	hrp1	ATP-dependent DNA helicase Hrp1
47	SPAC17A2.12	rrp1	ATP-dependent DNA helicase/ ubiquitin-protein ligase E3 (predicted)
48	SPAC17G8.05	med20	mediator complex subunit Med20
49	SPAC17G8.07	yaf9	YEATS family histone acetyltransferase subunit Yaf9
50	SPAC17G8.09	shg1	Set1C complex subunit Shg1
51	SPAC17G8.10c	dma1	mitotic spindle checkpoint ubiquitin ligase Dma1
52	SPAC17G8.13c	mst2	histone acetyltransferase Mst2
53	SPAC17H9.10c	ddb1	Cul4-RING E3 adaptor Ddb1
54	SPAC17H9.19c	cdt2	WD repeat protein Cdt2
55	SPAC1805.14		Schizosaccharomyces specific protein
56	SPAC1805.15c	pub2	HECT-type ubiquitin-protein ligase E3 Pub2
57	SPAC1851.03	ckb1	CK2 family regulatory subunit Ckb1
58	SPAC18G6.02c	chp1	heterochromatin (HP1) family chromodomain protein Chp1
59	SPAC18G6.10	lem2	LEM domain nuclear inner membrane protein Heh1/Lem2
60	SPAC18G6.13		Schizosaccharomyces specific protein
61	SPAC1952.05	gcn5	SAGA complex histone acetyltransferase catalytic subunit Gcn5
62	SPAC19A8.10	rfp1	SUMO-targeted ubiquitin-protein ligase subunit Rfp1
63	SPAC19D5.06c	din1	RNA pyrophosphohydrolase Din1
64	SPAC19D5.11c	ctf8	Ctf18 RFC-like complex subunit Ctf8
65	SPAC19E9.02	fin1	serine/threonine protein kinase, NIMA related Fin1
66	SPAC19G12.13c	poz1	shelterin complex subunit Poz1

	Systematic ID	Symbol	Description
67	SPAC19G12.17	erh1	enhancer of rudimentary homolog Erh1
68	SPAC1B3.17	clr2	chromatin silencing protein Clr2
69	SPAC1D4.09c	rtf2	replication termination factor Rtf2
70	SPAC1D4.11c	lkh1	dual specificity protein kinase Lkh1
71	SPAC1F3.01	rrp6	exosome 3'-5' exoribonuclease subunit Rrp6
72	SPAC1F3.06c	spo15	mitotic and meiotic spindle pole body protein Spo15
73	SPAC1F7.01c	spt6	nucleosome remodeling protein Spt6
74	SPAC20G4.04c	hus1	checkpoint clamp complex protein Hus1
75	SPAC20G8.08c	fft1	SMARCAD1 family ATP-dependent DNA helicase Fft1 (predicted)
76	SPAC20H4.03c	tfs1	general transcription elongation factor TFIIS
77	SPAC20H4.10	ufd2	ubiquitin-protein ligase E4 Ufd2 (predicted)
78	SPAC21E11.03c	pcr1	transcription factor Pcr1
79	SPAC21E11.05c	cyp8	cyclophilin family peptidyl-prolyl cis-trans isomerase Cyp8
80	SPAC222.04c	ies6	Ino80 complex subunit Ies6
81	SPAC222.15	meu13	Tat binding protein 1(TBP-1)-interacting protein (TBPIP) homolog (predicted)
82	SPAC22A12.01c	pso2	DNA 5' exonuclease (predicted)
83	SPAC22E12.11c	set3	histone lysine methyltransferase Set3
84	SPAC22E12.19	snt1	Set3 complex subunit Snt1
85	SPAC22F3.02	atf31	transcription factor Atf31
86	SPAC22F3.09c	res2	MBF transcription factor complex subunit Res2
87	SPAC22F8.12c	shf1	small histone ubiquitination factor Shf1
88	SPAC22H12.02	tfg3	TFIID, TFIIIF, Ino80, SWI/SNF, and NuA3 complex subunit Tfg3
89	SPAC23A1.07		ubiquitin-protein ligase E3 (predicted)
90	SPAC23C11.08	php3	CCAAT-binding factor complex subunit Php3
91	SPAC23C11.15	pst2	Clr6 histone deacetylase complex subunit Pst2
92	SPAC23C4.03	hrk1	haspin related kinase Hrk1
93	SPAC23D3.01	pdp3	PWWP domain protein, involved in chromatin remodeling (predicted)
94	SPAC23D3.09	arp42	SWI/SNF and RSC complex subunit Arp42
95	SPAC23E2.01	fep1	iron-sensing transcription factor Fep1
96	SPAC23E2.03c	ste7	arrestin family meiotic suppressor protein Ste7
97	SPAC23G3.04	ies4	Ino80 complex subunit Ies4
98	SPAC23G3.07c	snf30	SWI/SNF complex subunit Snf30
99	SPAC23G3.08c	ubp7	ubiquitin C-terminal hydrolase Ubp7
100	SPAC23G3.10c	ssr3	SWI/SNF and RSC complex subunit Ssr3
101	SPAC23H3.05c	swd1	Set1C complex subunit Swd1

	Systematic ID	Symbol	Description
102	SPAC23H4.12	alp13	MRG family Clr6 histone deacetylase complex subunit Alp13
103	SPAC24B11.10c	cfh1	SEL1/TPR repeat protein Cfh1 (predicted)
104	SPAC25A8.01c	fft3	SMARCAD1 family ATP-dependent DNA helicase Fft3
105	SPAC25H1.02	jmj1	histone demethylase Jmj1 (predicted)
106	SPAC26H5.03	pcf2	CAF assembly factor (CAF-1) complex subunit B, Pcf2
107	SPAC29A4.09		rRNA exonuclease Rrp17 (predicted)
108	SPAC29A4.18	prw1	Clr6 histone deacetylase complex subunit Prw1
109	SPAC29B12.02c	set2	histone lysine H3-K36 methyltransferase Set2
110	SPAC29B12.03	spd1	ribonucleotide reductase (RNR) inhibitor
111	SPAC29B12.06c	rcd1	CCR4-Not complex RNA-binding protein subunit Rcd1
112	SPAC29B12.08	clr5	Clr5 protein
113	SPAC2C4.07c	dis32	3'-5'-exoribonuclease activity Dis3L2
114	SPAC2F3.15	lsk1	P-TEFb-associated cyclin-dependent protein kinase Lsk1
115	SPAC2F3.16		ubiquitin-protein ligase E3, implicated in DNA repair (predicted)
116	SPAC2F7.07c	cph2	Clr6 histone deacetylase associated PHD protein Cph2
117	SPAC2F7.08c	snf5	SWI/SNF complex subunit Snf5
118	SPAC2G11.05c	rim20	BRO1 domain protein Rim20
119	SPAC2G11.10c	uba42	thiosulfate sulfurtransferase, URM1 activating enzyme E1-type Uba42 (predicted)
120	SPAC30D11.07	nth1	DNA endonuclease III
121	SPAC31A2.09c	apm4	AP-2 adaptor complex mu subunit Apm4 (predicted)
122	SPAC31A2.16	gef2	RhoGEF Gef2
123	SPAC31G5.09c	spk1	MAP kinase Spk1
124	SPAC31G5.19	abo1	ATPase with bromodomain protein
125	SPAC323.03c		Schizosaccharomyces specific protein
126	SPAC328.05	hrb1	RNA-binding protein involved in export of mRNAs Hrb1 (predicted)
127	SPAC32A11.03c	phx1	stationary phase-specific homeobox transcription factor Phx1
128	SPAC343.04c	gid7	GID complex subunit Gid7 (predicted)
129	SPAC343.11c	msc1	Swr1 complex subunit Msc1
130	SPAC343.18	rfp2	SUMO-targeted ubiquitin-protein ligase subunit Rfp2
131	SPAC3A11.05c	kms1	meiotic spindle pole body KASH domain protein Kms1
132	SPAC3C7.08c	elf1	AAA family ATPase Elf1
133	SPAC3F10.10c	map3	pheromone M-factor receptor Map3
134	SPAC3F10.12c		transcription factor (predicted)
135	SPAC3G6.01	hrp3	ATP-dependent DNA helicase Hrp3
136	SPAC3G6.06c	rad2	FEN-1 endonuclease Rad2

	Systematic ID	Symbol	Description
137	SPAC3G6.11	chl1	ATP-dependent DNA helicase Chl1 (predicted)
138	SPAC3G9.07c	hos2	histone deacetylase (class I) Hos2
139	SPAC3H1.11	hsr1	transcription factor Hsr1
140	SPAC3H1.12c	snt2	Lid2 complex PHD finger subunit Snt2
141	SPAC3H8.08c		transcription factor (predicted)
142	SPAC4A8.09c	cwf21	complexed with Cdc5 protein Cwf21
143	SPAC4F8.11	sea2	SEA complex WD repeat subunit Sea2 (predicted)
144	SPAC4G9.06c	chz1	histone H2A-H2B dimer chaperone Chz1 (predicted)
145	SPAC4H3.02c	swc3	Swr1 complex subunit Swc3
146	SPAC4H3.05	srs2	ATP-dependent DNA helicase, UvrD subfamily
147	SPAC56F8.16	esc1	transcription factor Esc1 (predicted)
148	SPAC57A10.09c	nhp6	High-mobility group non-histone chromatin protein (predicted)
149	SPAC5D6.02c	mug165	Clr6 histone deacetylase complex subunit Mug165
150	SPAC5D6.08c	mes1	meiotic APC inhibitor Mes1
151	SPAC630.14c	tup12	transcriptional corepressor Tup12
152	SPAC631.02	bdf2	BET family double bromodomain protein Bdf2
153	SPAC637.09	rex1	3'-5'- exoribonuclease Rex1 (predicted)
154	SPAC644.14c	rad51	RecA family recombinase Rad51/Rhp51
155	SPAC664.01c	swi6	heterochromatin (HP1) family chromodomain protein Swi6
156	SPAC664.02c	arp8	Ino80 complex actin-like protein Arp8
157	SPAC664.07c	rad9	checkpoint clamp complex protein Rad9
158	SPAC664.15	caf4	CCR4-Not complex subunit Caf4/Mdv1 (predicted)
159	SPAC688.06c	slx4	structure-specific endonuclease subunit Slx4
160	SPAC694.06c	mrc1	claspin, Mrc1
161	SPAC6B12.05c	ies2	Ino80 complex subunit Ies2
162	SPAC6B12.07c		ubiquitin-protein ligase E3 with SPX domain, human LORNRF1 ortholog (predicted)
163	SPAC6B12.14c		conserved fungal protein
164	SPAC6B12.16	meu26	DUF4451 family conserved fungal protein
165	SPAC6F12.09	rdp1	RNA-directed RNA polymerase Rdp1
166	SPAC6F6.09	eaf6	Mst2/NuA4 histone acetyltransferase complex subunit Eaf6
167	SPAC6G9.03c	mug183	histone H3.3 H4 heterotetramer chaperone Rtt106-like (predicted)
168	SPAC6G9.10c	sen1	ATP-dependent 5' to 3' DNA/RNA helicase Sen1
169	SPAC6G9.16c	xrc4	XRCC4 nonhomologous end joining factor Xrc4
170	SPAC7D4.04	atg11	autophagy associated protein Atg11
171	SPAC7D4.14c	iss10	NURS complex subunit Iss10

	Systematic ID	Symbol	Description
172	SPAC821.07c	moc3	transcription factor Moc3
173	SPAC823.03	ppk15	serine/threonine protein kinase Ppk15 (predicted)
174	SPAC824.04	swd22	mRNA cleavage and polyadenylation specificity factor complex, WD repeat protein Swd22
175	SPAC890.07c	rmt1	type I protein arginine N-methyltransferase Rmt1
176	SPAC8C9.14	prr1	transcription factor Prr1
177	SPAC8C9.17c	spc34	DASH complex subunit Spc34
178	SPAC8F11.03	msh3	MutS protein homolog 3
179	SPAC9E9.08	rad26	ATRIP, ATR checkpoint kinase regulatory subunit Rad26
180	SPAC9E9.10c	cbh1	CENP-B homolog Cbh1
181	SPAP14E8.02	tos4	chromatin binding FHA domain protein Tos4 (predicted)
182	SPAP27G11.15	slx1	structure-specific endonuclease catalytic subunit Slx1
183	SPAP32A8.03c	bop1	ubiquitin-protein ligase E3, human RNF126 ortholog (predicted)
184	SPAP8A3.02c	ofd2	histone H2A dioxygenase Ofd2
185	SPAPB1E7.02c	mcl1	DNA polymerase alpha accessory factor Mcl1
186	SPAPB24D3.01	toe3	transcription factor (predicted)
187	SPAPB2B4.03	cig2	G1/S-specific B-type cyclin Cig2
188	SPBC1105.04c	cbp1	CENP-B homolog
189	SPBC119.08	pmk1	MAP kinase Pmk1
190	SPBC119.14	rti1	Rad22 homolog Rti1
191	SPBC1198.11c	reb1	RNA polymerase I transcription termination factor/ RNA polymerase II transcription factor Reb1
192	SPBC11B10.05c	rsp1	random septum position protein, DNAJ domain protein Rsp1
193	SPBC11B10.08		WW domain containing conserved fungal protein
194	SPBC11B10.10c	pht1	histone H2A variant H2A.Z, Pht1
195	SPBC1347.07	rex2	RNA exonuclease (predicted)
196	SPBC13E7.08c	leo1	RNA polymerase II associated Paf1 complex subunit Leo1
197	SPBC13G1.08c	ash2	Ash2-trithorax family protein
198	SPBC146.06c	fan1	DNA repair protein Fan1
199	SPBC14C8.17c	spt8	SAGA complex subunit Spt8
200	SPBC14F5.07	doa10	ER ubiquitin-protein ligase E3 Doa10 (predicted)
201	SPBC15C4.01c	oca3	TPR repeat protein Oca3/ ER membrane protein complex Ecm2 (predicted)
202	SPBC15C4.06c		ubiquitin-protein ligase E3 Meu34, human RNF13 family homolog, unknown biological role (predicted)
203	SPBC15D4.03	slm9	histone H3.3 H4 chaperone, hira family Slm9
204	SPBC1604.09c	rex4	exoribonuclease Rex4 (predicted)

	Systematic ID	Symbol	Description
205	SPBC1604.16c		RNA-binding protein, G-patch type, human GPANK1 ortholog
206	SPBC1685.08	cti6	histone deacetylase complex ubiquitin-like protein ligase subunit Cti6
207	SPBC16A3.07c	nrm1	MBF complex corepressor Nrm1
208	SPBC16A3.19	eaf7	histone acetyltransferase complex subunit Eaf7
209	SPBC16D10.07c	sir2	Sirtuin family histone deacetylase Sir2
210	SPBC16E9.11c	pub3	HECT-type ubiquitin-protein ligase E3 Pub3 (predicted)
211	SPBC16E9.12c	pab2	poly(A) binding protein Pab2
212	SPBC16G5.03	mrz1	ubiquitin-protein ligase E3/SUMO transferase, Topors, possibly associated with DNA damage (predicted)
213	SPBC16G5.15c	fkh2	forkhead transcription factor Fkh2
214	SPBC16G5.17		transcription factor, zf-fungal binuclear cluster type (predicted)
215	SPBC1703.04	mlh1	MutL family protein Mlh1 (predicted)
216	SPBC1703.14c	top1	DNA topoisomerase I
217	SPBC1709.11c	png2	ING family histone acetyltransferase complex PHD-type zinc finger subunit Png2
218	SPBC1711.14	rec15	meiotic recombination protein Rec15
219	SPBC1718.02	hop1	linear element associated protein Hop1
220	SPBC1734.06	rhp18	Rad18 homolog ubiquitin protein ligase E3, Rhp18
221	SPBC1734.15	rsc4	RSC complex subunit Rsc4
222	SPBC1773.16c		transcription factor, zf-fungal binuclear cluster type(predicted)
223	SPBC1778.10c	ppk21	serine/threonine protein kinase Ppk21 (predicted)
224	SPBC17D11.04c	nto1	histone acetyltransferase complex PHD finger subunit Nto1 (predicted)
225	SPBC17G9.05	rct1	cyclophilin family peptidyl-prolyl cis-trans isomerase, RRM-containing Rct1
226	SPBC18H10.06c	swd2	Set1C complex subunit Swd2.1
227	SPBC18H10.15	cdk11	serine/threonine protein kinase Cdk11
228	SPBC19C7.02	ubr1	N-end-recognizing protein, UBR ubiquitin-protein ligase E3 Ubr1
229	SPBC1A4.03c	top2	DNA topoisomerase II
230	SPBC1D7.03	clg1	cyclin-like protein involved in autophagy Clg1 (predicted)
231	SPBC1D7.04	mlo3	RNA binding protein Mlo3
232	SPBC20F10.05	nrl1	RNAi-mediated silencing protein, human NRDE2 ortholog Nrl1
233	SPBC20F10.10	psl1	cyclin pho85 family Psl1 (predicted)
234	SPBC215.03c	csn1	COP9/signalosome complex subunit Csn1
235	SPBC215.06c		nucleolar RNA-binding protein, human LYAR homolog, implicated in transcriptional regulation
236	SPBC215.07c	pdp2	PWWP domain protein Pdp2 (predicted)

	Systematic ID	Symbol	Description
237	SPBC216.05	rad3	ATR checkpoint kinase Rad3
238	SPBC216.06c	swi1	replication fork protection complex subunit Swi1
239	SPBC21B10.13c	yox1	MBF complex corepressor Yox1
240	SPBC21C3.02c	dep1	Sds3-like family protein Dep1
241	SPBC21C3.20c	git1	C2 domain protein Git1
242	SPBC21D10.09c	rkr1	RQC complex ubiquitin-protein ligase E3 Rkr1 (predicted)
243	SPBC21D10.10	bdc1	bromodomain protein Bdc1
244	SPBC23E6.02	rrp2	ATP-dependent DNA helicase/ ubiquitin-protein ligase E3 (predicted)
245	SPBC23E6.09	ssn6	transcriptional corepressor Ssn6
246	SPBC23G7.13c		plasma membrane urea transmembrane transporter (predicted)
247	SPBC24C6.05	sec28	coatomer epsilon subunit (predicted)
248	SPBC25B2.08		Schizosaccharomyces pombe specific protein
249	SPBC26H8.09c	snf59	SWI/SNF complex subunit Snf59
250	SPBC28E12.02		RNA-binding protein
251	SPBC28F2.07	sfr1	Swi five-dependent recombination mediator Sfr1
252	SPBC28F2.10c	ngg1	SAGA complex subunit Ngg1/Ada3
253	SPBC29A10.03c	pcf1	CAF assembly factor (CAF-1) complex large subunit Pcf1
254	SPBC29A10.05	exo1	exonuclease I Exo1
255	SPBC29A10.14	rec8	meiotic cohesin complex subunit Rec8
256	SPBC29A3.03c	gid2	GID complex ubiquitin-protein ligase E3 subunit Gid2/Rmd5 (predicted)
257	SPBC29A3.05	vps71	Swr1 complex subunit Vps71
258	SPBC29A3.13	pdp1	PWWP domain protein Pdp1
259	SPBC29B5.01	atf1	transcription factor, Atf-CREB family Atf1
260	SPBC2A9.04c	san1	sir antagonist, ubiquitin-protein ligase E3
261	SPBC2D10.11c	nap2	histone H2A-H2B chaperone Nap2
262	SPBC2D10.17	clr1	SHREC complex intermodule linker subunit Clr1
263	SPBC2F12.09c	atf21	transcription factor, Atf-CREB family Atf21
264	SPBC2F12.12c	cay1	cactin, spliceosome complex subunit
265	SPBC2G2.06c	apl1	AP-2 adaptor complex beta subunit Apl1 (predicted)
266	SPBC2G2.14	csi1	mitotic centromere-SPB clustering protein Csi1
267	SPBC2G5.02c	ckb2	CK2 family regulatory subunit Ckb2 (predicted)
268	SPBC30B4.04c	sol1	SWI/SNF complex subunit Sol1
269	SPBC30D10.10c	tor1	serine/threonine protein kinase Tor1
270	SPBC31F10.07	lsb5	actin cortical patch component Lsb5 (predicted)

	Systematic ID	Symbol	Description
271	SPBC31F10.10c	mub1	Armadillo-type fold protein, zf-MYND type zinc finger protein, Mub1-Rad6-Ubr2 ubiquitin ligase complex Mub1 (predicted)
272	SPBC31F10.13c	hip1	histone H3.3 H4 chaperone, hira family Hip1
273	SPBC31F10.14c	hip3	HIRA interacting protein Hip3
274	SPBC32F12.07c		membrane associated ubiquitin-protein ligase E3, MARCH family (predicted)
275	SPBC32H8.06	mug93	TPR repeat protein, meiotically spliced
276	SPBC337.03	rhn1	RNA polymerase II transcription termination factor homolog
277	SPBC342.05	crb2	DNA repair protein Rad9 homolog Crb2
278	SPBC342.06c	rtt109	RTT109 family histone lysine acetyltransferase
279	SPBC354.03	swd3	WD repeat protein Swd3
280	SPBC354.05c	sre2	membrane-tethered transcription factor Sre2
281	SPBC365.10	arp5	Ino80 complex actin-like protein Arp5
282	SPBC36B7.05c	pib1	endosomal and vacuolar ubiquitin-protein ligase E3/phosphatidylinositol(3)-phosphate binding protein Pib1
283	SPBC36B7.08c	ccp1	histone chaperone, CENP-A nucleosome disassembly Ccp1
284	SPBC3B8.02	php5	CCAAT-binding factor complex subunit Php5
285	SPBC3D6.04c	mad1	mitotic spindle checkpoint protein Mad1
286	SPBC3D6.09	dpb4	DNA polymerase epsilon subunit Dpb4
287	SPBC3H7.13	far10	SIP/FAR complex FHA domain subunit Far10/Csc1
288	SPBC4.05	mlo2	ubiquitin protein ligase E3 component human N-recogin 7 homolog Mlo2
289	SPBC428.06c	rxt2	histone deacetylase complex subunit Rxt2
290	SPBC428.08c	clr4	histone lysine H3 methyltransferase Clr4
291	SPBC4B4.03	rsc1	RSC complex subunit Rsc1
292	SPBC4C3.12	1-Sep	forkhead transcription factor Sep1
293	SPBC530.08		membrane-tethered transcription factor (predicted)
294	SPBC530.14c	dsk1	SR protein-specific kinase Dsk1
295	SPBC543.07	pek1	MAP kinase kinase Pek1
296	SPBC56F2.03	arp10	dynactin complex actin-like protein Arp10 (predicted)
297	SPBC56F2.05c		transcription factor (predicted)
298	SPBC582.04c	dsh1	RNAi protein, Dsh1
299	SPBC582.06c	mcp6	horsetail movement protein Hrs1/Mcp6
300	SPBC609.05	pob3	histone H2A-H2B chaperone, FACT complex subunit Pob3
301	SPBC651.11c	apm3	AP-3 adaptor complex subunit Apm3 (predicted)
302	SPBC660.06		WW domain containing conserved fungal protein

	Systematic ID	Symbol	Description
303	SPBC660.14	mik1	mitotic inhibitor kinase Mik1
304	SPBC6B1.04	mde4	microtubule-site clamp monopolin complex subunit Mde4
305	SPBC6B1.06c	ubp14	Lys48-specific deubiquitinase Ubp14
306	SPBC725.02	mpr1	histidine-containing response regulator phosphotransferase Mpr1
307	SPBC725.11c	php2	CCAAT-binding factor complex subunit Php2
308	SPBC776.02c	dis2	serine/threonine protein phosphatase PP1, Dis2
309	SPBC776.16	mis20	centromere protein Mis20/Eic2
310	SPBC800.03	clr3	histone deacetylase (class II) Clr3
311	SPBC83.03c	tas3	RITS complex subunit 3
312	SPBC902.02c	ctf18	Ctf18 RFC-like complex subunit Ctf18
313	SPBC902.04	rmn1	RNA-binding protein
314	SPBC902.06	mto2	gamma tubulin complex linker Mto2
315	SPBP16F5.03c	tra1	SAGA complex phosphatidylinositol pseudokinase Tra1
316	SPBP22H7.05c	abo2	ATPase with bromodomain protein (predicted)
317	SPBP23A10.05	ssr4	SWI/SNF and RSC complex subunit Ssr4
318	SPBP35G2.08c	air1	TRAMP complex zinc knuckle subunit Air1
319	SPBP35G2.10	mit1	SHREC complex ATP-dependent DNA helicase subunit Mit1
320	SPBP35G2.13c	swc2	Swr1 complex subunit Swc2
321	SPBP8B7.07c	set6	histone lysine methyltransferase Set6 (predicted)
322	SPBP8B7.23	rnf10	ubiquitin-protein ligase E3 (predicted)
323	SPBP8B7.28c	stc1	CLRC ubiquitin ligase complex linker protein, LIM-like Stc1
324	SPCC1020.12c	xap5	xap-5-like protein
325	SPCC11E10.08	rik1	CLRC ubiquitin ligase complex WD repeat protein Rik1
326	SPCC1223.13	cbf12	CBF1/Su(H)/LAG-1 family transcription factor Cbf12
327	SPCC1235.05c	fft2	SMARCAD1 family ATP-dependent DNA helicase Fft2 (predicted)
328	SPCC1235.09	hif2	Set3 complex subunit Hif2
329	SPCC1235.12c	mug146	Schizosaccharomyces specific protein Mug46
330	SPCC1259.04	iec3	Ino80 complex subunit Iec3
331	SPCC1259.07	rxt3	transcriptional regulatory protein Rxt3
332	SPCC126.02c	pku70	Ku domain protein Pku70
333	SPCC126.04c	sgf73	SAGA complex deubiquitinating submodule subunit Sgf73
334	SPCC126.07c	asr1	ubiquitin-protein ligase E3 Asr1 (predicted)
335	SPCC126.11c		RNA-binding protein, rrm type
336	SPCC126.13c	sap18	splicing factor Sap18 (predicted)
337	SPCC132.02	hst2	Sirtuin family histone deacetylase Hst2

	Systematic ID	Symbol	Description
338	SPCC1393.02c	spt2	non-specific DNA binding protein Spt2 (predicted)
339	SPCC1393.05	ers1	RNA-silencing factor Ers1
340	SPCC1442.13c	sqs2	R3H and G-patch domain protein Sqs2
341	SPCC1450.02	bdf1	Swr1 complex bromodomain subunit Bdf1
342	SPCC1450.03	utp502	ribonucleoprotein (RNP) complex Utp502 (predicted)
343	SPCC1494.03	arz1	human RAP1 GTPase-GDP dissociation stimulator ortholog, Zfs1 target number 1
344	SPCC162.11c	urk1	uridine kinase/uracil phosphoribosyltransferase (predicted)
345	SPCC1620.14c	snf22	ATP-dependent DNA helicase Snf22
346	SPCC1682.13	laf2	Clr6 associated factor 2, Laf2
347	SPCC16C4.11	pef1	Pho85/PhoA-like cyclin-dependent kinase Pef1
348	SPCC1739.03	hrr1	Helicase Required for RNAi-mediated heterochromatin assembly Hrr1
349	SPCC1739.05	set5	histone lysine methyltransferase Set5 (predicted)
350	SPCC1739.07	cti1	exosome C1D family subunit Cti1
351	SPCC1739.12	ppe1	serine/threonine protein phosphatase Ppe1
352	SPCC1753.03c	rec7	meiotic recombination protein Rec7
353	SPCC1840.04	pca1	metacaspase Pca1
354	SPCC188.07	ccq1	shelterin complex HEAT repeat subunit Ccq1
355	SPCC188.13c	dcr1	dicer
356	SPCC18B5.03	wee1	M phase inhibitor protein kinase Wee1
357	SPCC18B5.07c	nup61	nucleoporin Nup61
358	SPCC24B10.07	gad8	AGC family protein kinase Gad8
359	SPCC24B10.08c	ada2	SAGA complex subunit Ada2
360	SPCC24B10.14c	xlf1	XRCC4-like nonhomologous end joining factor, Cernunnon Xlf1/Nej1
361	SPCC24B10.19c	nts1	Clr6 histone deacetylase complex subunit Nts1
362	SPCC297.03	ssp1	Ca ²⁺ /calmodulin-dependent (CaMMK)-like protein kinase Ssp1
363	SPCC297.04c	set7	histone lysine H3-K37 methyltransferase Set7
364	SPCC2H8.05c	dbl1	double strand break localizing Dbl1
365	SPCC306.04c	set1	histone lysine H3-K4 methyltransferase Set1
366	SPCC31H12.08c	ccr4	CCR4-Not complex 3'-5'-exoribonuclease subunit Ccr4
367	SPCC330.01c	rhp16	Rad16 homolog ATP-dependent DNA helicase/ ubiquitin protein ligase E3 Rhp16
368	SPCC330.02	rhp7	Rad7 homolog Rhp7
369	SPCC338.16	pof3	F-box protein Pof3
370	SPCC364.02c	bis1	splicing factor Bis1
371	SPCC364.06	nap1	histone H2A-H2B chaperone Nap1

	Systematic ID	Symbol	Description
372	SPCC417.07c	mto1	gamma tubulin complex linker Mto1
373	SPCC417.09c		transcription factor (predicted)
374	SPCC4B3.12	set9	histone lysine H4-K20 methyltransferase Set9
375	SPCC4G3.15c	not2	CCR4-Not complex NOT box subunit Not2
376	SPCC4G3.19	alp16	gamma tubulin complex subunit Alp16
377	SPCC548.05c	dbl5	ubiquitin-protein ligase E3 Dbl5
378	SPCC550.12	arp6	actin-like protein Arp6
379	SPCC550.15c	rei1	ribosome biogenesis protein Rei1 (predicted)
380	SPCC553.04	cyp9	WD repeat containing cyclophilin family peptidyl-prolyl cis-trans isomerase Cyp9 (predicted)
381	SPCC576.13	swc5	Swr1 complex subunit Swc5
382	SPCC594.05c	spf1	Set1C ubiquitin-protein ligase E3 subunit Spf1
383	SPCC61.02	spt3	SAGA complex subunit Spt3
384	SPCC613.12c	raf1	CLRC ubiquitin ligase complex WD repeat subunit Raf1/Dos1
385	SPCC622.15c		Schizosaccharomyces specific protein
386	SPCC622.16c	epe1	Jmjc domain chromatin associated protein Epe1
387	SPCC622.19	jmj4	peptidyl-lysine 3-dioxygenase activity jmj4 (predicted)
388	SPCC645.13	bye1	transcription elongation regulator Bye1 (predicted)
389	SPCC663.11	saf1	splicing associated factor Saf1
390	SPCC663.12	cid12	poly(A) polymerase Cid12
391	SPCC736.08	cbf11	CBF1/Su(H)/LAG-1 family transcription factor Cbf11
392	SPCC736.11	ago1	argonate
393	SPCC757.09c	rnc1	KH domain RNA-binding protein Rnc1
394	SPCC895.06	elp2	elongator complex WD repeat protein Elp2 (predicted)
395	SPCC895.07	alp14	TOG/XMAP215 microtubule plus end tracking polymerase Alp14
396	SPCC970.07c	raf2	CLRC ubiquitin ligase complex subunit Raf2

Table S1.2. Strain table.List of *S. pombe* strains used in this study.

Strain	Genotype
PAS075	Locus2:: <i>ade6p::3xE2C:hygMX</i> at Locus2 (between SPBC1711.11 and SPBC1711.12)
PM003	Wild-type strain: h(+); <i>ura4-D18</i> ; <i>leu1-32</i> ; <i>ade6-M216</i> ; <i>his7-366</i>
PM006	972 h- wild-type
PAS193	$\Delta K::ade6p:mKO2$; <i>ade6p:SF-GFP</i> between <i>REIII</i> and <i>mat3M</i> ; <i>ade6p:3xE2C:hygMX</i> at Locus2; <i>clr4::kanMX</i> , h(-)
PAS216	<i>cenH::ade6p:SF-GFP(Kint2)</i> ; <i>mat3m(EcoRV)::ade6p:mKO2</i> ; <i>ade6p:3xE2C:hygMX</i> at Locus2; <i>clr4::kanMX</i> , h90
PAS217	<i>cenH:ade6p:SF-GFP (Kint2)</i> ; <i>mat3m(EcoRV)::ade6p:mKO2</i> ; <i>ade6p:3xE2C:hygMX</i> at Locus2, h90
PAS231	<i>ura4::natMX:dh:ade6p:SF-GFP</i> , <i>ade6p:mKO2</i> 3 kb, <i>leu1::ade6p:3xE2C:hygMX</i>
PAS331	<i>cenH::ade6p:SF-GFP (Kint2)</i> ; <i>mat3m(EcoRV)::ade6p:mKO2</i> ; <i>ade6p:3xE2C:hygMX</i> at Locus2; $\Delta REIII::REIII(\Delta s1, \Delta s2)$ in <i>clr4::kanMX</i> , h90
PAS332	<i>cenH::ade6p:SF-GFP (Kint2)</i> ; <i>mat3m(EcoRV)::ade6p:mKO2</i> ; <i>ade6p:3xE2C:hygMX</i> at Locus2; $\Delta REIII::REIII(\Delta s1, \Delta s2)$, h90
PAS353	<i>ura4::natMX:dh:ade6p:SF-GFP</i> , <i>ade6p:mKO2</i> 3 kb, <i>leu1::ade6p:3xE2C:hygMX</i> ; <i>gcn5::kanMX</i>
PAS482	$\Delta K::ade6p:mKO2$; <i>ade6p:SF-GFP</i> between <i>REIII</i> and <i>mat3M</i> ; <i>ade6p:3xE2C:hygMX</i> at Locus2, h(-); 'OFF' allele
PAS795	<i>cenH:ade6p:SF-GFP (Kint2)</i> ; <i>mat3m(EcoRV)::ade6p:mKO2</i> ; <i>ade6p:3xE2C:hygMX</i> at Locus2; <i>fkh2::natMX</i>
PAS796	<i>cenH:ade6p:SF-GFP (Kint2)</i> ; <i>mat3m(EcoRV)::ade6p:mKO2</i> ; <i>ade6p:3xE2C:hygMX</i> at Locus2; <i>prw1::kanMX</i>
PAS797	<i>cenH:ade6p:SF-GFP (Kint2)</i> ; <i>mat3m(EcoRV)::ade6p:mKO2</i> ; <i>ade6p:3xE2C:hygMX</i> at Locus2; <i>png3::kanMX</i>
PAS798	<i>cenH::ade6p:SF-GFP (Kint2)</i> ; <i>mat3m(EcoRV)::ade6p:mKO2</i> ; <i>ade6p:3xE2C:hygMX</i> at Locus2; $\Delta REIII::REIII(\Delta s1, \Delta s2)$; <i>fkh2::natMX</i>
PAS799	<i>cenH::ade6p:SF-GFP (Kint2)</i> ; <i>mat3m(EcoRV)::ade6p:mKO2</i> ; <i>ade6p:3xE2C:hygMX</i> at Locus2; $\Delta REIII::REIII(\Delta s1, \Delta s2)$; <i>prw1::kanMX</i>
PAS800	<i>cenH::ade6p:SF-GFP (Kint2)</i> ; <i>mat3m(EcoRV)::ade6p:mKO2</i> ; <i>ade6p:3xE2C:hygMX</i> at Locus2; $\Delta REIII::REIII(\Delta s1, \Delta s2)$; <i>png3::kanMX</i>
PAS803	$\Delta K::ade6p:mKO2$; <i>ade6p:SF-GFP</i> between <i>REIII</i> and <i>mat3M</i> ; <i>ade6p:3xE2C:hygMX</i> at Locus2; 'OFF' allele; <i>fkh2::natMX</i>
PAS808	<i>cenH:ade6p:SF-GFP (Kint2)</i> ; <i>mat3m(EcoRV)::ade6p:mKO2</i> ; <i>ade6p:3xE2C:hygMX</i> at Locus2; <i>fkh2::natMX</i> ; <i>prw1::kanMX</i> by cross
PAS809	<i>cenH:ade6p:SF-GFP (Kint2)</i> ; <i>mat3m(EcoRV)::ade6p:mKO2</i> ; <i>ade6p:3xE2C:hygMX</i> at Locus2; <i>fkh2::natMX</i> ; <i>prw1::kanMX</i> by sequential knockout
PAS810	<i>cenH::ade6p:SF-GFP (Kint2)</i> ; <i>mat3m(EcoRV)::ade6p:mKO2</i> ; <i>ade6p:3xE2C:hygMX</i> at Locus2; $\Delta REIII::REIII(\Delta s1, \Delta s2)$; <i>fkh2::natMX</i> ; <i>prw1::kanMX</i> by cross
PAS811	<i>cenH::ade6p:SF-GFP (Kint2)</i> ; <i>mat3m(EcoRV)::ade6p:mKO2</i> ; <i>ade6p:3xE2C:hygMX</i> at Locus2; $\Delta REIII::REIII(\Delta s1, \Delta s2)$; <i>fkh2::natMX</i> ; <i>prw1::kanMX</i> by sequential knockout

Strain	Genotype
PAS813	<i>cenH:: ade6p:SF-GFP (Kint2); mat3m(EcoRV):: ade6p:mKO2; ade6p:3xE2C:hygMX at Locus2; ΔREIII::REIII(Δs1, Δs2); apm3::natMX</i>
PAS816	<i>apl5:SF-GFP:hygMX; Swi6:E2C:kanMX</i>
PAS817	<i>apm3:SF-GFP:hygMX; Swi6:E2C:kanMX</i>
PAS833	<i>fkh2::Fkh2:13XMYC Zilio et al.</i>
PAS836	<i>clr6::Clr6:13XMYC:hygMX; fkh2::Fkh2:TAP:kanMX Zilio et al.</i>
PAS838	<i>fkh2::Fkh2:13XMYC:hygMX; sds3::Sds3:TAP:kanMX Zilio et al.</i>
PAS839	<i>cenH:: ade6p:SF-GFP (Kint2); mat3m(EcoRV):: ade6p:mKO2; ade6p:3xE2C:hygMX at Locus2; ΔREIII::REIII(Δs1, Δs2); clr6-1, h90</i>
PAS841	<i>cenH:: ade6p:SF-GFP (Kint2); mat3m(EcoRV):: ade6p:mKO2; ade6p:3xE2C:hygMX at Locus2; ΔREIII::REIII(Δs1, Δs2), fkh2::Fkh2:13XMYC:hygMX, h90</i>
PAS842	<i>cenH:: ade6p:SF-GFP (Kint2); mat3m(EcoRV):: ade6p:mKO2; ade6p:3xE2C:hygMX at Locus2; ΔREIII::REIII(Δs1, Δs2); clr3-D232N:natMX, h90</i>
PAS850	<i>cenH:: ade6p:SF-GFP (Kint2); mat3m(EcoRV):: ade6p:mKO2; ade6p:3xE2C:hygMX at Locus2; ΔREIII::REIII(Δs1, Δs2), fkh2::Fkh2:13XMYC:hygMX; prw1::kanMX, h90</i>
PAS867	<i>cenH:: ade6p:SF-GFP (Kint2); mat3m(EcoRV):: ade6p:mKO2; ade6p:3xE2C:kanMX at Locus2; ΔREIII::REIII(Δs1, Δs2), clr6::Clr6:13XMYC:hygMX, h90</i>
PAS868	<i>cenH:: ade6p:SF-GFP (Kint2); mat3m(EcoRV):: ade6p:mKO2; ade6p:3xE2C:kanMX at Locus2; ΔREIII::REIII(Δs1, Δs2), clr6::Clr6:13XMYC:hygMX; fkh2::natMX, h90</i>
PAS869	<i>cenH:: ade6p:SF-GFP (Kint2); mat3m(EcoRV):: ade6p:mKO2; ade6p:3xE2C:kanMX at Locus2; ΔREIII::REIII(Δs1, Δs2), apl5::kanMX; apm3::natMX, h90</i>
PAS870	<i>cenH:: ade6p:SF-GFP (Kint2); mat3m(EcoRV):: ade6p:mKO2; ade6p:3xE2C:kanMX at Locus2; ΔREIII::REIII(Δs1, Δs2), apl5::kanMX, h90</i>
PAS889	<i>cenH:: ade6p:SF-GFP (Kint2); mat3m(EcoRV):: ade6p:mKO2; ade6p:3xE2C:kanMX at Locus2; saf5::kanMX, h90</i>
PAS890	<i>cenH:: ade6p:SF-GFP (Kint2); mat3m(EcoRV):: ade6p:mKO2; ade6p:3xE2C:kanMX at Locus2; eaf6::kanMX, h90</i>
PAS891	<i>cenH:: ade6p:SF-GFP (Kint2); mat3m(EcoRV):: ade6p:mKO2; ade6p:3xE2C:kanMX at Locus2; pht1::kanMX, h90</i>
PAS892	<i>cenH:: ade6p:SF-GFP (Kint2); mat3m(EcoRV):: ade6p:mKO2; ade6p:3xE2C:kanMX at Locus2; hip1::kanMX, h90</i>
PAS893	<i>cenH:: ade6p:SF-GFP (Kint2); mat3m(EcoRV):: ade6p:mKO2; ade6p:3xE2C:kanMX at Locus2; gad8::kanMX, h90</i>
PAS894	<i>ΔK::ade6p:mKO2; ade6p: SF-GFP between REIII and mat3M; ade6p:3xE2C:hygMX at Locus2, h(-); pht1::kanMX, h90</i>
PAS895	<i>ΔK::ade6p:mKO2; ade6p: SF-GFP between REIII and mat3M; ade6p:3xE2C:hygMX at Locus2, h(-); hip1::kanMX, h90</i>
PAS896	<i>ΔK::ade6p:mKO2; ade6p: SF-GFP between REIII and mat3M; ade6p:3xE2C:hygMX at Locus2, h(-); gad8::kanMX, h90</i>
PAS897	<i>ΔK::ade6p:mKO2; ade6p: SF-GFP between REIII and mat3M; ade6p:3xE2C:hygMX at Locus2, h(-); hip1::kanMX, h90</i>

Strain	Genotype
PAS898	$\Delta K::ade6p:mKO2$; <i>ade6p</i> : SF-GFP between <i>REIII</i> and <i>mat3M</i> ; <i>ade6p:3xE2C:hygMX</i> at Locus2, h(-); <i>gad8::kanMX</i> , h90
PAS900	<i>ura4::natMX:dh:ade6p:SF-GFP</i> , <i>ade6p:mKO2</i> 3 kb, <i>leu1::ade6p:3xE2C:hygMX</i> ; <i>eaf6::kanMX</i>
PAS901	<i>ura4::natMX:dh:ade6p:SF-GFP</i> , <i>ade6p:mKO2</i> 3 kb, <i>leu1::ade6p:3xE2C:hygMX</i> ; <i>pht1::kanMX</i>
PAS902	<i>ura4::natMX:dh:ade6p:SF-GFP</i> , <i>ade6p:mKO2</i> 3 kb, <i>leu1::ade6p:3xE2C:hygMX</i> ; <i>hip1::kanMX</i>
PAS903	<i>ura4::natMX:dh:ade6p:SF-GFP</i> , <i>ade6p:mKO2</i> 3 kb, <i>leu1::ade6p:3xE2C:hygMX</i> ; <i>gad8::kanMX</i>
PAS904	<i>cenH::ade6p:SF-GFP</i> (Kint2); <i>mat3m(EcoRV)::ade6p:mKO2</i> ; <i>ade6p:3xE2C:kanMX</i> at Locus2; $\Delta REIII::REIII(\Delta s1, \Delta s2)$; <i>saf5::kanMX</i> , h90
PAS905	<i>cenH::ade6p:SF-GFP</i> (Kint2); <i>mat3m(EcoRV)::ade6p:mKO2</i> ; <i>ade6p:3xE2C:kanMX</i> at Locus2; $\Delta REIII::REIII(\Delta s1, \Delta s2)$; <i>eaf6::kanMX</i> , h90
PAS906	<i>cenH::ade6p:SF-GFP</i> (Kint2); <i>mat3m(EcoRV)::ade6p:mKO2</i> ; <i>ade6p:3xE2C:kanMX</i> at Locus2; $\Delta REIII::REIII(\Delta s1, \Delta s2)$; <i>pht1::kanMX</i> , h90
PAS907	<i>cenH::ade6p:SF-GFP</i> (Kint2); <i>mat3m(EcoRV)::ade6p:mKO2</i> ; <i>ade6p:3xE2C:kanMX</i> at Locus2; $\Delta REIII::REIII(\Delta s1, \Delta s2)$; <i>hip1::kanMX</i> , h90
PAS908	<i>cenH::ade6p:SF-GFP</i> (Kint2); <i>mat3m(EcoRV)::ade6p:mKO2</i> ; <i>ade6p:3xE2C:kanMX</i> at Locus2; $\Delta REIII::REIII(\Delta s1, \Delta s2)$; <i>gad8::kanMX</i> , h90
PAS932	<i>smt-0</i> h(-); <i>ura4-D18</i> ; <i>leu1-32</i> ; <i>ade6-M216</i> ; <i>his7-366</i> ; <i>clr6-1</i>
PAS933	<i>smt-0</i> h(-); <i>ura4-D18</i> ; <i>leu1-32</i> ; <i>ade6-M216</i> ; <i>his7-366</i> ; <i>prw1::kanMX</i>

Table S1.3. Primers used for ChIP qPCR and RT qPCR.

Primers for amplicons used in qPCR in this study.

oligo	target	sequence
OAS 0367	orange F	AATTTTCCTGCTGATGGTCCT
OAS 0368	orange R	TGATCACCAGGCATTTCAAG
OAS 0846	green F	CTGCTGATAAGCAAAAGAACG
OAS 0847	green R	CCATATGATCACGCTTTTTCG
OAS 1044	dg F	CCATCACCACCTTTCATCTCC
OAS 1045	df R	CAGGATACCTAGACGCACAA
OAS 1362	dh F	TTTAAAGCTTCACTACCATCGAAA
OAS 1363	dh R	TGCCAACAGTTTTTCCAACCTT
OAS 1569	MAT distal F	tgcaagttatctcaacgctgct
OAS 1570	MAT distal R	gcttggtgcttgggatgttt
OAS 1601	mtd1 F	CCTGCCAGCAAGGAGAGGTT
OAS 1602	mtd1 R	TGGTACTTACTGCAGCTATGGTTAGG
OAS 1822	mei4 F	CCCCCTCTTCCCCCTTCTAA
OAS 1823	mei4 R	AAAGGCTAGACTCATGGGCATC
OAS 2087	mcp7 F	GGAAGCTGCCAATTTGTGGA
OAS 2088	mcp7 R	TTGCAGATCGTCCAAATCCTC
OAS 2091	ssm4 F	CAATTCCAAGCCCATTGACC
OAS 2092	ssm4 R	TGAAAACCTGGGTCGCTCGAT
OAS 2097	SB_TEL1L_3 F	TAATGAGTTGCCCCGGGTAT
OAS 2098	SB_TEL1L_3 R	CCGAATGGCAAGATGGTAAT
OAS 2099	SB_TEL1L_7 F	CACAGACGTCTCCTGGTGTC
OAS 2100	SB_TEL1L_7 R	TGCAGAGTTTGCGGTACTIONT

Chapter 2

Phosphate-binding pocket on cyclin regulates mitotic timing

Phosphate-binding pocket on cyclin regulates mitotic timing

Henry Ng^{1,2}, David O. Morgan^{1,*}

¹Department of Physiology, University of California San Francisco, San Francisco, CA 94143, USA,

²TETRAD graduate program, University of California San Francisco, San Francisco, CA 94143, USA,

*Correspondence: David.morgna@ucsf.edu

In Progress.

Introduction

Complexes of cyclin-dependent kinases (CDKs) and their cyclin regulatory subunits phosphorylate hundreds of protein substrates to drive progression through the phases of the cell division cycle^{99–103}. Phosphorylation generally occurs at serines or threonines followed by a proline, sometimes followed by a basic residue to form the optimal consensus site, S/T*-P-x-K/R. Multiple CDK sites are often clustered in long regions of intrinsic disorder¹⁰⁰. Phosphorylation in these regions promotes or inhibits interactions with other proteins to trigger changes in the activity, binding affinity, localization, or turnover of the regulatory and structural proteins that govern cell cycle events^{104–107}.

CDK substrates are phosphorylated in a specific order, ensuring the correct sequence and coordination of cell cycle events. The timing of substrate phosphorylation depends on many mechanisms. Due to variations in sequence context and accessibility, different CDK sites exhibit wide variations in their rates of phosphorylation, likely resulting in differences in the timing of phosphorylation. Many substrates carry short linear sequence motifs (SLiMs) that interact with docking sites on a specific cyclin regulatory subunit, thereby promoting phosphorylation at cell cycle stages when that cyclin is expressed^{101,108,109}. For example, an L-x-F motif on some substrates docks at a site called the hydrophobic patch of Cyclin B^{110–113}. There is also abundant evidence that the timing of substrate phosphorylation is determined in part by the level of CDK activity, such that certain substrates are modified earlier in the cycle at low CDK activity and other substrates are modified later by rising levels of activity^{105,106,114–117}. Phosphatase specificity for different sites is also likely to contribute to the timing of phosphorylation^{118–127}.

CDK substrate interactions can be affected by the accessory protein Cks1, which binds to the CDK subunit of the Cyclin-CDK complex^{128–131}. Cks1 has a phosphate-binding pocket with specificity for phosphorylated threonine. After initial phosphorylation of a CDK substrate at a

threonine, Cks1 binds to the phosphothreonine to promote secondary phosphorylation of the substrate at downstream serines or threonines, leading to sequential multi-site phosphorylation¹⁰⁵. Cks1 is required for multi-site phosphorylation of numerous CDK substrates. In the case of the CDK inhibitor Sic1, Cks1 promotes secondary phosphorylation at 'phosphodegron' motifs that trigger Sic1 ubiquitylation and destruction¹⁰⁶. Cks1-dependent secondary site phosphorylation provides a mechanism to delay the timing of cell cycle events until CDK activity reaches a higher threshold.

Recent structural studies revealed that human Cyclin B1 carries a binding pocket for phosphorylated substrates¹³¹. This "phospho-pocket (PP)" is formed by the positively-charged side chains of three amino acids, R307, H320 and K324, on the surface of Cyclin B1 near the Cdk1 active site. These residues are highly conserved in B-type Cyclins (**Fig 2.1**), supporting a conserved role for phosphate binding at this site. The discovery of this phosphate-binding site raised the possibility that Cyclin B, like Cks1, interacts with phosphorylation sites on Cdk1 substrates to promote secondary phosphorylation at other sites.

We recently showed that mutation of the PP in budding yeast Clb2 reduces phosphorylation of Ndd1, a transcriptional co-activator that stimulates *CLB2* expression in early mitosis¹⁰⁵. Ndd1 has 16 consensus CDK phosphorylation sites. Initial phosphorylation of one site, T319, promotes Ndd1 function and *CLB2* expression in early mitosis, resulting in positive feedback¹³². During M-phase with high CDK activity, hyperphosphorylation at multiple additional sites promotes Ndd1 degradation, thereby suppressing *CLB2* expression in a mitotic arrest. *In vitro*, large numbers of sites are phosphorylated by wild-type Clb2-Cdk1-Cks1 complexes. Mutation of either Cks1 or the Clb2 PP does not affect initial phosphorylation sites but reduces phosphorylation at later sites, suggesting that the Cyclin PP, together with Cks1, is required for secondary phosphorylation at sites that promote Ndd1 degradation.

In budding yeast, four B-type cyclins (Clb1-4) contribute to the control of mitosis¹⁰⁷. Clb2 is the major mitotic cyclin, working with Cdk1 to catalyze phosphorylation of numerous proteins involved in mitotic processes, including spindle assembly and bud growth and morphology¹³³⁻¹³⁵. It is also involved in the phosphorylation, and thus activation, of the Anaphase-Promoting Complex/Cyclosome (APC/C), the ubiquitin ligase responsible for triggering chromosome segregation in anaphase^{136,137}. Deletion of *CLB2* is not lethal but causes an elongated bud morphology and mitotic delays. *CLB2* is essential for survival in the absence of *CLB1* and *CLB3*¹³⁵.

As multi-site phosphorylation of CDK substrates plays an important role in cell cycle regulation, we asked whether mutation of the PP in Clb2 leads to cell cycle defects. Our results suggest that mutation of the PP in Clb2 is not lethal but causes a delay in mitotic timing, particularly when combined with deletions of *CLB1* and *CLB3*. We conclude that the precise timing of mitotic events depends in part on PP-dependent hyperphosphorylation of Clb2-Cdk1 substrates in the cell.

Results

The Clb2 phosphate pocket is required for normal cell proliferation

To characterize the functions and biochemical properties of the phosphate pocket in B-type cyclins, we analyzed the role of the pocket in a model organism, the budding yeast *Saccharomyces cerevisiae*. The three basic residues that constitute the phosphate-binding pocket of human Cyclin B1 are highly conserved not only among paralogs but also orthologs from different species (**Fig 2.1**). The six B-type cyclins of *S. cerevisiae* (Clb1-6) all contain the three basic residues that form the pocket. Due to its high conservation, we hypothesized that the phosphate-binding pocket plays an important role in B-type cyclin function.

Four B-type cyclins (Clb1-4) are involved in the control of mitosis in budding yeast. Clb2 is the major mitotic regulator, and mutations in *CLB2* cause the most severe defect in morphology as well as proliferation. We therefore focused our studies on the phosphate pocket of Clb2. As in our previous work, we constructed a strain in which *CLB2* is replaced by a mutant gene in which the three key pocket residues are mutated to alanine – termed the *clb2-pp* mutant (R366A, R379A, K383A)¹⁰⁵.

Mutation of the Clb2 phosphate pocket did not cause an elongated morphology phenotype like that seen in a $\Delta clb2$ strain^{135,138} (**Fig 2.2A**). To examine whether other *CLB* genes can compensate for the loss of the Clb2 PP, we introduced single or multiple deletion mutations in a *clb2-pp* background. In previous work, combinations of *CLB* deletions with $\Delta clb2$ (*i.e.* $\Delta clb1 \Delta clb2$, $\Delta clb2 \Delta clb3$, $\Delta clb1 \Delta clb2 \Delta clb3$, $\Delta clb1 \Delta clb2 \Delta clb4$, and $\Delta clb1 \Delta clb2 \Delta clb3 \Delta clb4$) caused severe growth defects or lethality^{135,138}. We found, however, that combining deletions with *clb2-pp* resulted in viable colonies ($\Delta clb1 clb2-pp$, *clb2-pp* $\Delta clb3$, $\Delta clb1 clb2-pp \Delta clb3$). Analysis by microscopy revealed that *clb2-pp* $\Delta clb3$ cells showed a mild elongated morphology, while $\Delta clb1$

clb2-pp and $\Delta clb1 clb2-pp \Delta clb3$ cells displayed a more pronounced elongated phenotype accompanied by cell chains (**Fig 2.2A**).

To further assess the effects of the *clb2-pp* mutation on cell cycle progression, we measured growth rate in suspension cultures using an optical density-based method (**Fig 2.2B**). At 30°C in rich media, all single and double mutants grew at rates that were not significantly different from that of the wild-type strain. A defect was seen only in the triple mutant, $\Delta clb1 clb2-pp \Delta clb3$, which grew at a rate about 40% lower than that of the wild-type (**Fig 2.2C, Right**). We also measured the growth of all mutants on plates (**Fig 2.2C**). On rich media, the $\Delta clb1 clb2-pp \Delta clb3$ mutant exhibited a mild growth defect at 30°C (**Fig 2.2C, Left**). Thus, in the absence of *CLB1* and *CLB3*, *clb2-pp* is not sufficient for normal rates of proliferation.

To further examine the role of the Clb2 PP, we sensitized the strains with heat stress or microtubule destabilization. Only the $\Delta clb1 clb2-pp \Delta clb3$ mutant showed a significant growth defect at 37°C (**Fig 2.2C, Middle**). Any double or triple mutant showed a growth defect when treated with benomyl, a microtubule destabilizer (**Fig 2.2C, Right**), suggesting a role for the Clb2 PP in the control of anaphase.

The Clb2 phosphate pocket is required for normal mitotic progression

We next investigated the role of the Clb2 PP in progression through mitosis. As in our previous work, we measured mitotic progression in single cells by analyzing the behavior of a fluorescently-tagged spindle pole body (SPB)¹³⁹. The SPB is duplicated in early S phase and then separates slightly at the onset of mitosis to form the short mitotic spindle; the initiation of anaphase then triggers rapid SPB separation as the spindle elongates across the mother cell

and into the bud^{140,141}. The time between initial SPB separation and spindle elongation reflects the time from mitotic entry to anaphase onset.

We constructed wild-type and *clb2-pp* strains in which the SPB protein Spc42 was fused to a C-terminal mCherry fluorophore, and we measured the time from SPB separation to spindle elongation (**Fig 2.3A**). As in our previous studies, this time was highly variable in wild-type cells, ranging from 10 to 66 min with a median of 32 min (**Fig 2.3B**)¹³⁹. In comparison, *clb2-pp* mutant cells displayed a range of 20 to 82 min, with a median of 48 min. Thus, *clb2-pp* cells experience a ~15-minute delay in a ~30-minute process (**Fig 2.3B**). Thus, the Clb2 PP is required for the normal progression of cells through early mitosis, and/or is required for the normal timing of anaphase onset.

We next analyzed mitotic progression by western blotting of mitotic proteins in cells released from a pheromone-induced G1 arrest. We first analyzed the separase inhibitor securin/Pds1, which is known to increase in abundance in S phase and then decline rapidly at the onset of anaphase due to its ubiquitination by the Cdc20-activated APC/C. Mutation of the Clb2 PP resulted in a small but reproducible delay of 10-20 min in the timing of securin destruction (**Fig 2.3C, Left**). Deletion of *CLB1* and *CLB3* had no significant impact on securin degradation, but $\Delta clb1 clb2-pp \Delta clb3$ cells showed a major delay in securin degradation past 120 min after release from G1 (**Fig 2.3C, Right**).

We also monitored the degradation timing of Ndd1, a transcriptional co-activator that is targeted by the Cdh1-activated form of the APC/C, resulting in late mitotic degradation¹⁴². As in the case of securin, late mitotic degradation of Ndd1 was delayed by 10-20 minutes in the *clb2-pp* strain, and more severely delayed in $\Delta clb1 clb2-pp \Delta clb3$ cells (**Fig 2.3D**).

To test if the *clb2-pp* anaphase delay is caused by activation of the spindle assembly checkpoint (SAC), we also analyzed securin levels in a *clb2-pp* strain lacking Mad2, a critical SAC component¹⁴³⁻¹⁴⁵. Relative to $\Delta mad2$ cells, *clb2-pp* $\Delta mad2$ cells displayed the same minor delay in securin destruction that we observed in *clb2-pp* cells, suggesting that this delay does not depend on the SAC.

Phosphorylation of several proteins *in vivo* depends on the Clb2 phosphate pocket

We hypothesized that mitotic defects in *clb2-pp* cells are due to defects in Cdk1 substrate phosphorylation. We tested this possibility by quantitative mass spectrometry of protein phosphorylation in wild-type and *clb2-pp* cells, using Stable Isotope Labeling with Amino acids in Cell culture (SILAC)¹⁴⁶. Wild-type and *clb2-pp* cultures were labeled differentially with “light” or “heavy” isotopes, and proteins were isolated from cell lysates and trypsinized. Phosphorylated peptides were enriched with Immobilized Metal Chelate Affinity Chromatography (IMAC) before analysis by Liquid Chromatography – Tandem Mass Spectrometry¹⁴⁷. We obtained 4000 phosphopeptide sequences, of which 680 were phosphorylated at a Cdk1 consensus sequence ([S/T]P) (**Fig 2.4**). The relative quantities of these peptides in wild-type and *clb2-pp* cells were determined, revealing 70 phosphopeptides with 2-fold or greater enrichment in the wild-type culture and 37 phosphopeptides enriched in the *clb2-pp* culture. We were particularly interested in phosphopeptides enriched in the wild-type cells, which represent sites that are less phosphorylated in the *clb2-pp* cells, as expected for Cdk1 substrates that depend on the Clb2 PP for full phosphorylation.

Many of the potential Clb2 PP target proteins contain more than one CDK consensus sequence, and several of these proteins were identified among the large numbers of putative Cdk1 substrates identified in our previous studies^{99,100} (**Table S2.1**). Noteworthy proteins from this list

are Fun30 (chromatin remodeling), Jsn1 (mRNA-binding protein), and Ssk1 (MAP kinase cascade component), which are highlighted in **Fig 2.4A**. These proteins contain multiple Cdk1 consensus sites in large regions of predicted disorder, making them good candidates for PP-dependent secondary phosphorylation (**Fig S2.1**).

We analyzed the PP-dependent proteins by Gene Ontology(GO) term enrichment. GO analysis of the 70 PP-dependent peptides showed that the *clb2-pp* mutation affected proteins that are primarily related to two biological processes (BP): chromatin remodeling and positive regulation of DNA-templated transcription (**Fig S2.2**).

Phosphorylation of Fun30 and Ssk1 *in vitro* depends on the Clb2 phosphate pocket

Two of the top PP-dependent candidates, Fun30 and Ssk1, contain 10 and 18 [S/T]P sites, respectively, including three optimal sites with a basic residue at the +3 position (**Fig S2.1**). To test the impact of the Clb2 PP on phosphorylation of these proteins *in vitro*, we measured phosphorylation of a Fun30 fragment (aa 1-550) or full-length Ssk1 (712 aa) with purified Cdk1-Clb2-Cks1 complexes (**Fig 2.5**). Phosphorylation of both proteins was reduced in the absence of either the Clb2 or Cks1 phospho-pocket, indicating that the PP of Clb2 is required for hyperphosphorylation of some CDK substrates.

Discussion

Our results shed light on the biological function of the highly conserved phosphate-binding pocket (PP) of mitotic B-type cyclins. We found that mutation of the PP in budding yeast Clb2 had little impact on cell morphology or proliferation rate under normal conditions, but detailed analyses uncovered defects in mitotic progression and particularly in the timing of anaphase onset. More pronounced defects in morphology, growth, and mitosis were observed when the *clb2-pp* mutation was combined with deletions of the two other major mitotic cyclin genes, *CLB1* and *CLB3*. We conclude that the PP is required for normal mitotic progression and potentially for other Clb2 functions, and that other cyclins provide some of these functions in the absence of the Clb2 PP.

The *clb2-pp* mutation, when combined with deletions of *CLB1* and *CLB3*, causes an elongated morphology that resembles the well-known bud morphology defect of $\Delta clb2$ cells, in which there is a delay in the switch from polar to isotropic bud growth^{133,135,138}. Our results suggest that PP-dependent Clb2-Cdk1 substrates function in this switch. For example, Clb2-Cdk1 is thought to phosphorylate components of the polarisome, a protein complex that controls actin dynamics and polarized bud growth¹⁴⁸. Potential Clb2-Cdk1 substrates in this complex include Spa2 and Bud6, both of which are extensively phosphorylated on multiple Cdk1 consensus sites and other sites^{100,148}. PP-dependent multisite phosphorylation of these substrates might be required for the regulation of their functions.

Our evidence that the Clb2 PP is required for timely anaphase onset is consistent with abundant previous evidence that Cdk1 and mitotic cyclins play important roles in the metaphase-anaphase transition. Delays in anaphase onset are seen in cells carrying defects in Cdk1 activity or cyclin expression, including cells lacking *CLB2*^{136,137,149–151}. Interestingly, the *clb2-IV* mutant (D232G, L286S, K353R, and D485G), a temperature-sensitive allele has a delayed

securin degradation without Clb1, resembling our *clb2-pp* allele¹⁵⁰. In principle, Clb2-dependent mitotic delays might be expected to result from defects in early mitotic processes such as spindle assembly, which would delay anaphase by activation of the SAC^{143–145}. However, our data suggest that the anaphase delay of the *clb2-pp* mutant is independent of the SAC: we observed that deletion of *MAD2* did not abolish the mitotic delay. Our results imply that PP-dependent phosphorylation plays a direct role in anaphase initiation.

The most likely explanation for our results is that the PP is required for the phosphorylation, and thus activation, of the mitotic APC/C. Cdk1-dependent phosphorylation of multiple APC/C subunits is known to promote APC/C binding to the activator subunit Cdc20, thereby initiating the ubiquitination and destruction of securin and mitotic cyclins^{136,137,152–155}. APC/C activation depends on multisite phosphorylation of large disordered loops in conserved TPR subunits (Cdc27/Apc3, Cdc16/Apc6, and Cdc23/Apc8 in budding yeast). Interestingly, the Cks1 subunit is important for Cdc16 and Cdc27 hyperphosphorylation in yeast, and APC/C activation depends on Cks1-mediated APC/C hyperphosphorylation in vertebrates¹³⁶. Cks1-dependent binding of CDK to TPR subunit loops is thought to promote secondary phosphorylation on Loop 300 in the large Apc1 subunit, leading to the formation of a binding site for Cdc20¹⁵³. The critical role of Cks1 in APC/C activation raises the possibility that the Clb2 PP also promotes the multisite phosphorylation events that underly activation of the APC/C. We propose that PP-dependent phosphorylation by Clb2-Cdk is important for APC/C activation.

Based on our phosphoproteomic studies and on the large number of Cdk1 substrates carrying multiple clustered phosphorylation sites, we suspect that the *clb2-pp* phenotype is likely to be complex and arise from changes in the phosphorylation state of many proteins. Further research will be required to identify these additional targets and explore the molecular mechanisms underlying Clb2 PP-mediated cell cycle regulation. Ultimately, the phospho-pocket

in Clb2 likely serves as an alternate mechanism for secondary phosphorylation on CDK substrates, similar to Cks1. The phospho-pockets of B-type cyclins and Cks1 are highly conserved. This stepwise phosphorylation mechanism likely plays an important role in cell-cycle, especially in temporal regulation^{105,115,156}. Secondary phosphorylation when CDK activity reaches a high threshold at M-phase may alter a variety of protein activities, helping to ensure the precise timing of cell cycle events.

Methods

Strain and Plasmid Construction

All strains are derivatives of W303a, except that strains used for SILAC are derivatives of S288c (**Table 2.1**). All strains were constructed using PCR- and/or restriction digest-based homologous recombination with 50-bp flanking homology. All plasmids were constructed using Gibson Assembly to recombine restriction-digested vector with PCR products or synthetic DNA fragments (Integrated DNA Technologies, IDT) (**Table 2.2**).

Yeast Proliferation

Yeast strains were grown in YPD (1% Yeast Extract, 2% Peptone, 2% Dextrose) at 30°C unless specified otherwise. The optical density-based growth assay was carried out using a TECAN Spark 10M plate reader. 200 μ l of OD₆₀₀=0.05 culture was added to the wells of a transparent, sterile, flatbottom, non-tissue culture treated 96-well plate (Falcon #351172), which was then sealed with Breathe-Easy sealing membrane (Diversified Biotech #BEM-1). Absorbance (OD₆₀₀) of each well was measured every 15 min for 24 h during a 30°C incubation with shaking. Four replicates of each strain were analyzed. Growth rate was quantified by fitting absorbance data to a Logistic Growth Model on Prism Graphpad. For analysis of growth on YPD plates, 5 μ l aliquots of 1:10 serial diluted culture were spotted and incubated at 30 or 37°C.

Microscopy

Differential interference contrast (DIC) imaging was performed with a Nikon Ti2-E microscope and a CFI Plan Apochromat Lambda 100X/1.45 NA oil immersion objective lens. Images were captured with a Teledyne Photometrics Prime 95B 25 mm camera. Nikon NIS Elements software was used to drive stage movement and acquisition.

Live imaging of yeast cells with mCherry-tagged Spc42 was conducted as described¹³⁹. Imaging was performed using a Nikon Ti-E microscope equipped with a Yokogawa CSU-22 spinning disk confocal unit and a Teledyne Photometrics Evolve EMCCD camera (UCSF Center for Advanced Light Microscopy). Imaging sessions typically lasted for 1.5 h with a time interval of 2 min between frames. For each time point and channel, z-stacks were acquired across a distance of 5 μm with 0.5 μm steps. The exposure time for the mCherry channel was set to be less than 40 ms for each z-slice. The imaging system was controlled using $\mu\text{Manager}$ software¹⁵⁷, ensuring precise and accurate acquisition of the images.

Yeast cells were grown and imaged at 30°C. Before imaging, yeast were grown in synthetic complete media with 2% glucose (SD) for 24 h with dilution to maintain $\text{OD}_{600} < 0.4$. For imaging, wells in a 96-well Glass Bottom Microwell Plate (MGB096-1-2-LG-L) were pre-treated with 10 mg/ml Concanavalin A for 1 h and washed with water. 100 μl cell culture was added and immobilized for 40–60 min in a 30°C incubator. Unattached cells were washed off with fresh media before imaging. To minimize autofluorescence, all media was filtered instead of autoclaved.

SILAC Mass Spectrometry

SD-Arg-Lys media is made with a premix CSM-Arg-Lys drop out powder (Sunrise Science Product). To make a 1000x stock solution of lysine and arginine (30 mg/ml lysine, 20 mg/ml arginine), L-lysine-HCl (Sigma #L5626) and L-arginine-HCl (Sigma #A5131) are dissolved in water and the solution is filter-sterilized using a 0.2 μm filter. The heavy arginine and lysine amino acids contain stable heavy isotopes of both ¹³C and ¹⁵N: L-lysine:2HCl (Cambridge Isotope #CNLM-291-H) and L-arginine:HCl (Cambridge isotope # CNLM-539-H). Both light and heavy amino acid stocks are stored in the dark at room temperature.

Wild-type and *clb2-pp* strains were grown in 2-liter SD+2%Dextrose media +2 mL of heavy or light amino acid stock each to $OD_{600} = 0.5$. Harvested cells were washed, resuspended into lysis buffer (100 mM Tris-HCl pH 8.0, 2% SDS) and snap frozen as “popcorn” by dropwise freezing of the cell suspension in LN₂. Frozen cell suspensions were lysed using a Cryomill (SPEX SamplePrep 6870). The frozen milled powder was quickly heated to 60°C and incubated for 30min, followed by centrifugation at 15000g for 10 min to separate the cell debris. Lysate was reduced by incubating with 10mM DTT at 60C for 30 min, then alkylated by incubating with 30mM Iodoacetate at room temperature for 30 min in the dark to cap free cysteine residues. The total proteins are then precipitated using Ethanol/Acetone; the pellet is washed three times with 40%Ethanol/40%Acetone, then kept frozen at -20°C before solubilization and trypsin digestion.

Solubilization of protein pellets was performed in 20 mL of 8 M urea in 50 mM Tris-HCl pH 8.0 with a dounce homogenizer and centrifuged at 4000x g for 10 min to remove insoluble debris. Protein concentration was measured using the Bradford method (Bio-Rad #5000006) and monitoring absorbance at 590 nm. Protein extracts were diluted 5-fold with 50 mM Tris-HCl and digested for 12 hours at 37°C using 1/100th sequencing grade trypsin (Promega cat#: V511A) by weight compared to the total amount of protein as measured by the Bradford method.

Tryptic digests were acidified to a final concentration of 0.5% Trifluoroacetic acid (TFA) and centrifuged at 4000 g to remove insoluble peptides. Solid phase extraction was performed using a 5 g Sep-Pak C18 column (Waters #WAT036925) to remove salts. SPE was performed as follows: SPE columns were pre-washed with 1 column volume (20 mL) of methanol, followed by 1 column volume of 80% acetonitrile: 0.1% TFA, and equilibrated using 2 column volumes of 0.1% TFA. Tryptic digests were loaded by gravity flow and washed with two column volumes of

0.1% acetic acid. Peptides are eluted using 1.5 column volumes of 80% acetonitrile, 0.1% acetic acid, and dried under centrifugation and vacuum.

The method for purifying phosphopeptides using Fe³⁺- nitrilotriacetic acid immobilized metal affinity chromatography (IMAC) silica resin is adapted from Suhandynata et al. (2014). The dried peptides are resuspended in 0.6% acetic acid (10 µg/µl peptide concentration) and spun for 5 min at 2300x g in a microcentrifuge. The supernatant is loaded onto a microcapillary column with fiber glass as a frit containing freshly prepared IMAC resin and washed twice with 60 µl of wash buffer containing 25% acetonitrile, 100 mM NaCl, and 0.1% acetic acid, once with 60 µL 0.1% acetic acid, and finally once with 30 µl water. Loading and washing is performed using positive displacement using a syringe at a flow rate of 1 to 2 µl/min. Phosphopeptides are eluted into a glass insert using 180 µl 6% NH₄OH and dried under vacuum. The dried phosphopeptides can be stored at -20°C until ready for MS.

Phosphopeptides were directly analyzed following reconstitution in 0.6% acetic by autosampler injection onto a liquid chromatography system coupled to a high resolution mass spectrometer (Thermo Scientific; Ultimate 3000 RSLCnano, Orbitrap Fusion Lumos) operated in data dependent mode. Data analysis was performed using the COMET database search tool that is part of the Trans Proteomic Pipeline (TPP) software suite. The search results were then processed and quantified using the XPRESS component of TPP to generate SILAC ratios of the identified phosphorylated peptides. An FDR of less than 1% was applied for the identified phosphopeptides, combined with manual interrogation of MS/MS spectra and parent ion chromatograms as a final quality control for identification and quantification; respectively.

GO Analysis

We utilized ShinyGO to analyze and visualize Gene Ontology (GO) data¹⁵⁸. Enrichment analysis was done using the Biological Processes (BP), Cellular Component (CC) and Molecular Function (MF) pathway databases. Statistical significance of enriched terms was determined by p-values and adjusted p-values.

Protein Purification

Wild-type and *clb2-pp* Cdc28-Clb2 complexes were purified as described^{99,159}. Briefly, TAP-tagged *CLB2* was overexpressed from a 2-micron *URA3* plasmid under *GAL* control. Yeast were grown in SD-Ura + 2% Raffinose at 30°C with shaking to OD₆₀₀=0.6, followed by induction with 2% Galactose for 2 h. Cells were harvested, washed with PBS, and resuspend into 10 ml of TAP Lysis Buffer (25 mM HEPES pH 8.0, 1 M NaCl, 0.1% NP-40, 1 mM EDTA, 30 mM EGTA, 1 mM PMSF, 1 cOmplete Protease Inhibitor Tablet, 80 mM beta-glycerophosphate, 50 mM NaF, 1 mM Na₃VO₄). Cells were frozen in LN2 and stored at -80°C until use. Frozen cells were processed in a Cryomill (SPEX SamplePrep 6870) for 8 cycles of 2-min grinding followed by 2-min chilling. Lysate was clarified by two centrifugations at 10,000x g then 50,000x g, and bound to IgG Sepharose 6 Fast Flow beads (GE 52-2083-00 AH) for 1 h at 4°C. The column was washed 3 times with 10 bed volumes of TAP Lysis Buffer, then 1 volume of TEV Cleavage Buffer (10 mM Tris-HCl pH 8.0, 150 mM NaCl, 0.1% NP-40, 0.5 mM EDTA, 1 mM DTT). Cdc28-Clb2 complexes were cleaved off the column with AcTEV (Invitrogen Cat#12575015) in 1 ml TEV Cleavage Buffer for 90 min at 16°C. Eluate was collected by passing an additional 400 µl of TEV Cleavage Buffer over the column. AcTEV was removed by incubation with Ni-NTA beads (QIAGEN #30230) for 1 h at 16°C. The eluate was concentrated in centrifugal concentrators (Millipore Sigma #UFC803024) and stored in 10% Glycerol at -80°C.

Purification of recombinant wild-type and mutant *S. cerevisiae* Cks1 was performed as described¹²⁸. Briefly, BL21(DE3) Star cells transformed with a plasmid expressing *CKS1* from

the T7 promoter were grown in 1 liter of LB + Amp at 37°C to an OD₆₀₀ of 0.6, then induced with 1 mM of IPTG at 16°C overnight. Cells were frozen in LN2, thawed, and sonicated in 10 ml PBS. The lysate was clarified by centrifugation at 7000 rpm. The supernatant was incubated in a boiling water bath for 5 min and then centrifuged for 10 min at 40,000 rpm (Beckman Ti45 rotor). The supernatant was supplemented with ammonium sulfate (1 g per 6.1 ml of supernatant), incubated for 30 min at 4°C, and centrifuged at 40,000 rpm for 10 min (Beckman Ti45 rotor). Precipitated proteins were redissolved in 10 ml Tris-NaCl-EDTA Buffer (50 mM Tris pH 7.5, 100 mM NaCl, 2 mM EDTA) and dialyzed against three changes of Tris-NaCl Buffer (50 mM Tris pH 7.5, 100 mM NaCl). The dialysate was subjected to gel filtration on a S200 column, and fractions containing Cks1 were pooled and concentrated in a 15-ml Millipore centrifugal concentrator (nominal molecular mass cutoff = 10 kDa).

For production of CDK substrates, a codon-optimized synthetic DNA (IDT) was inserted into a pET28 expression vector by Gibson assembly, fused to DNA encoding an N-terminal 6xHis-SUMO tag. BL21(DE3) Star cells transformed with plasmids expressing recombinant protein from the T7 promoter were grown in 1 liter of LB + Kan at 37°C to an OD₆₀₀ of 0.6, then induced with 1 mM of IPTG at 16°C overnight. Cells were frozen in LN2, thawed and resuspended in Native His Lysis Buffer (50 mM Tris pH 7.5, 300 mM NaCl, 20 mM Imidazole, 3 mM DTT, 5% Glycerol) supplemented with 250U of Benzonase, 1 cComplete Protease Inhibitor Tablet, 500 µg/ml Lysozyme and 1 mM PMSF). Suspended cells were sonicated and clarified by centrifugation at 40,000 x g for 30 min. Supernatant was incubated with Ni-NTA beads (QIAGEN #30230) for 1 h at 16°C. The beads were washed 3 times with 10 bed volumes of Native His Lysis Buffer, and eluted with 4ml Elution Buffer (Native His Lysis Buffer with 200 mM Imidazole). Eluate was concentrated and snap frozen.

Kinase Assays

Phosphorylation reactions were conducted in a reaction buffer containing 25 mM HEPES pH 7.5, 50 mM NaCl, 10 mM MgCl₂, 1 mM DTT, 100 μM ATP, and supplemented with 0.025 μCi [γ-³²P]-ATP (Hartmann Analytic). To quench the reactions at specific time points (5, 15, 30, and 60 min), an aliquot of the reaction mixture was pipetted into SDS-PAGE sample buffer. Reaction products were separated on Phos-tag SDS-PAGE with a gel composition of 7.5% acrylamide and 50 μM Phos-tag (Wako Chemicals). Autoradiography was performed with an Amersham Typhoon 5 Biomolecular Imager (GE Healthcare Life Sciences), and images were quantified using ImageQuant TL software (Amersham Biosciences).

Western Blotting

Yeast strains expressed C-terminally Myc-tagged proteins either at the endogenous locus or under the control of the *GAL* promoter. For *GAL*-induced *NDD1* expression, galactose was added to a final concentration of 2% in YEP-Raffinose medium. G1 arrest was achieved by addition of alpha factor (1.5 μg/ml) for 3 h at 30°C; G1 release was achieved by washing the arrested culture 3 times with fresh media. Samples (1 ml) were harvested at 20-min intervals over the course of 2 h. Alpha factor was added back to the culture 1 h after release, when most cells had budded. Yeast lysates were prepared by bead-beating cells for 2 min in 100 μl urea lysis buffer (20 mM Tris-HCl pH 7.4, 7 M urea, 2 M thiourea, 65 mM CHAPS, 10 mM DTT) with 100 μl of 0.5 mm diameter glass beads. SDS-PAGE was used to separate equal volumes of the lysates, which were then transferred onto a 0.45-micron nitrocellulose membrane (GE-Healthcare Life Sciences) at a constant voltage of 110V for 70 min at 4°C. Blots were incubated overnight at 4°C with primary antibodies: either mouse anti-Myc (9B11 Cell Signaling Technology) diluted 1:5000 in TBS-T containing 4% nonfat dry milk, or GAPDH Monoclonal Antibody (GA1R Thermo) diluted 1:2500 in TBS-T containing 4% nonfat dry milk. Blots were then incubated at room temperature for 1 h with secondary antibody IRDye 800CW Donkey

anti-Mouse IgG (926-32212 LI-COR), diluted 1:2000 in TBS-T. After each incubation, blots were washed three times over 15 min with TBS-T. Fluorescence signals on the blots were captured using an Odyssey Fc imager (LI-COR) at 800 nm for a duration of 10 min.

<i>Saccharomyces cerevisiae</i>	Clb1	346	RRISKADDYDIQSR	TLAK	363
	Clb2	366	RRISKADDYDIQSR	TLAK	383
	Clb3	306	RRISKADDYEHDT	RTLAK	323
	Clb4	345	RRISKADDYDFEP	RTLAK	362
	Clb5	303	RRISKADDYDPVNR	NIGK	320
	Clb6	261	RRISKADNYCIETR	NMAK	278
<i>Schizosaccharomyces pombe</i>	Cdc13	341	RRISKADFYDIQT	RTVAK	358
<i>Homo sapiens</i>	Ccnb1	307	RRASKIGEVDVEQ	HTLAK	324
	Ccnb2	271	RRASKAGEVDVEQ	HTLAK	288
	Ccnb3	1266	RRYARCIHTNMKT	LTLSR	1283
<i>Mus musculus</i>	Ccnb1	304	RRASKAGEVDVEQ	HTLAK	321
<i>Rattus norvegicus</i>	Ccnb1	297	RRASKAGEVDVEQ	HTLAK	314
<i>Gallus gallus</i>	Ccnb2	266	RRASKAGEADAEQ	HTLAK	283
<i>Drosophila melanogaster</i>	CycB	390	RRYSKAAGAEDEH	HHTMSK	407
<i>Danio rerio</i>	Ccnb1	273	RRASKIGDVTAEH	HHTLAK	290
<i>Xenopus tropicalis</i>	Ccnb1	273	RRFAKCAHATMET	LTLLAR	290
<i>Caenorhabditis elegans</i>	Ccnb3	250	RRFGRVCRVDMKT	LTMGR	267

Fig 2.1. The phosphate-binding pocket is conserved in B-type cyclins.

Alignment of the amino acid sequences of B-type cyclin homologs, with cyan indicating the three basic residues that constitute the phosphate-binding pocket.

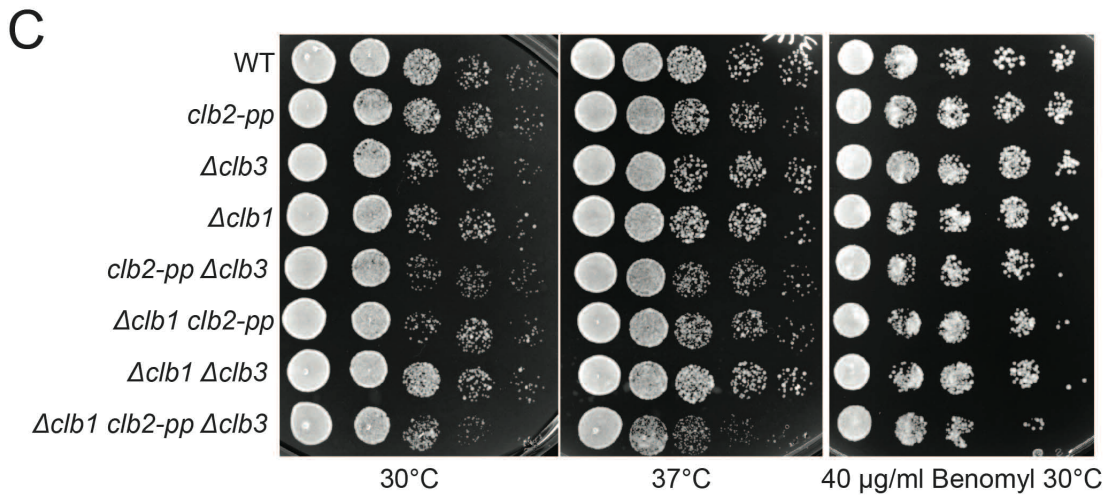
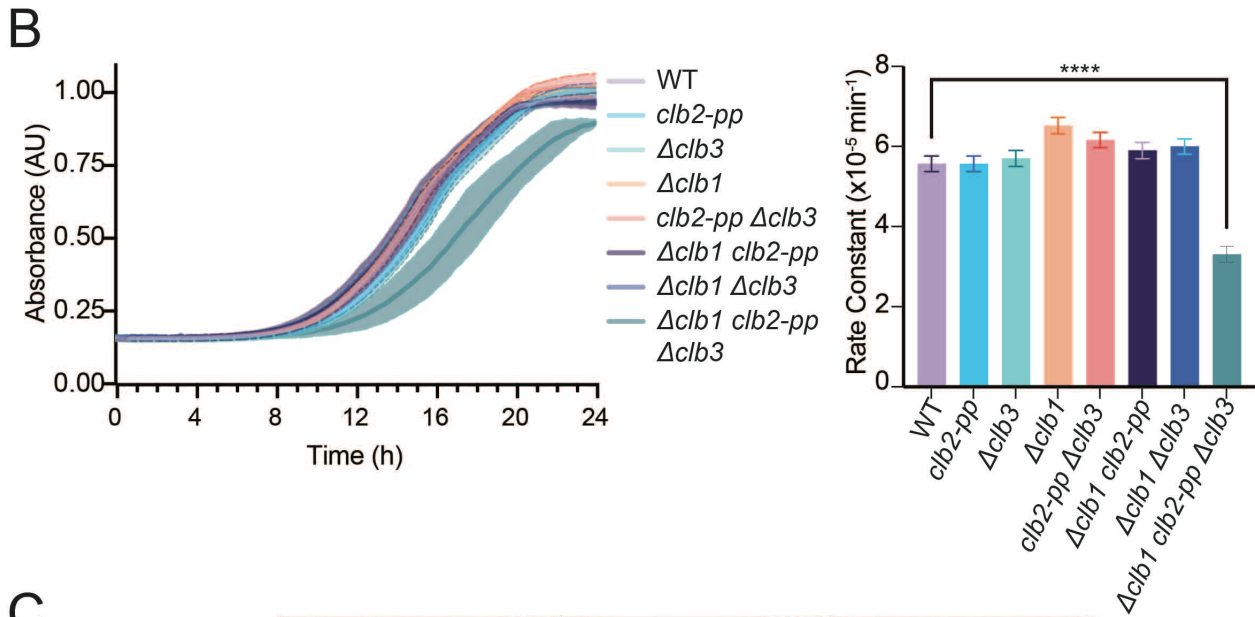
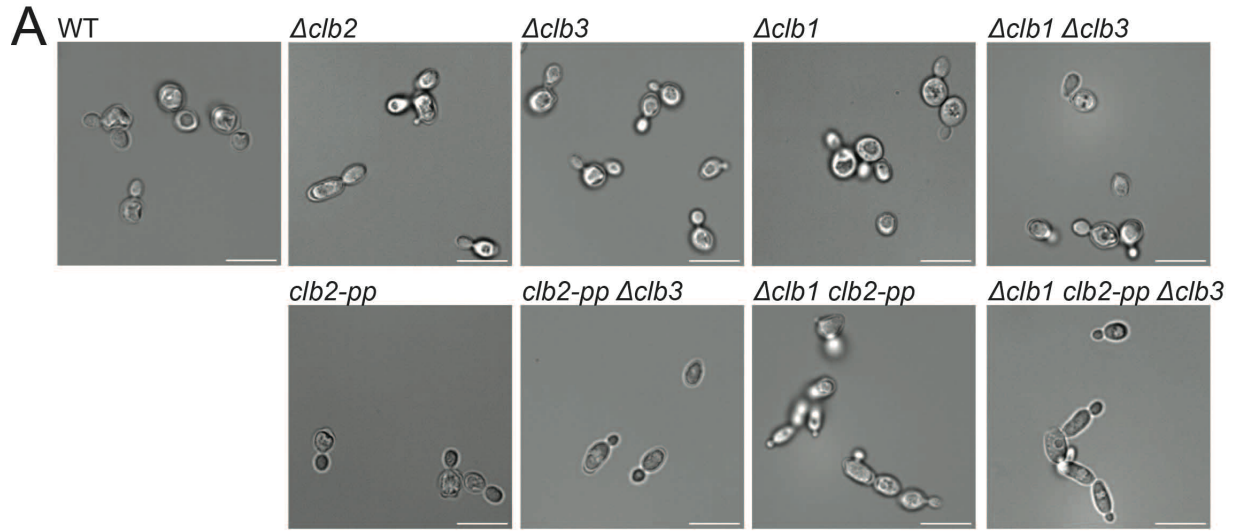


Fig 2.2. Mutation of the phosphate-binding pocket in Clb2 causes a growth defect in the absence of *CLB1* and *CLB3*.

- A. Representative differential interference contrast (DIC) microscopy images of the indicated yeast strains growing at mid-log phase in rich (YPD) media. Scale bar is 10 μm .
- B. (Left) Growth curves of the yeast strains in panel A over a 24-h period, with OD_{600} recorded every 15 min. The data represents the mean \pm standard deviation (SD) of four independent biological replicates. (Right) Bar graphs showing growth rates calculated by fitting the $\text{OD}_{600}/\text{min}$ to a logistic growth model. Data represents mean \pm SD of four independent biological replicates. Statistical significance was determined using one-way analysis of variance (ANOVA) (**** $p < 0.0001$).
- C. The yeast strains in panel A were spotted on YPD plates and incubated for 48 h at the indicated temperatures. Right panel shows growth on plates containing benomyl (40 $\mu\text{g}/\text{ml}$). Each spot represents 5 μl of a yeast culture at $\text{OD}_{600}=0.1$ followed by four 1:10 serial dilutions.

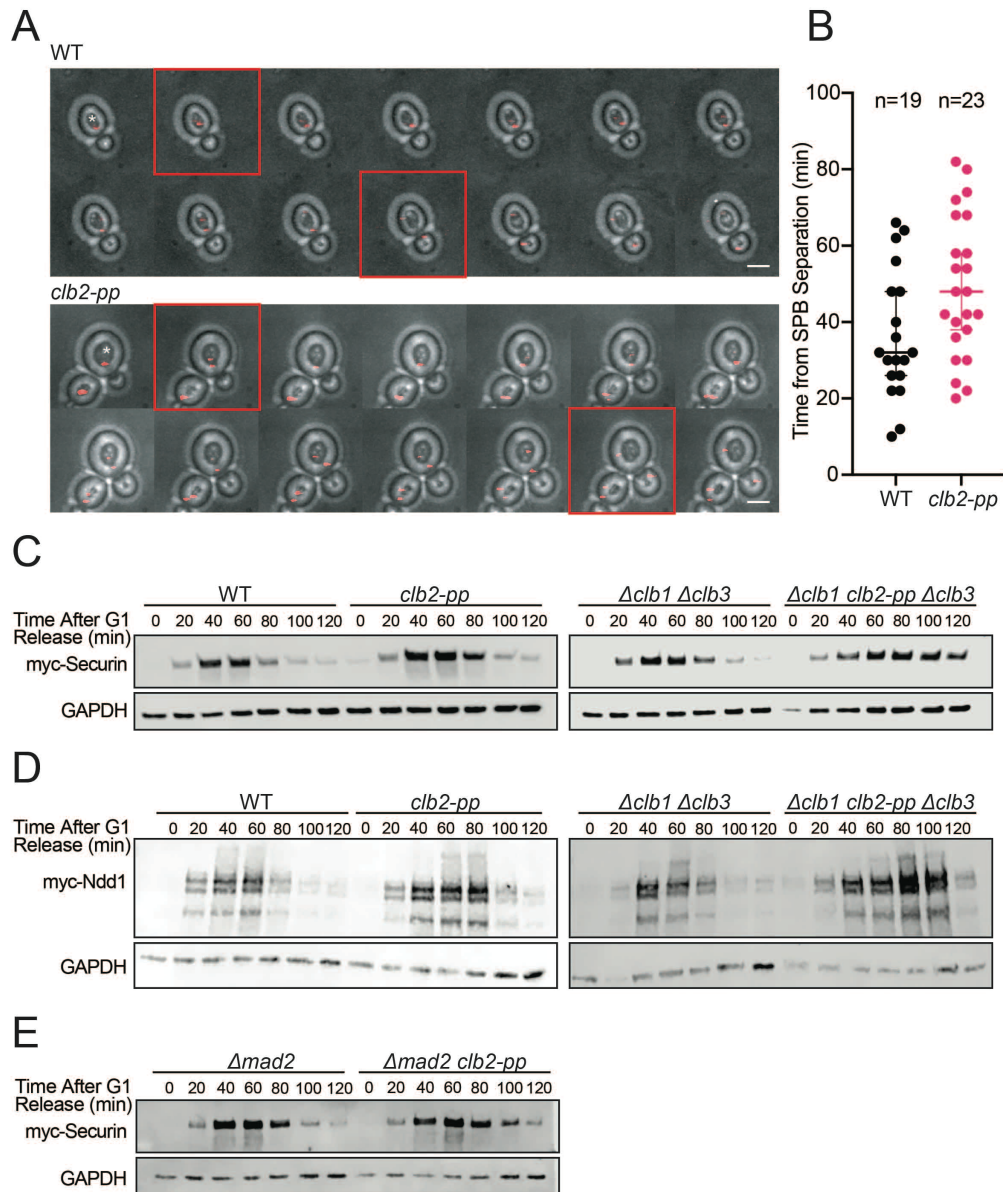


Fig 2.3. The *clb2-pp* mutation causes a mitotic delay.

- A. Representative fluorescence image montages of wild-type (WT) or *clb2-pp* yeast carrying mCherry-labeled Spc42, captured over 48 min at 2 min intervals. Images depict representative yeast cells with distinct mCherry foci (red). Frames indicated with red outlines depict (1) SPB separation and (2) initiation of spindle elongation. White asterisks mark the cells entering mitosis used for quantification. The scale bar represents 3 μ m.
- B. Scatter plot depicting single-cell measurements of time from SPB separation to spindle elongation, as in panel A. Each data point represents a single cell and the median \pm standard deviation (SD) is shown. The sample size (n) is noted above.
- C. Western blots comparing levels of Myc-tagged securin/Pds1 after release from a G1 arrest in the indicated yeast strains. GAPDH loading control on lower blot.
- D. Western blots comparing levels of Myc-tagged Ndd1 after release from a G1 arrest in the indicated yeast strains. GAPDH loading control on lower blot.
- E. Western blots of Myc-tagged securin/Pds1 after release from a G1 arrest in the indicated yeast strains. GAPDH loading control on lower blot.

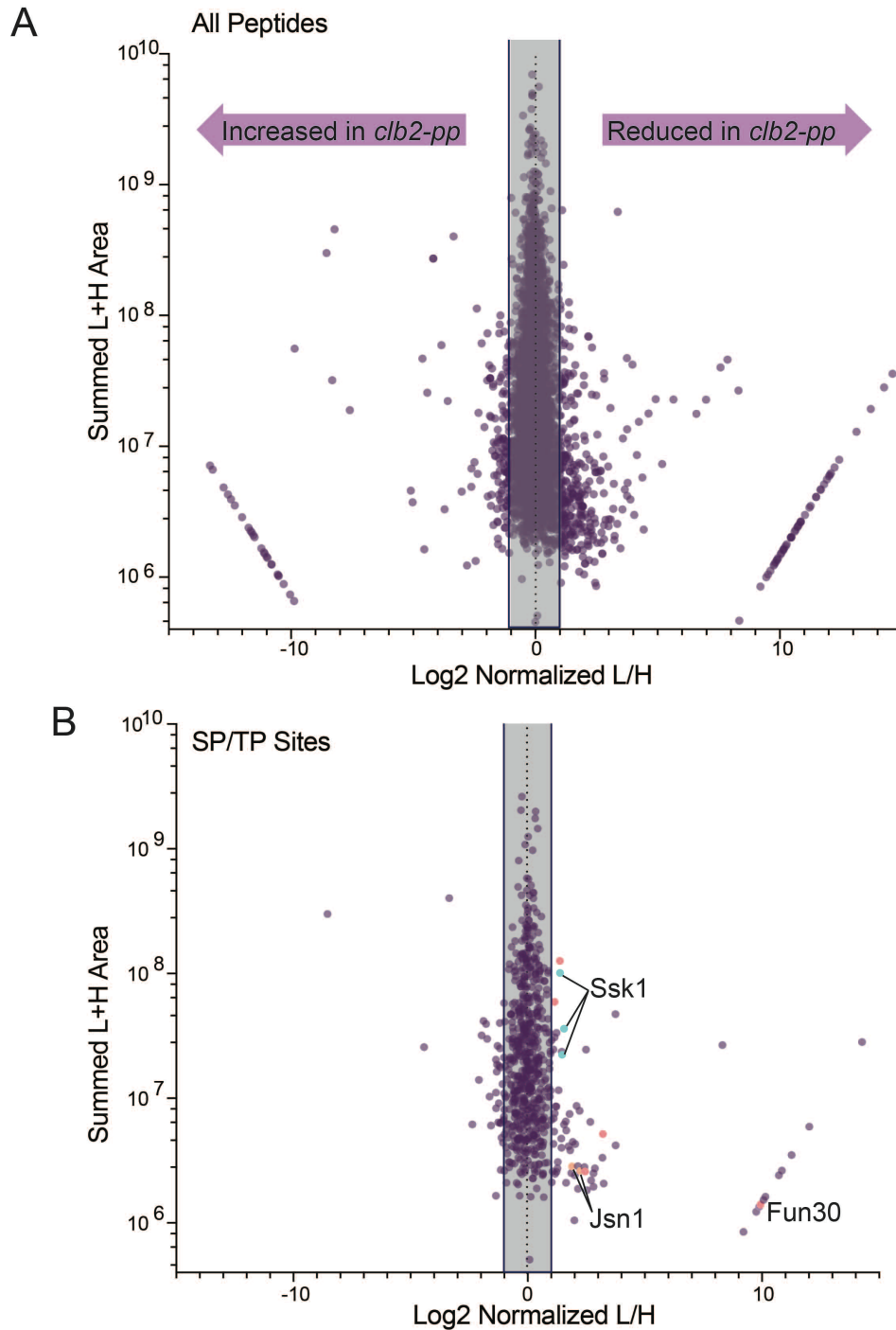


Fig 2.4. Identification of proteins with reduced phosphorylation in *clb2-pp* cells.

- A. Identification of IMAC-purified phosphopeptides in the SILAC-MS experiment comparing log-phase wild-type cells in 'light' media with *clb2-pp* cells in 'heavy' media. Each dot represents a single phosphopeptide, plotted according to its abundance (y-axis; summed area of heavy and light peaks) and the Log2 of the ratio of light:heavy peptide abundance (x-axis). Log2 L/H ratios above +1 represent phospho-peptides that were significantly reduced in *clb2-pp* cells, as expected for phosphorylation sites that depend on the Clb2 PP.
- B. Plot of the subset of phosphopeptides in which the identified phosphorylation site lies in a CDK consensus site (S/T*-P). Peptides from three putative CDK substrates are labeled.

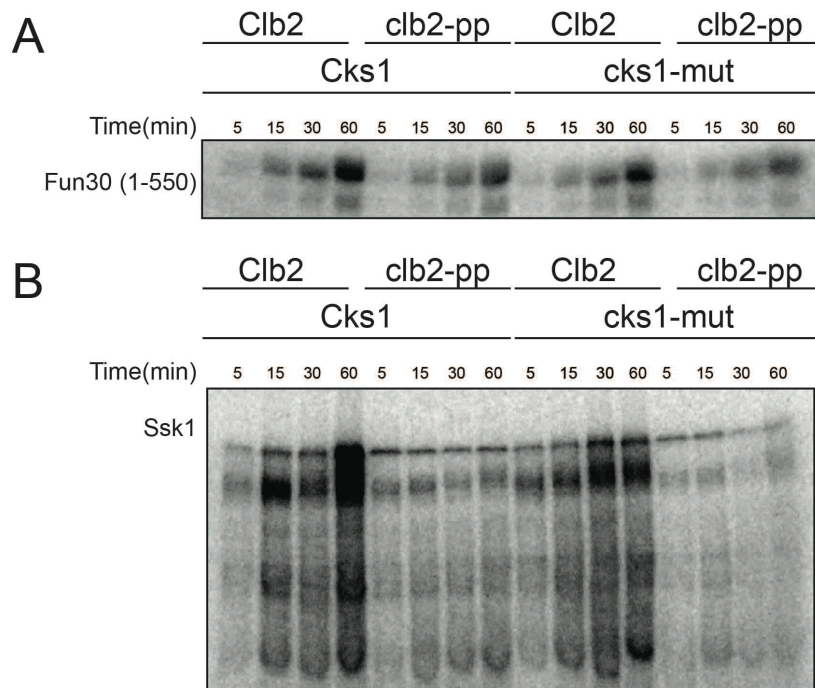


Fig 2.5 Phosphorylation is reduced with clb2-pp *in vitro*

- A. Purified Fun30 fragment (aa 1-550) was incubated with wild-type or *clb2-pp* Clb2-Cdk1 with wild-type or mutant Cks1 and radiolabeled ATP. Reaction products were analyzed by PhosTag SDS-PAGE and autoradiography.
- B. Same as A with full length Ssk1.

A. Fun30

```

1  MSGSHSNDED DVVQVPETSS PTKVASSSPL KPTSPTVPDA SVASLRSRFT FKPSDPSEGA
61  HTSKPLPSGS PEVALVNLAR EFPDFSQTLV QAVFKSNSFN LQSARERLTR LRQQRQNWTV
121 NKNASPKKSE TPPPVKKSLP LANTGRLSSI HGNINNKSSK ITVAKQKTSI FDRYSNVINQ
181 KQYTFELPTN LNIDSEALSK LPVNYNKKRR LVRADQHPIG KSYESSATQL GSAREKLLAN
241 RKYGRHANDN DEEEEEEMMT DDDDASGDDY TESTPQINLD EQVLQFINDS DIVDLSDLSD
301 TTMHKAQLIA SHRPYSSLNA FVNTNFNDKD TEENASNKRK RRAAASANES ERLLDKITQS
361 IRGYNAIESV IKKCSSYGDL VTSQMKKWGV QVEGDNSELD LMNLGEDDDD DNDDGNNDNN
421 NSNNNTAGA DATSKEKEDT KAVEGFDET SAEPTPAPAP APVERETKRI RNTTKPKVVE
481 DEDDDVDLEA IDDEL PQSEH EDDDYEEEDE DYNDEEEDVE YDDGDDDDDD DDEFVATRKN
541 THVISTTSRN GRKPIVKFFK GKPRLLSPEI SLKDYQQTGI NWLNLLYQNK MSCILADDMG
601 LGKTCQVISF FAYLKQINEP GPHLVVVPSS TLENWREFQ KFAPALKIEP YYGSLQEREE
661 LRDILERNAG KYDVIVTTYN LAAGNKYDVS FLKRNRFNVV VYDEGHMLKN STSERFAKLM
721 KIRANFRLLL TGTPQLNNLK ELMSLLEFIM PNLFISKKES FDAIFKQRAK TTDDNKNHNP
781 LLAQEAITRA KTMMPFILR RRKDQVLKHL PPKHTHIQYC ELNAIQKKIY DKEIQIVLEH
841 KRMIKDGELP KDAKEKSKLQ SSSSKNLIMA LRKASLHPLL FRNIYNDKII TKMSDAILDE
901 PAYAENGNGE YIKEDMSYMT DFELHKLCCN FPNTLSKYQL HNDEWMQSGK IDALKKLLKT
961 IIVDKQEKVL IFSLFTQVLD ILEMVLSTLD YKFLRLDGST QVNDRQLLID KFYEDKDIPI
1021 FILSTKAGGF GINLVCANNV IIFDQSFNPH DDRQAADRAH RVGQTKEVNI TTLITKDSIE
1081 EKIHQLAKNK LALDSYISED KKSQDVLESK VSDMLEDIY DENSKPKGKT E*
```

B. Ssk1

```

1  MLNSALLWKV WLRIDNSTDE VNQPIAVQFD EIDTVDDLKS RFFQKLSSTR WREINDNASI
61  AIGLYAPKFD NQADNTSSNN TNDNSCRSKS NGAGSGANLS VNSNTKSSVS PTAGSFGLSK
121 DLAKDRNVLQ HPKPTQKRGV LYDAFAAVPT VAATTNVDFP PNEAPMLSPQ RPYSTSPKQF
181 PATTKSPLLR FASVSPYPKE HSDNQIMASA GLTYVSPHMK NKYTRPLIRK GLNFTTESVN
241 DCTYKIIFEP DELAINIYKE LFGTMGSQPA SQPLLIFSNV NLRQDVPLD ILNVVDYVPT
301 NEEISQKQTQ PTDHGAVGVF HLDDHISPGE QGLKQTIGDK ADLKGKDGNS SPQEFKLITD
361 EEQLRRASQE LKDEEKDAES PWQAILLPK GYKGGVDFRN KPVAHTDSSF NNEDTITHSE
421 LEVNTGSPSQ ESGSLNEAGI GITQPMSEVQ RRKEDVTPAS PILTSSQTPH YNSLYNAPF
481 AVSSPPDPLP NLFTTTSEKV FPKINVLIVE DNVINQAILG SFLRKHKISY KLAKNGQEAV
541 NIWKEGGLHL IFMDLQLPVL SGIEAAKQIR DFQKQNGIGI QKSLNNSHSN LEKGTSKRFS
601 QAPVIVALT ASNSQMDKRR ALLSGCNDYL TKPVNLHWLS KKITEWGCMT ALIDFDSWKQ
661 GESRMTDVL VKSPQKPIAP SNPHSFKQAT SMTPTHSPVR KNSNLSPTQI EL*
```

Fig S2.1. Protein sequences of selected proteins identified from SILAC-MS

- A. Protein sequence of Fun30. Underlined is the peptide sequence identified in the MS analysis. CDK consensus sequences (S/T*-P) are highlighted in orange, and S/T residues identified previously as phosphorylation sites *in vivo* are shown in bold. Highlighted in blue is the recombinant fragment used in our *in vitro* assays.
- B. Same as A with Ssk1.

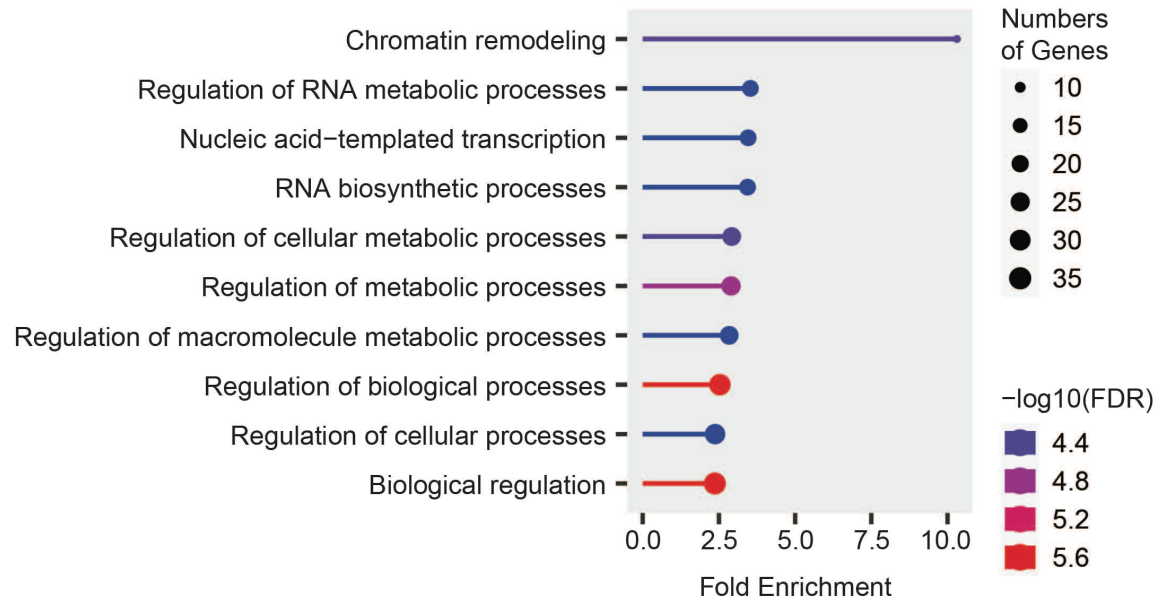


Fig S2.2. GO Analysis of proteins which phosphorylation is reduced in *clb2-pp*

The top ranked GO terms according to significant fold enrichment in the Biological Process (BP) category. “Number of Gene” is the number of genes enriched in a GO term. “-Log (FDR)” is the log 10 of the false discovery rate calculated based on nominal P-value from the hypergeometric test representing the confidence of enrichment. “Fold Enrichment” is defined as the percentage of genes belonging to a pathway, divided by the corresponding percentage in the background indicating how drastically genes of a certain pathway is overrepresented.

Table 2.1 Yeast Strain Table

	Genotype	Source
DOM123	<i>MATa, bar1-HisG</i>	ATCC
yJBA53	<i>trp1::pGAL-NDD1-9xMYC-TRP1</i>	105
yHN40	<i>Δclb2::HYGR, trp1::pGAL-NDD1-9xMYC-TRP1</i>	This Study
yJBA71	<i>clb2::CLB2-R336A,R379A,K383A-HYGR, trp1::pGAL-NDD1-9xMYC-TRP1</i>	105
yHN01	<i>Δclb3::pAgTEF-KANMX-tAgTEF, trp1::pGAL-NDD1-9xMYC-TRP1</i>	This Study
yHN02	<i>Δclb1::pAGTEF-NATNT-tADH1, trp1::pGAL-NDD1-9xMYC-TRP1</i>	This Study
yHN03	<i>Δclb3::pAgTEF-KANMX-tAgTEF, clb2::CLB2-R336A,R379A,K383A-HYGR, trp1::pGAL-NDD1-9xMYC-TRP1</i>	This Study
yHN04	<i>Δclb1::pAGTEF-NATNT-tADH1, clb2::CLB2-R336A,R379A,K383A-HYGR, trp1::pGAL-NDD1-9xMYC-TRP1</i>	This Study
yHN05	<i>Δclb3::pAgTEF-KANMX-tAgTEF, Δclb1::pAGTEF-NATNT-tADH1, trp1::pGAL-NDD1-9xMYC-TRP1</i>	This Study
yHN06	<i>Δclb3::pAgTEF-KANMX-tAgTEF, Δclb1::pAGTEF-NATNT-tADH1, clb2::CLB2-R336A,R379A,K383A-HYGR, trp1::pGAL-NDD1-9xMYC-TRP1</i>	This Study
DOM1324	<i>SPC42-mCherry-HIS3</i>	160
yHN24	<i>SPC42-mCherry-HIS3, clb2::CLB2-R336A,R379A,K383A-HYGR</i>	This Study
DOM1228	<i>pds1::PDS1-myc13-TRP1</i>	161
yHN10	<i>pds1::PDS1-myc13-TRP1, clb2::CLB2-R336A,R379A,K383A-HYGR</i>	This Study
yHN22	<i>pds1::PDS1-myc13-TRP1, Δclb3::pAgTEF-KANMX-tAgTEF, Δclb1::pAGTEF-NATNT-tADH1</i>	This Study
yHN21	<i>pds1::PDS1-myc13-TRP1, Δclb3::pAgTEF-KANMX-tAgTEF, Δclb1::pAGTEF-NATNT-tADH1, clb2::CLB2-R336A,R379A,K383A-HYGR</i>	This Study
HZY292	<i>ura3-52, leu2Δ1, trp1Δ63, his3Δ200, lys2ΔBgl, arg4Δ, sml1Δ::TRP1, hom3-10, ade2Δ, ade8, ade8 has 2 NT loss, S288c</i>	162
yHN07	<i>ura3-52, leu2Δ1, trp1Δ63, his3Δ200, lys2ΔBgl, arg4Δ, sml1Δ::TRP1, hom3-10, ade2Δ, ade8, ade8 has 2 NT loss, clb2::CLB2-R336A,R379A,K383A-HYGR, S288c</i>	This Study
DOM77	<i>sic1::LEU2, bar1::HisG + pAB1234-2micron Gal-CLB2-TAP-URA3</i>	99
MO840	<i>sic1::LEU2, bar1::HisG + pAB1234-clb2-2micron Gal-CLB2-R336A,R379A,K383A-TAP-URA3</i>	105
DOM1231	<i>pds1::PDS1-MYC-TRP1 cdc20::CDC20 mad2Δ::KAN</i>	161
yHN39	<i>pds1::PDS1-MYC-TRP1 cdc20::CDC20 mad2Δ::KAN clb2::CLB2-R336A,R379A,K383A-HYGR</i>	This Study
yHN41	<i>pds1::PDS1-myc13-TRP1, apc1::APC1 Δ225-365-NATNT</i>	This Study
yHN42	<i>pds1::PDS1-myc13-TRP1, apc1::APC1 Δ225-365-NATNT, clb2::CLB2-R336A,R379A,K383A-HYGR</i>	This Study

Table 2.2 Plasmid Table

	Description	Source
pEV652	pET-CKS1	128
pEV653	pET-CKS1mutant (R33A/S82E/R102A)	106
pMO1020	pET-6xHis-Ndd1(1-272)	105
pHN37	pET28a-6xHis-SUMO-Fun30(1-550)	This Study
pHN40	pET28a-6xHis-SUMO-Ssk1	This Study

Table S2.1 MS Analyzed peptide containing CDK site with Log2 L/H > 1

Gene		Normalized L/H Log2	S/TPxK/R sites	S/TP sites	Ubersax P-score Table S1 ⁹⁹	Holt Table S1 ¹⁰⁰	Loog Table S1 Clb5:2 ¹⁰¹	Peptide sequence [Molecular weight of modified residue]
YPL202C	Aft2	10.064 7428						L.EYKAS[167.00]LNLPLVT[181.01]PII S[167.00]C[160.03]DC[160.03]GLTK.E
YOL062C	Apm4	1.2819 5698	0	5	1.6			R.NMGGLLDSPDGNDVLSSSS[167.00] SS[167.00]PT[181.01]SSAGELHFPK.F
YLR399C	Bdf1	1.4335 6088						R.DASS[167.00]LS[167.00]PTSAGSR. K
YLR399C	Bdf1	1.5448 0537						R.DASS[167.00]LS[167.00]PTSAGSR[166.11].K
YCL029C	Bik1	2.2112 5186						R.LTNQFS[167.00]PMDDPKS[167.00] PT[181.01]PMR.S
YFL007W	Blm10	1.3185 1612	2	6	1.2	X		R.S[167.00]AT[181.01]PTLQDQK.L
YDL099W	Bug1	2.7020 0192				X		K.NSSAT[181.01]GSIGS[167.00]ET[18 1.01]PDLEGTPGEESTQEETVK.A
YER026C	Cho1	1.2708 3278						R.AS[167.00]S[167.00]IFSINTT[181.01] JPLAPPNATDIQK.F
YER026C	Cho1	1.8096 251						R.ASSIFS[167.00]INT[181.01]T[181.01] JPLAPPNATDIQK.F
YOR042W	Cue5	2.6680 4972				X		K.VVAETTYIDT[181.01]PDTET[181.01] JKKK.W
YDL117W	Cyk3	9.2099 4068	1	8	1.6			R.NTNIYSS[167.00]SVSSPKS[167.00] PK.A
YIR023W	Dal81	1.4382 6701	2	19	3.7	X		R.SGVQSQIPIQFNVGS[167.00]PAMT [181.01]EQGS[167.00]PLNQWK.N
YPL049C	Dig1	1.1279 6086						K.RVNSYDS[167.00]PLS[167.00]GT ASTGK.T
YKL204W	Eap1	8.3068 212						R.ES[167.00]AS[167.00]HET[181.01]P TDLRPVIPR.G

Gene		Normalized L/H Log2	S/TPxK/R sites	S/TP sites	Ubersax P-score Table S1 ⁹⁹	Holt Table S1 ¹⁰⁰	Loog Table S1 Cib5:2 ¹⁰¹	Peptide sequence [Molecular weight of modified residue]
YAL019W	Fun30	1.1462 5134	3	10	5.8		0.9	K.AVVEGFDET[181.01]S[167.00]AEP T[181.01]PAPAPAPVER.E
YAL019W	Fun30	1.3725 1718	3	10	5.8		0.9	K.AVVEGFDET[181.01]S[167.00]AEP T[181.01]PAPAPAPVER.E
YAL019W	Fun30	2.4468 8637	3	10	5.8		0.9	K.AVVEGFDET[181.01]S[167.00]AEP T[181.01]PAPAPAPVER.E
YAL019W	Fun30	3.2094 5337	3	10	5.8		0.9	K.AVVEGFDET[181.01]S[167.00]AEP T[181.01]PAPAPAPVER.E
YAL019W	Fun30	9.8841 7052	3	10	5.8		0.9	K.AVVEGFDET[181.01]S[167.00]AEP T[181.01]PAPAPAPVER.E
YOL051W	Gal11	3.2399 4062				X		K.KLS[167.00]ISNAAS[167.00]QQPT[1 81.01]PR.S
YOR025W	Hst3	1.6364 928	1	6	1.8			K.ILS[167.00]PENS[167.00]S[167.00]E EDEEENLDTR.K
YOR025W	Hst3	2.5267 2646	1	6	1.8			K.ILS[167.00]PENS[167.00]S[167.00]E EDEEENLDTR.K
YFL013C	les1	2.1388 4463						K.SGSQEEAS[167.00]PS[167.00]SIQ S[167.00]ETETVTTK.S
YDR229W	Ivy1	1.1529 9909						M.PDNNTEQLQGS[167.00]PSS[167.0 0]DQR.L
YJR091C	Jsn1	1.8944 4054	2	11	2		1.7	K.MMESSIDGVTMDRPGS[167.00]LT[181.01]PPQDM[147.04]EK.L
YJR091C	Jsn1	2.2415 8599	2	11	2		1.7	K.M[147.04]MESSIDGVTMDRPGS[16 7.00]LT[181.01]PPQDMEK.L
YLL019C	Kns1	1.0979 4505						K.AVNLTIAHS[167.00]TS[167.00]PFS NPPAQIASLPQSNLK.K
YLL019C	Kns1	1.1443 8991						K.AVNLTIAHS[167.00]TS[167.00]PFS NPPAQIASLPQSNLK[136.11].K
YLL019C	Kns1	1.7889 1767						K.AVNLTIAHST[181.01]S[167.00]PFS NPPAQIASLPQSNLK.K

Gene		Normalized L/H Log2	S/TPxK/R sites	S/TP sites	Ubersax P-score Table S ¹⁹⁹	Holt Table S ¹⁰⁰	Loog Table S1 Cib5:2 ¹⁰¹	Peptide sequence [Molecular weight of modified residue]
YHR082C	Ksp1	1.1963 1891						R.RGS[167.00]TTTVQHS[167.00]PGA YIPPNA.R.N
YDL240W	Lrg1	1.6191 3164						R.SLNTAS[167.00]PMT[181.01]VQVK. N
YER068W	Mot2	3.1840 0019						R.SGIHNNISTSTAGSNT[181.01]NLLS ENFTGT[181.01]PS[167.00]PAAMR.A
YMR037C	Msn2	1.1069 152						R.NTNLNITTNST[181.01]SSS[167.00] NAS[167.00]PNTTTMNANADSNIAGN PK.N
YKL062W	Msn4	1.0599 6196				X		R.RGS[167.00]TIS[167.00]PTTTINNS NPNFK.L
YKL062W	Msn4	1.1647 2708				X		R.RGS[167.00]T[181.01]IS[167.00]PT TTINNSNPNFK.L
YKL062W	Msn4	1.6409 9654				X		R.RGS[167.00]TIS[167.00]PTTTINNS NPNFK.L
YKL062W	Msn4	2.0840 0894				X		R.RGS[167.00]T[181.01]IS[167.00]PT TTINNSNPNFK.L
YMR153W	Nup53	9.7498 6943	2	7	1.4			K.TDNIEDPNLSSNITFDGKPT[181.01] AT[181.01]PS[167.00]PFRPLEK.T
YHR118C	Orc6	1.0239 4172	6	50*	4.1	X	68	K.QFAWT[181.01]PS[167.00]PK[136.1 1].K
YIR006C	Pan1	3.7504 9259						K.SVTESSPFVPS[167.00]ST[181.01]P T[181.01]PVDDR.S
YNR070W	Pdr18	12.016 8083						Y.WLDS[167.00]PEYARLK.G
YOL011W	Plb3	3.7475 6184						D.LS[167.00]QDFNDIAVYS[167.00]PN PFK.D
YBL035C	Pol12	2.4880 7641				X		K.SSDAKT[181.01]PGS[167.00]STFQ TPTTNTPTTSR.Q

Gene		Normalized L/H Log2	S/TPxK/R sites	S/TP sites	Ubersax P-score Table S1 ⁹⁹	Holt Table S1 ¹⁰⁰	Loog Table S1 Cib5:2 ¹⁰¹	Peptide sequence [Molecular weight of modified residue]
YER075C	Ptp3	9.9366 3794				X		R.NVLSDSPMSSS[167.00]S[167.00]PI SALFK.F
YKR090W	Pxl1	1.9190 0028	1	9	2.9		0.9	K.IPEINVTRES[167.00]NT[181.01]PS[167.00]LTMNALDSK.L
YPR115W	Rgc1	10.720 2443						R.LSDIVY[243.03]PNM[147.04]KS[167 .00]PLAK.C
YPL089C	Rlm1	10.846 2739						R.SSKIS[167.00]PLS[167.00]ASASGP LT[181.01]LQK.G
YPL089C	Rlm1	11.258 566						R.SSKIS[167.00]PLSASAS[167.00]GP LT[181.01]LQK.G
YLR357W	Rsc2	1.9873 8995				X		R.S[167.00]T[181.01]TPSHSGT[181.0 1]PQPLGPR.H
YPL085W	Sec16	1.0049 9491	2	28	1.6	X		K.TSPS[167.00]PTGPNPNNSPS[167. 00]PSS[167.00]PISR.L
YPL085W	Sec16	1.0236 7283	2	28	1.6	X		K.TSPSPT[181.01]GPNPNNSPS[167. 00]PSS[167.00]PISR.L
YDL195W	Sec31	1.2261 3968				X		R.VAT[181.01]PLS[167.00]GGVPPAP LPK[136.11].A
YKR072C	Sis2	2.0221 9137				X		R.QS[167.00]IS[167.00]PTLSNATTTT TK.S
YNL311C	Skp2	2.8073 5492						R.LNDET[181.01]PIIT[181.01]S[167.00]JER.L
YNL243W	Sla2	2.1472 0492	2	10	1.9	X		K.LITSEDNENT[181.01]S[167.00]PEQ FIVAS[167.00]K.E
YOR290C	Snf2	2.0111 0159						K.LEGSENSEPPALES[167.00]SPVT[1 81.01]GDNS[167.00]PSEDFMDIPKPR .T
YOR290C	Snf2	2.8662 4861						K.LEGSENSEPPALES[167.00]SPVT[1 81.01]GDNS[167.00]PSEDFMDIPKPR .T

Gene		Normalized L/H Log2	S/TPxK/R sites	S/TP sites	Ubersax P-score Table S1 ⁹⁹	Holt Table S1 ¹⁰⁰	Loog Table S1 Cib5:2 ¹⁰¹	Peptide sequence [Molecular weight of modified residue]
YLR006C	Ssk1	1.3756 6989	3	18	2.8	X	0.6	R.FAS[167.00]VS[167.00]PYPK[136.11].F
YLR006C	Ssk1	1.4661 0473	3	18	2.8	X	0.6	R.FAS[167.00]VS[167.00]PYPK.F
YLR006C	Ssk1	1.5451 4704	3	18	2.8	X	0.6	R.FAS[167.00]VS[167.00]PYPK[136.11].F
YDR320C	Swa2	1.7471 0404						R.TAPDVSHSS[167.00]S[167.00]PTS GILIEENSR.R
YPL105C	Syh1	1.4550 5318						R.ASSLDDFIS[167.00]RT[181.01]PS[167.00]PSSSALNSSNTSNAWTTVSSK. S
YHR009C	Tda3	1.2296 9722						R.S[167.00]HTNS[167.00]ASDLDSVS[167.00]PVEQLR.E
YJL048C	Ubx6	2.8073 5492						K.LSSLDMVSDGGGGGGGDSMT[181.01]PS[167.00]AYT[181.01]TPR.M
YDR213W	Upc2	1.2223 9242						R.NSNIS[167.00]PST[181.01]PSAVLN DRQEMQDSISSLGNLTK.A
YDR485C	Vps72	10.147 2049						K.QVTFTDHPQVAIIDT[181.01]EES[167.00]PSKK.D
YML076C	War1	1.0973 5638				X		R.S[167.00]RS[167.00]PT[181.01]PFE SPMVNVSTK.S
YEL043W		2.4217 0123				X		R.STNESLFSTTGT[181.01]PM[147.04] JSSYK.A
YHR097C		1.8598 2234						K.NVDTIDKMDVT[181.01]GLFGGS[167.00]FHHDGPFDAC[160.03]T[181.01] P.Q

*19 duplicates shaded yellow in "Gene" column, so 50 unique proteins on list

†Red shading in "Ubersax P score" column indicates score of 2 or higher

References

1. Reyes-Turcu FE, Zhang K, Zofall M, Chen E, Grewal SIS. Defects in RNA quality control factors reveal RNAi-independent nucleation of heterochromatin. *Nat Struct Mol Biol.* 2011;18(10):1132-1138.
2. Hall IM, Shankaranarayana GD, Noma K ichi, Ayoub N, Cohen A, Grewal SIS. Establishment and maintenance of a heterochromatin domain. *Science (1979).* 2002;297(5590):2232-2237.
3. Lachner M, O'Carroll D, Rea S, Mechtler K, Jenuwein T. Methylation of histone H3 lysine 9 creates a binding site for HP1 proteins. *Nature.* 2001;410(6824):116-120.
4. Jacobs SA, Taverna SD, Zhang YN, et al. Specificity of the HP1 chromo domain for the methylated N-terminus of histone H3. *Embo Journal.* 2001;20(18):5232-5241.
5. Fischer T, Cui B, Dhakshnamoorthy J, et al. Diverse roles of HP1 proteins in heterochromatin assembly and functions in fission yeast. *Proc Natl Acad Sci USA.* 2009;106(22):8998-9003.
6. Buhler M, Moazed D. Transcription and RNAi in heterochromatic gene silencing. *Nat Struct Mol Biol.* 2007;14(11):1041-1048.
7. Buhler M, Haas W, Gygi SP, Moazed D. RNAi-dependent and -independent RNA turnover mechanisms contribute to heterochromatic gene silencing. *Cell.* 2007;129(4):707-721.
8. Greenstein RA, Barrales RR, Sanchez NA, Bisanz JE, Braun S, Al-Sady B. Set1/COMPASS repels heterochromatin invasion at euchromatic sites by disrupting Suv39/Clr4 activity and nucleosome stability. *Genes Dev.* 2019;34(1-2):99-117.
9. Scott KC, Merrett SL, Willard HF. A heterochromatin barrier partitions the fission yeast centromere into discrete chromatin domains. *Curr Biol.* 2006;16(2):119-129.

10. Wen B, Wu H, Shinkai Y, Irizarry RA, Feinberg AP. Large histone H3 lysine 9 dimethylated chromatin blocks distinguish differentiated from embryonic stem cells. *Nat Genet.* 2009;41(2):246-250.
11. Zyllicz JJ, Borensztein M, Wong FC, et al. G9a regulates temporal preimplantation developmental program and lineage segregation in blastocyst. *Elife.* 2018;7.
<https://elifesciences.org/articles/33324>
12. Zyllicz JJ, Dietmann S, Gunesdogan U, et al. Chromatin dynamics and the role of G9a in gene regulation and enhancer silencing during early mouse development. *Elife.* 2015;4.
<https://elifesciences.org/articles/09571>
13. Zhu J, Adli M, Zou J, et al. Genome-wide chromatin state transitions associated with developmental and environmental cues. *Cell.* 2013;152(3):642-654.
[https://www.cell.com/fulltext/S0092-8674\(13\)00068-5](https://www.cell.com/fulltext/S0092-8674(13)00068-5)
14. Nicetto D, Zaret KS. Role of H3K9me3 heterochromatin in cell identity establishment and maintenance. *Curr Opin Genet Dev.* 2019;55:1-10.
15. Alabert C, Barth TK, Reveron-Gomez N, et al. Two distinct modes for propagation of histone PTMs across the cell cycle. *Genes Dev.* 2015;29(6):585-590.
16. Zhang K, Mosch K, Fischle W, Grewal SIS. Roles of the Clr4 methyltransferase complex in nucleation, spreading and maintenance of heterochromatin. *Nat Struct Mol Biol.* 2008;15(4):381-388.
17. Ragunathan K, Jih G, Moazed D. Epigenetic inheritance uncoupled from sequence-specific recruitment. *Science (1979).* 2015;348(6230):1258699.
18. Al-Sady B, Madhani HD, Narlikar GJ. Division of labor between the chromodomains of HP1 and Suv39 methylase enables coordination of heterochromatin spread. *Mol Cell.* 2013;51(1):80-91.
19. Moazed D. Small RNAs in transcriptional gene silencing and genome defence. *Nature.* 2009;457(7228):413-420.

20. Zofall M, Yamanaka S, Reyes-Turcu FE, Zhang K, Rubin C, Grewal SI. RNA elimination machinery targeting meiotic mRNAs promotes facultative heterochromatin formation. *Science (1979)*. 2012;335(6064):96-100.
21. Zofall M, Smith DR, Mizuguchi T, Dhakshnamoorthy J, Grewal SIS. Taz1-Shelterin Promotes Facultative Heterochromatin Assembly at Chromosome-Internal Sites Containing Late Replication Origins. *Mol Cell*. Published online 2016.
doi:10.1016/j.molcel.2016.04.034
22. Wang J, Cohen AL, Letian A, et al. The proper connection between shelterin components is required for telomeric heterochromatin assembly. *Genes Dev*. 2016;30(7):827-839.
doi:10.1101/gad.266718.115
23. Jia S. RNAi-Independent Heterochromatin Nucleation by the Stress-Activated ATF/CREB Family Proteins. *Science (1979)*. 2004;304(5679):1971-1976.
doi:10.1126/science.1099035
24. Greenstein RA, Jones SK, Spivey EC, Rybarski JR. Noncoding RNA-nucleated heterochromatin spreading is intrinsically labile and requires accessory elements for epigenetic stability. Published online 2018:1-33.
25. Thon G, Bjerling P, Bünner CM, Verhein-Hansen J. Expression-state boundaries in the mating-type region of fission yeast. *Genetics*. 2002;161(2):611-622.
doi:10.1093/genetics/161.2.611
26. Grewal SIS, Klar AJS. A recombinationally repressed region between mat2 and mat3 loci shares homology to centromeric repeats and regulates directionality of mating-type switching in fission yeast. *Genetics*. Published online 1997.
27. Noma K ichi, Cam HP, Maraia RJ, Grewal SIS. A role for TFIIIC transcription factor complex in genome organization. *Cell*. 2006;125(5):859-872.
doi:10.1016/j.cell.2006.04.028

28. Thon G, Friis T. Epigenetic inheritance of transcriptional silencing and switching competence in fission yeast. *Genetics*. 1997;145(3):685-696.
doi:10.1093/genetics/145.3.685
29. Noma KI, Sugiyama T, Cam H, et al. RITS acts in cis to promote RNA interference-mediated transcriptional and post-transcriptional silencing. *Nat Genet*. 2004;36(11):1174-1180. doi:10.1038/ng1452
30. Kim HS, Choi ES, Shin JA, Jang YK, Park SD. Regulation of Swi6/HP1-dependent heterochromatin assembly by cooperation of components of the mitogen-activated protein kinase pathway and a histone deacetylase Ctr6. *J Biol Chem*. 2004;279(41):42850-42859. doi:10.1074/jbc.M407259200
31. Marina DB, Shankar S, Natarajan P, Finn KJ, Madhani HD. A conserved ncRNA-binding protein recruits silencing factors to heterochromatin through an RNAi-independent mechanism. *Genes Dev*. 2013;27(17):1851-1856. doi:10.1101/gad.226019.113
32. Canzio D, Liao M, Naber N, et al. A conformational switch in HP1 releases auto-inhibition to drive heterochromatin assembly. *Nature*. 2013;496(7445):377-381.
doi:10.1038/nature12032
33. Al-Sady B, Greenstein RA, El-Samad HJ, Braun S, Madhani HD. Sensitive and quantitative three-color protein imaging in fission yeast using spectrally diverse, recoded fluorescent proteins with experimentally-characterized in vivo maturation kinetics. *PLoS One*. 2016;11(8):1-20. doi:10.1371/journal.pone.0159292
34. Braun S, Garcia JF, Rowley M, Rougemaille M, Shankar S, Madhani HD. The Cul4-Ddb1Cdt2 ubiquitin ligase inhibits invasion of a boundary-associated antisilencing factor into heterochromatin. *Cell*. Published online 2011. doi:10.1016/j.cell.2010.11.051
35. Bayne EH, Bijos DA, White SA, de Lima Alves F, Rappsilber J, Allshire RC. A systematic genetic screen identifies new factors influencing centromeric heterochromatin integrity in fission yeast. *Genome Biol*. 2014;15(10):481. doi:10.1186/s13059-014-0481-4

36. Tsukii K, Takahata S, Murakami Y. Histone variant H2A.Z plays multiple roles in the maintenance of heterochromatin integrity. *Genes Cells*. 2022;27(2):93-112. doi:10.1111/gtc.12911
37. Meneghini MD, Wu M, Madhani HD. Conserved histone variant H2A.Z protects euchromatin from the ectopic spread of silent heterochromatin. *Cell*. 2003;112(5):725-736. doi:10.1016/s0092-8674(03)00123-5
38. Holla S, Dhakshnamoorthy J, Folco HD, et al. Positioning Heterochromatin at the Nuclear Periphery Suppresses Histone Turnover to Promote Epigenetic Inheritance Article Positioning Heterochromatin at the Nuclear Periphery Suppresses Histone Turnover to Promote Epigenetic Inheritance. *Cell*. Published online 2020:1-15. doi:10.1016/j.cell.2019.12.004
39. Grewal SIS, Klar AJS. Chromosomal inheritance of epigenetic states in fission yeast during mitosis and meiosis. *Cell*. 1996;86(1):95-101. doi:10.1016/S0092-8674(00)80080-X
40. Webb S, Braun S, Barrales RR, et al. Global regulation of heterochromatin spreading by Leo1. *Open Biol*. 2015;5(5):150045-150045. doi:10.1098/rsob.150045
41. Krogan NJ, Keogh MC, Datta N, et al. A Snf2 family ATPase complex required for recruitment of the histone H2A variant Htz1. *Mol Cell*. 2003;12(6):1565-1576. doi:10.1016/s1097-2765(03)00497-0
42. Lock A, Rutherford K, Harris MA, et al. PomBase 2018: User-driven reimplementations of the fission yeast database provides rapid and intuitive access to diverse, interconnected information. *Nucleic Acids Res*. 2019;47(D1):D821-D827. doi:10.1093/nar/gky961
43. Grewal SI, Bonaduce MJ, Klar AJ. Histone deacetylase homologs regulate epigenetic inheritance of transcriptional silencing and chromosome segregation in fission yeast. *Genetics*. 1998;150(2):563-576. doi:10.1093/genetics/150.2.563

44. Nicolas E, Yamada T, Cam HP, Fitzgerald PC, Kobayashi R, Grewal SIS. Distinct roles of HDAC complexes in promoter silencing, antisense suppression and DNA damage protection. *Nat Struct Mol Biol.* 2007;14(5):372-380. doi:10.1038/nsmb1239
45. Sugiyama T, Cam HP, Sugiyama R, et al. SHREC, an effector complex for heterochromatic transcriptional silencing. *Cell.* 2007;128(3):491-504. doi:10.1016/j.cell.2006.12.035
46. Shankaranarayana GD, Motamedi MR, Moazed D, Grewal SIS. Sir2 regulates histone H3 lysine 9 methylation and heterochromatin assembly in fission yeast. *Curr Biol.* 2003;13(14):1240-1246. doi:10.1016/s0960-9822(03)00489-5
47. Zilio N, Codlin S, Vashisht AA, et al. A Novel Histone Deacetylase Complex in the Control of Transcription and Genome Stability. *Mol Cell Biol.* 2014;34(18):3500-3514. doi:10.1128/mcb.00519-14
48. Yamada T, Fischle W, Sugiyama T, Allis CD, Grewal SIS. The nucleation and maintenance of heterochromatin by a histone deacetylase in fission yeast. *Mol Cell.* 2005;20(2):173-185. doi:10.1016/j.molcel.2005.10.002
49. Jih G, Iglesias N, Currie MA, et al. Unique roles for histone H3K9me states in RNAi and heritable silencing of transcription. *Nature.* 2017;547(7664):463-467. doi:10.1038/nature23267
50. Buck V, Ng SS, Ruiz-Garcia AB, et al. Fkh2p and Sep1p regulate mitotic gene transcription in fission yeast. *J Cell Sci.* 2004;117(Pt 23):5623-5632. doi:10.1242/jcs.01473
51. Bulmer R, Pic-Taylor A, Whitehall SK, Martin KA, Millar JB, Quinn J. The forkhead transcription factor Fkh2 regulates the cell division cycle of *Schizosaccharomyces pombe*. *Eukaryot Cell.* 2004;3(4):944-954. <https://ec.asm.org/content/3/4/944>

52. Rossi A, Kontarakis Z, Gerri C, et al. Genetic compensation induced by deleterious mutations but not gene knockdowns. *Nature*. 2015;524(7564):230-233.
<https://www.nature.com/articles/nature14580>
53. Yamane K ichi, Mizuguchi T, Cui B, Zofall M, Noma K ichi, Grewal SIS. Asf1/HIRA facilitate global histone deacetylation and associate with HP1 to promote nucleosome occupancy at heterochromatic loci. *Mol Cell*. 2011;41(1):56-66.
<https://www.sciencedirect.com/science/article/pii/S109727651000875X>
54. Shevchenko A, Roguev A, Schaft D, et al. Chromatin Central: towards the comparative proteome by accurate mapping of the yeast proteomic environment. *Genome Biol*. 2008;9(11):R167. <https://genomebiology.biomedcentral.com/articles/10.1186/gb-2008-9-11-r167>
55. Yu Y, Zhou H, Deng X, Wang W, Lu H. Set3 contributes to heterochromatin integrity by promoting transcription of subunits of Clr4-Rik1-Cul4 histone methyltransferase complex in fission yeast. *Sci Rep*. 2016;6:31752. <https://www.nature.com/articles/srep31752>
56. Murawska M, Greenstein RA, Schauer T, et al. The histone chaperone FACT facilitates heterochromatin spreading by regulating histone turnover and H3K9 methylation states. *Cell Rep*. 2021;37(5):109944.
<https://www.sciencedirect.com/science/article/pii/S2211124721014175>
57. Alves-Rodrigues I, Ferreira PG, Moldón A, et al. Spatiotemporal Control of Forkhead Binding to DNA Regulates the Meiotic Gene Expression Program. *Cell Rep*. 2016;14(4):885-895.
<https://www.sciencedirect.com/science/article/pii/S2211124716000331>
58. Garg A, Futcher B, Leatherwood J. A new transcription factor for mitosis: in *Schizosaccharomyces pombe*, the RFX transcription factor Sak1 works with forkhead factors to regulate mitotic expression. *Nucleic Acids Res*. 2015;43(14):6874-6888.
<https://academic.oup.com/nar/article/43/14/6874>

59. Knott SR, Peace JM, Ostrow AZ, et al. Forkhead transcription factors establish origin timing and long-range clustering in *S. cerevisiae*. *Cell*. 2012;148(1-2):99-111.
<https://www.sciencedirect.com/science/article/pii/S0092867411016105>
60. Zenk F, Zhan Y, Kos P, et al. HP1 drives de novo 3D genome reorganization in early *Drosophila* embryos. *Nature*. 2021;593(7858):289-293.
<https://www.nature.com/articles/s41586-021-03596-9>
61. Sanulli SG, Narlikar GJ. Liquid-like interactions in heterochromatin: Implications for mechanism and regulation. *Curr Opin Cell Biol*. 2020;64:90-96.
<https://www.sciencedirect.com/science/article/pii/S0955067419301740>
62. Al-Sady B, Kikis EA, Monte E, Quail PH. Mechanistic duality of transcription factor function in phytochrome signaling. *Proc Natl Acad Sci U S A*. 2008;105(6):2232-2237.
<https://www.pnas.org/content/105/6/2232>
63. Canzio D, Chang EY, Shankar S, et al. Chromodomain-mediated oligomerization of HP1 suggests a nucleosome-bridging mechanism for heterochromatin assembly. *Mol Cell*. 2011;41(1):67-81. <https://www.sciencedirect.com/science/article/pii/S1097276510008761>
64. Yang X, Seto E. The Rpd3/Hda1 family of lysine deacetylases: from bacteria and yeast to mice and men. *Nat Rev Mol Cell Biol*. 2008;9(3):206-218.
<https://www.nature.com/articles/nrm2346>
65. Lorch Y, Kornberg RD. Chromatin-remodeling for transcription. *Q Rev Biophys*. 2017;50:e5. <https://www.cambridge.org/engage/api-gateway/quc:site/publications/5e2189a3bb3c2854e334ed4d>
66. Garcia JF, Dumesic PA, Hartley PD, El-Samad H, Madhani HD. Combinatorial, site-specific requirement for heterochromatic silencing factors in the elimination of nucleosome-free regions. *Genes Dev*. 2010;24(16):1758-1771.
<https://www.genesdev.org/content/24/16/1758>

67. Lantermann AB, Straub T, Stralfors A, Yuan GC, Ekwall K, Korber P. Schizosaccharomyces pombe genome-wide nucleosome mapping reveals positioning mechanisms distinct from those of Saccharomyces cerevisiae. *Nat Struct Mol Biol.* 2010;17(2):251–U15. <https://www.nature.com/articles/nsmb.1759>
68. Narlikar GJ, Phelan ML, Kingston RE. Generation and Interconversion of Multiple Distinct Nucleosomal States as a Mechanism for Catalyzing Chromatin Fluidity. *Mol Cell.* 2001;8(6):1219-1230. <https://www.sciencedirect.com/science/article/pii/S1097276501004530>
69. Rowe CE, Narlikar GJ. The ATP-dependent remodeler RSC transfers histone dimers and octamers through the rapid formation of an unstable encounter intermediate. *Biochemistry.* 2010;49(45):9882-9890. <https://pubs.acs.org/doi/abs/10.1021/bi101182b>
70. Rawal Y, Chereji R V, Qiu H, et al. SWI/SNF and RSC cooperate to reposition and evict promoter nucleosomes at highly expressed genes in yeast. *Genes Dev.* 2018;32(9-10):695-710. <https://www.genesdev.org/content/32/9-10/695>
71. Volpe TA, Kidner C, Hall IM, Teng G, Grewal SIS, Martienssen RA. Regulation of heterochromatic silencing and histone H3 lysine-9 methylation by RNAi. *Science (1979).* 2002;297(5588):1833-1837. <https://science.sciencemag.org/content/297/5588/1833>
72. Bao K, Shan CM, Moresco J, Yates J, Jia S. Anti-silencing factor epe1 associates with SAGA to regulate transcription within heterochromatin. *Genes Dev.* 2019;33(1-2):116-126. doi:10.1101/gad.318030.118
73. Kim JH, Saraf A, Florens L, Washburn M, Workman JL. Gcn5 regulates the dissociation of SWI/SNF from chromatin by acetylation of Swi2/Snf2. *Genes Dev.* 2010;24(24):2766-2771. <https://www.genesdev.org/content/24/24/2766>
74. Cohen A, Habib A, Laor D, Yadav S, Kupiec M, Weisman R. TOR complex 2 in fission yeast is required for chromatin-mediated gene silencing and assembly of heterochromatic

- domains at subtelomeres. *J Biol Chem*. 2018;293(21):8138-8150.
<https://www.jbc.org/content/293/21/8138>
75. Nakayama J, Klar AJ, Grewal SI. A chromodomain protein, Swi6, performs imprinting functions in fission yeast during mitosis and meiosis. *Cell*. 2000;101(3):307-317.
<https://www.sciencedirect.com/science/article/pii/S0092867400810099>
76. Eissenberg JC, Morris GD, Reuter G, Hartnett T. The heterochromatin-associated protein HP-1 is an essential protein in *Drosophila* with dosage-dependent effects on position-effect variegation. *Genetics*. 1992;131(2):345-352.
<https://www.genetics.org/content/131/2/345>
77. Matsuyama A, Arai R, Yashiroda Y, et al. ORFeome cloning and global analysis of protein localization in the fission yeast *Schizosaccharomyces pombe*. *Nat Biotechnol*. 2006;24(7):841-847. <https://www.nature.com/articles/nbt1222>
78. Barrales RR, Forn M, Georgescu PR, Sarkadi Z, Braun S. Control of heterochromatin localization and silencing by the nuclear membrane protein Lem2. *Genes Dev*. 2016;30(2):133-148. <https://www.genesdev.org/content/30/2/133>
79. Conway JR, Lex A, Gehlenborg N. UpSetR: an R package for the visualization of intersecting sets and their properties. *Bioinformatics*. 2017;33(18):2938-2940.
<https://academic.oup.com/bioinformatics/article/33/18/2938/3094037>
80. Clarke ESM. ggbeeswarm: Categorical Scatter (Violin Point) Plots. R. package version 0.6.0. Published online 2017. <https://CRAN.R-project.org/package=ggbeeswarm>
81. Consortium TGO, others. The Gene Ontology Resource: 20 years and still GOing strong. *Nucleic Acids Res*. 2019;47(D1):D330–D338.
<https://academic.oup.com/nar/article/47/D1/D330/5198160>
82. Gu Z, Eils R, Schlesner M. HilbertCurve: an R/Bioconductor package for high-resolution visualization of genomic data. *Bioinformatics*. 2016;32(15):2372-2374.
<https://academic.oup.com/bioinformatics/article/32/15/2372/216144>

83. Torres-Garcia S, Di Pompeo L, Eivers L, et al. SpEDIT: A fast and efficient CRISPR/Cas9 method for fission yeast. *Wellcome Open Res.* 2020;5.
<https://wellcomeopenresearch.org/articles/5-274>
84. Wickham H. *Ggplot2: Elegant Graphics for Data Analysis*. Springer; 2016.
85. Bolger AM, Lohse M, Usadel B. Trimmomatic: a flexible trimmer for Illumina sequence data. *Bioinformatics.* 2014;30(15):2114-2120.
<https://academic.oup.com/bioinformatics/article/30/15/2114/2190096>
86. Langmead B, Salzberg SL. Fast gapped-read alignment with Bowtie 2. *Nat Methods.* 2012;9(4):357-359. <https://www.nature.com/articles/nmeth.1923>
87. Li H, Handsaker B, Wysoker A, et al. The Sequence Alignment/Map format and SAMtools. *Bioinformatics.* 2009;25(16):2078-2079.
<https://academic.oup.com/bioinformatics/article/25/16/2078/204688>
88. Ramírez F, Ryan DP, Grüning B, et al. deepTools2: a next generation web server for deep-sequencing data analysis. *Nucleic Acids Res.* 2016;44(W1):W160–W165.
<https://academic.oup.com/nar/article/44/W1/W160/2467863>
89. Lawrence M, Gentleman R, Carey V. rtracklayer: an R package for interfacing with genome browsers. *Bioinformatics.* 2009;25(14):1841-1842.
<https://academic.oup.com/bioinformatics/article/25/14/1841/192044>
90. Hahne F, Ivanek R. Visualizing Genomic Data Using Gviz and Bioconductor. *Methods Mol Biol.* 2016;1418:335-351. https://link.springer.com/protocol/10.1007/978-1-4939-3578-9_16
91. Lawrence M, Huber W, Pagès H, et al. Software for computing and annotating genomic ranges. *PLoS Comput Biol.* 2013;9(8):e1003118.
<https://journals.plos.org/ploscompbiol/article?id=10.1371/journal.pcbi.1003118>

92. Lun ATL, Smyth GK. csaw: a Bioconductor package for differential binding analysis of CHIP-seq data using sliding windows. *Nucleic Acids Res.* 2016;44(5):e45.
<https://academic.oup.com/nar/article/44/5/e45/2467880>
93. Love MI, Huber W, Anders S. Moderated estimation of fold change and dispersion for RNA-seq data with DESeq2. *Genome Biol.* 2014;15(12):550.
<https://genomebiology.biomedcentral.com/articles/10.1186/s13059-014-0550-8>
94. Yamanaka S, Mehta S, Reyes-Turcu FE, et al. RNAi triggered by specialized machinery silences developmental genes and retrotransposons. *Nature.* 2013;493(7433):557-560.
<https://www.nature.com/articles/nature11716>
95. Wang J, Reddy BD, Jia S. Rapid epigenetic adaptation to uncontrolled heterochromatin spreading. *Elife.* 2015;4. <https://elifesciences.org/articles/06179>
96. Parsa JY, Boudoukha S, Burke J, Homer C, Madhani HD. Polymerase pausing induced by sequence-specific RNA-binding protein drives heterochromatin assembly. *Genes Dev.* 2018;32(13–14):953-964. <https://doi.org/10.1101/gad.318907.118>
97. Nakayama J, Xiao G, Noma K, et al. Alp13, an MRG family protein, is a component of fission yeast Clr6 histone deacetylase required for genomic integrity. *EMBO J.* 2003;22(11):2776-2787. <https://doi.org/10.1093/emboj/cdg264>
98. Thon G, Bjerling KP, Nielsen IS. Localization and properties of a silencing element near the mat3-M mating-type cassette of *Schizosaccharomyces pombe*. *Genetics.* 1999;151(3):945-963. <https://www.genetics.org/content/151/3/945>
99. Ubersax JA, Woodbury EL, Quang PN, et al. Targets of the cyclin-dependent kinase Cdk1. *Nature.* 2003;425(6960):859-864.
http://www.ncbi.nlm.nih.gov/entrez/query.fcgi?cmd=Retrieve&db=PubMed&dopt=Citation&list_uids=14574415

100. Holt LJ, Tuch BB, Villen J, Johnson AD, Gygi SP, Morgan DO. Global analysis of Cdk1 substrate phosphorylation sites provides insights into evolution. *Science* (1979). 2009;325(5948):1682-1686. doi:325/5948/1682 [pii] 10.1126/science.1172867
101. Loog M, Morgan DO. Cyclin specificity in the phosphorylation of cyclin-dependent kinase substrates. *Nature*. 2005;434:104-108.
102. Coudreuse D, Nurse P. Driving the cell cycle with a minimal CDK control network. *Nature*. 2010;468(7327):1074-1079. doi:10.1038/nature09543
103. Swaffer MP, Jones AW, Flynn HR, Snijders AP, Nurse P. CDK Substrate Phosphorylation and Ordering the Cell Cycle. *Cell*. 2016;167:1750–1761. e16.
104. Wittenberg C, Reed SI. Cell cycle-dependent transcription in yeast: promoters, transcription factors, and transcriptomes. *Oncogene*. 2005;24(17):2746-2755.
http://www.ncbi.nlm.nih.gov/entrez/query.fcgi?cmd=Retrieve&db=PubMed&dopt=Citation&list_uids=15838511
105. Asfaha JB, Örd M, Carlson CR, Faustova I, Loog M, Morgan DO. Multisite phosphorylation by Cdk1 initiates delayed negative feedback to control mitotic transcription. *Curr Biol*. 2022;32(1):256-263.e4. doi:10.1016/j.cub.2021.11.001
106. Koivomagi M, Valk E, Venta R, et al. Cascades of multisite phosphorylation control Sic1 destruction at the onset of S phase. *Nature*. 2011;480:128-131.
107. Ercan DP, Chretien F, Chakravarty P, Flynn HR, Snijders AP, Uhlmann F. Budding yeast relies on G1 cyclin specificity to couple cell cycle progression with morphogenetic development. *Sci Adv*. 2021;7(5):eabg0007.
108. Bhaduri S, Pryciak PM. Cyclin-specific docking motifs promote phosphorylation of yeast signaling proteins by G1/S Cdk complexes. *Current Biology*. 2011;21(19):1615-1623.
109. Ord M, Venta R, Moll K, Valk E, Loog M. Cyclin-Specific Docking Mechanisms Reveal the Complexity of M-CDK Function in the Cell Cycle. *Mol Cell*. 2019;75(1):76–89. e3.

110. Brown NR, Noble MEM, Endicott JA, et al. The crystal structure of cyclin A. *Structure*. 1995;3:1235-1247.
111. Russo AA, Jeffrey PD, Patten A, Massague J, Pavletich NP. Crystal structure of the p27Kip1 cyclin-dependent kinase inhibitor bound to the cyclinA-CDK2 complex. *Nature*. 1996;382:325-331.
112. Morgan DO. The dynamics of cyclin dependent kinase structure. *Curr Opin Cell Biol*. 1996;8:767-772.
113. Petri ET, Errico A, Escobedo L, Hunt T, Basavappa R. The crystal structure of human cyclin B. *Cell Cycle*. 2007;6(11):1342-1349. doi:10.4161/cc.6.11.4297
114. Hao B, Oehlmann S, Sowa ME, Harper JW, Pavletich NP. Structure of a Fbw7-Skp1-Cyclin E Complex: Multisite-Phosphorylated Substrate Recognition by SCF Ubiquitin Ligases. *Mol Cell*. 2007;26(1):131-143.
http://www.ncbi.nlm.nih.gov/entrez/query.fcgi?cmd=Retrieve&db=PubMed&dopt=Citation&list_uids=17434132
115. Valk E, Venta R, Ord M, Faustova I, Koivomagi M, Loog M. Multistep phosphorylation systems: tunable components of biological signaling circuits. *Mol Biol Cell*. 2014;25(22):3456-3460. doi:10.1091/mbc.E14-02-0774
116. Kõivomagi M, Örd M, Iofik A, et al. Multisite phosphorylation networks as signal processors for Cdk1. *Nat Struct Mol Biol*. 2013;20(12):1415-1424.
117. Deshaies RJ, Ferrell Jr. JE. Multisite phosphorylation and the countdown to S phase. *Cell*. 2001;107(7):819-822.
http://www.ncbi.nlm.nih.gov/entrez/query.fcgi?cmd=Retrieve&db=PubMed&dopt=Citation&list_uids=11779457
118. Trautmann S, McCollum D. Cell cycle: new functions for Cdc14 family phosphatases. *Curr Biol*. 2002;12(21):R733-5.

- http://www.ncbi.nlm.nih.gov/entrez/query.fcgi?cmd=Retrieve&db=PubMed&dopt=Citation&list_uids=12419203
119. Mochida S, Hunt T. Protein phosphatases and their regulation in the control of mitosis. *EMBO Rep.* 2012;13(3):197-203. doi:10.1038/embor.2011.263
 120. Galaktionov K, Beach D. Specific activation of cdc25 tyrosine phosphatases by B-type cyclins: evidence for multiple roles of mitotic cyclins. *Cell.* 1991;67:1181-1194.
 121. Millar JBA, Russell P. The cdc25 M-phase inducer: an unconventional protein phosphatase. *Cell.* 1992;68:407-410.
 122. Riedel CG, Katis VL, Katou Y, et al. Protein phosphatase 2A protects centromeric sister chromatid cohesion during meiosis I. *Nature.* 2006;441(7089):53-61.
http://www.ncbi.nlm.nih.gov/entrez/query.fcgi?cmd=Retrieve&db=PubMed&dopt=Citation&list_uids=16541024
 123. Jinno S, Suto K, Nagata A, et al. Cdc25A is a novel phosphatase functioning early in the cell cycle. *EMBO J.* 1994;13:1549-1556.
 124. Godfrey M, Touati SA, Kataria M, Jones A, Snijders AP, Uhlmann F. PP2ACdc55 Phosphatase Imposes Ordered Cell-Cycle Phosphorylation by Opposing Threonine Phosphorylation. *Mol Cell.* 2017;65(3):393-402 e3. doi:10.1016/j.molcel.2016.12.018
 125. Minshull J, Straight A, Rudner AD, Dernburg AF, Belmont A, Murray AW. Protein phosphatase 2A regulates MPF activity and sister chromatid cohesion in budding yeast. *Curr Biol.* 1996;6:1609-1620.
 126. Marston AL, Lee BH, Amon A. The Cdc14 phosphatase and the FEAR network control meiotic spindle disassembly and chromosome segregation. *Dev Cell.* 2003;4(5):711-726.
http://www.ncbi.nlm.nih.gov/entrez/query.fcgi?cmd=Retrieve&db=PubMed&dopt=Citation&list_uids=12737806
 127. Kamenz J, Ferrell Jr. JE. The Temporal Ordering of Cell-Cycle Phosphorylation. *Mol Cell.* 2017;65(3):371-373. doi:10.1016/j.molcel.2017.01.025

128. Reynard GJ, Reynolds W, Verma R, Deshaies RJ. Cks1 is required for G(1) cyclin-cyclin-dependent kinase activity in budding yeast. *Mol Cell Biol.* 2000;20(16):5858-5864.
129. Hadwiger JA, Wittenberg C, Mendenhall MD, Reed SI. The *Saccharomyces cerevisiae* CKS1 gene, a homolog of the *Schizosaccharomyces pombe* *suc1+* gene, encodes a subunit of the Cdc28 protein kinase complex. *Mol Cell Biol.* 1989;9(5):2034-2041.
http://www.ncbi.nlm.nih.gov/entrez/query.fcgi?cmd=Retrieve&db=PubMed&dopt=Citation&list_uids=2664468
130. Tang Y, Reed SI. The Cdk-associated protein Cks1 functions both in G1 and G2 in *Saccharomyces cerevisiae*. *Genes Dev.* 1993;7:822-832.
131. Yu J, Raia P, Ghent CM, et al. Structural basis of human separase regulation by securin and CDK1-cyclin B1. *Nature.* 2021;596:138-142.
132. Reynolds D, Shi BJ, McLean C, Katsis F, Kemp B, Dalton S. Recruitment of Thr 319-phosphorylated Ndd1p to the FHA domain of Fkh2p requires Clb kinase activity: a mechanism for CLB cluster gene activation. *Genes Dev.* 2003;17(14):1789-1802.
133. Eluere R, Offner N, Varlet I, et al. Compartmentalization of the functions and regulation of the mitotic cyclin Clb2 in *S. cerevisiae*. *J Cell Sci.* 2007;120(Pt 4):702-711.
http://www.ncbi.nlm.nih.gov/entrez/query.fcgi?cmd=Retrieve&db=PubMed&dopt=Citation&list_uids=17264146
134. Wäsch R, Cross F. APC-dependent proteolysis of the mitotic cyclin Clb2 is essential for mitotic exit. *Nature.* 2002;418:556-62.
135. Richardson H, Lew DJ, Henze M, Sugimoto K, Reed SI. Cyclin-B homologs in *Saccharomyces cerevisiae* function in S phase and in G2. *Genes Dev.* 1992;6(11):2021-2034.
136. Rudner AD, Murray AW. Phosphorylation by Cdc28 activates the Cdc20-dependent activity of the anaphase-promoting complex. *J Cell Biol.* 2000;149(7):1377-1390.

- <http://www.ncbi.nlm.nih.gov/cgi-bin/Entrez/referer?http://www.jcb.org/cgi/content/abstract/149/7/1377>
137. Rudner AD, Hardwick KG, Murray AW. Cdc28 activates exit from mitosis in budding yeast. *J Cell Biol.* 2000;149(7):1361-1376. doi:10.1083/jcb.149.7.1361
 138. Lew DJ, Reed SI. Morphogenesis in the yeast cell cycle: regulation by Cdc28 and cyclins. *J Cell Biol.* 1993;120(6):1305-1320.
 139. Lu D, Hsiao JY, Davey NE, et al. Multiple mechanisms determine the order of APC/C substrate degradation in mitosis. *J Cell Biol.* 2014;207(1):23-39. doi:10.1083/jcb.201402041
 140. Jaspersen SL, Huneycutt BJ, Giddings Jr. TH, Resing KA, Ahn NG, Winey M. Cdc28/Cdk1 regulates spindle pole body duplication through phosphorylation of Spc42 and Mps1. *Dev Cell.* 2004;7(2):263-274. http://www.ncbi.nlm.nih.gov/entrez/query.fcgi?cmd=Retrieve&db=PubMed&dopt=Citation&list_uids=15296722
 141. Castillo AR, Meehl JB, Morgan G, Schutz-Geschwender A, Winey M. The yeast protein kinase Mps1p is required for assembly of the integral spindle pole body component Spc42p. *J Cell Biol.* 2002;156(3):453-65. <http://www.ncbi.nlm.nih.gov/cgi-bin/Entrez/referer?http://www.jcb.org/cgi/content/full/156/3/453>
 142. Sajman J, Zenvirth D, Nitzan M, et al. Degradation of Ndd1 by APC/C(Cdh1) generates a feed forward loop that times mitotic protein accumulation. *Nat Commun.* 2015;6:7075. doi:10.1038/ncomms8075
 143. Shonn MA, Murray AL, Murray AW. Spindle checkpoint component Mad2 contributes to biorientation of homologous chromosomes. *Curr Biol.* 2003;13(22):1979-1984. http://www.ncbi.nlm.nih.gov/entrez/query.fcgi?cmd=Retrieve&db=PubMed&dopt=Citation&list_uids=14614824

144. Rudner AD, Murray AW. The spindle assembly checkpoint. *Curr Opin Cell Biol.* 1996;8:773-780.
145. Palframan WJ, Meehl JB, Jaspersen SL, Winey M, Murray AW. Anaphase inactivation of the spindle checkpoint. *Science (1979).* 2006;313(5789):680-684.
146. Ong SE, Blagoev B, Kratchmarova I, et al. Stable isotope labeling by amino acids in cell culture, SILAC, as a simple and accurate approach to expression proteomics. *Mol Cell Proteomics.* 2002;1(5):376-386. doi:10.1074/mcp.m200025-mcp200
147. Villen J, Gygi SP. The SCX/IMAC enrichment approach for global phosphorylation analysis by mass spectrometry. *Nat Protoc.* 2008;3(10):1630-1638. doi:nprot.2008.150 [pii] 10.1038/nprot.2008.150
148. Wang H, Huang ZX, Au Yong JY, et al. CDK phosphorylates the polarisome scaffold Spa2 to maintain its localization at the site of cell growth. *Mol Microbiol.* 2016;101(2):250-264. doi:10.1111/mmi.13386
149. Lianga N, Williams EC, Kennedy EK, et al. A Wee1 checkpoint inhibits anaphase onset. *J Cell Biol.* 2013;201(6):843-862. doi:10.1083/jcb.201212038
150. Rahal R, Amon A. Mitotic CDKs control the metaphase-anaphase transition and trigger spindle elongation. *Genes Dev.* 2008;22(11):1534-1548. doi:10.1101/gad.1638308
151. Lianga N, Doré C, Kennedy EK, et al. Cdk1 phosphorylation of Esp1/Separase functions with PP2A and Slk19 to regulate pericentric Cohesin and anaphase onset. *PLoS Genet.* 2018;14(3):e1007029. doi:10.1371/journal.pgen.1007029
152. Barford D. Structure, function and mechanism of the anaphase promoting complex (APC/C). *Q Rev Biophys.* 2011;44(2):153-190. doi:10.1017/S0033583510000259
153. Zhang S, Chang L, Alfieri C, et al. Molecular mechanism of APC/C activation by mitotic phosphorylation. *Nature.* 2016;533(7602):260-264. doi:10.1038/nature17973

154. Fujimitsu K, Grimaldi M, Yamano H. Cyclin-dependent kinase 1-dependent activation of APC/C ubiquitin ligase. *Science* (1979). 2016;352(6289):1121-1124.
doi:10.1126/science.aad3925
155. Qiao R, Weissmann F, Yamaguchi M, et al. Mechanism of APC/CCDC20 activation by mitotic phosphorylation. *Proc Natl Acad Sci U S A*. 2016;113(19):E2570-8.
doi:10.1073/pnas.1604929113
156. Kõivomägi M, Valk E, Venta R, et al. Cascades of multisite phosphorylation control Sic1 destruction at the onset of S phase. *Nature*. 2011;480:128-131. doi:nature10560 [pii] 10.1038/nature10560
157. Edelstein A, Amodaj N, Hoover K, Vale R, Stuurman N. Computer control of microscopes using μ Manager. *Curr Protoc Mol Biol*. 2010;Chapter 14:Unit14.20.
doi:10.1002/0471142727.mb1420s92
158. Ge SX, Jung D, Yao R. ShinyGO: a graphical gene-set enrichment tool for animals and plants. *Bioinformatics*. 2020;36(8):2628-2629. doi:10.1093/bioinformatics/btz931
159. Puig O, Caspary F, Rigaut G, et al. The tandem affinity purification (TAP) method: a general procedure of protein complex purification. *Methods*. 2001;24(3):218-229.
160. Lu D, Hsiao JY, Davey NE, et al. Multiple mechanisms determine the order of APC/C substrate degradation in mitosis. *J Cell Biol*. 2014;207(1):23-39.
doi:10.1083/jcb.201402041
161. Foster SA, Morgan DO. The APC/C subunit Mnd2/Apc15 promotes Cdc20 autoubiquitination and spindle assembly checkpoint inactivation. *Mol Cell*. 2012;47(6):921-932. doi:10.1016/j.molcel.2012.07.031
162. Chen S hong, Albuquerque CP, Liang J, Suhandynata RT, Zhou H. A proteome-wide analysis of kinase-substrate network in the DNA damage response. *J Biol Chem*. 2010;285(17):12803-12812. doi:10.1074/jbc.M110.106989

Publishing Agreement

It is the policy of the University to encourage open access and broad distribution of all theses, dissertations, and manuscripts. The Graduate Division will facilitate the distribution of UCSF theses, dissertations, and manuscripts to the UCSF Library for open access and distribution. UCSF will make such theses, dissertations, and manuscripts accessible to the public and will take reasonable steps to preserve these works in perpetuity.

I hereby grant the non-exclusive, perpetual right to The Regents of the University of California to reproduce, publicly display, distribute, preserve, and publish copies of my thesis, dissertation, or manuscript in any form or media, now existing or later derived, including access online for teaching, research, and public service purposes.

DocuSigned by:

Henry Ng

662605BAEFFB466...

Author Signature

8/21/2023

Date